Realization of a multistage OPCPA system in the mid infrared and its application in electron transfer studies at interfaces

Der Fakultät für Physik
der Universität Duisburg-Essen vorgelegte

Dissertation

zur Erlangung des akademischen Grades eines
Doktors der Naturwissenschaft
(Dr. rer. nat.)

von
Manuel Bridger
aus Regensburg, DE

1. Gutachter: Prof. Dr. Uwe Bovensiepen
2. Gutachterin: Prof. Dr. Clara Saraceno
Tag der mündlichen Prüfung: 26.09.2022

Hiermit erkläre ich,

- dass ich die eingereichte Dissertation selbstständig verfasst habe.
- dass ich die Erlangung des akademischen Grads eines Doktors der Naturwissenschaften (Dr. rer. nat.) anstrebe.
- dass ich nur die angegebenen Hilfsmittel verwendet habe und alle wörtlich oder inhaltlich überernommenen Stellen als solche kenntlich gemacht habe.
- dass die vorliegende Arbeit weder im Aus- noch im Inland in gleicher oder ähnlicher Form einer anderen Prüfungsbehörde vorgelegt wurde.

Duisburg, 05.12.2022

Abstract

The investigation of microscopic processes, like for example electron transfer and electron-phonon coupling, is crucial for improving our fundamental understanding of interaction principles in condensed matter and at interfaces. Complementary to experiments in thermal equilibrium, analysis in this domain has provided new opportunities for experimental analysis. Essential is in this case that the time resolution matches the time scale of the microscopic process of interest. Such are typical in the pico- and femtosecond regime, which requires the use of ultrashort pulses in the experiments.
In this thesis I present our self built optical parametric chirped pulse amplification (OPCPA) laser system, which generates mid infrared, ultrashort-laser pulses. They were employed in an investigation of the influence of vibrational modes to electron transfer dynamics at interfaces. The OPCPA generates three usable output laser pulses at different wavelengths, centered at 0.8 µm, 1.5 µm and 3.0 µm with pulse energies of 40 µJ, 1800 µJ and 800 µJ, respectively and pulse durations of 49 fs, 700 fs (uncompressed) and 63 fs, respectively.
In this work, we were particularly interested in understanding the electron transfer across solid/liquid (electrolyte) interfaces, which underlies much of the technology necessary for a sustainable global energy economy. We investigated Ferrocene undecanethiol[1] self assembled monolayers attached to a gold substrate in an acidic solution. We used a novel double-pump-probe measurement technique, in which the aromatic CH stretch of the Ferrocene head group is driven resonantly at 3.0 µm, an electron transfer is induced with the 0.8 µm pulses and the corresponding voltage drop across the interface is analyzed quantitatively.
We found that a vibrational preexcitation has a substantial effect on electron transfer as it induces two processes with the life times of 120 ± 30 fs and 4.0 ± 1.5 ps. Our interpretation is as follows: The mid infrared excitation of Ferrocene induces a short lived (120 ± 30 fs) reorientation of the dipoles of surrounding water molecules which supports the electron transfer from gold to Ferrocene. Before full thermalization of this condition, the energy distribution of Ferrocene is still spread for another 4.0 ± 1.5 ps, slightly enhancing the electron transfer. This means, that vibrational excitations of molecules at solid/liquid interfaces improve the electron transfer for up to 4.0 ps until the excited vibrational mode fully thermalizes.
This measurement procedure can also be used to investigate other vibrational excitation of molecules at solid/liquid interfaces and determine their influence on the electron transfer dynamics.

[1] Ferrocene head group with 11 piece CH chain

Zusammenfassung

Die Studie mikroskopischer Prozesse, wie z. B. Elektronentransfer und Elektron-Phonon-Kopplung, ist entscheidend für die Verbesserung unseres grundlegenden Verständnisses der Wechselwirkungsprinzipien in kondensierter Materie und an Grenzflächen. Diese Untersuchungen eröffnen ein weites Feld an Möglichkeiten der experimentellen Analyse. Entscheidend ist in diesem Fall, dass die Zeitauflösung mit der Zeitskala des interessierenden mikroskopischen Prozesses übereinstimmt. Solche sind im Pico- und Femtosekundenbereich typisch, was die Verwendung ultrakurzer Pulse in den Experimenten erfordert.
In dieser Arbeit stelle ich unser selbst gebautes optisches parametrisches gechirptes Pulsverstärkungssystem (OPCPA) vor, das ultrakurze Laserpulse im mittleren Infrarotbereich erzeugt. Dieses wurde für eine Untersuchung des Einflusses von Schwingungsmoden auf die Elektronentransferdynamik an Grenzflächen eingesetzt. Der OPCPA erzeugt drei nutzbare Ausgangslaserpulse bei den Wellenlängen 0,8 µm (VIS), 1,5 µm (NIR) und 3,0 µm (MIR) mit Pulsenergien von 40 µJ, 1800 µJ bzw. 800 µJ und Pulsdauern von 49 fs, 700 fs (unkomprimiert) bzw. 63 fs.
Bei dieser Arbeit waren wir besonders daran interessiert, den Elektronentransfer an Fest-Flüssig-Grenzflächen (Elektrolyten) zu verstehen, der einem Großteil der für eine nachhaltige globale Energiewirtschaft erforderlichen Technologie zugrunde liegt. Wir untersuchten Ferrocen-Undekanthiol[2], das auf einem Goldsubstrat in einer sauren Lösung als selbstorganisierte Monoschicht (SAM) vorliegt. Wir haben eine neuartige Doppel-Pump-Probe-Messtechnik verwendet, bei der die aromatische CH-Streckung der Ferrocen-Kopfgruppe bei 3 µm resonant angetrieben wird, ein Elektronentransfer mit 0,8 µm-Pulsen induziert wird und der entsprechende Spannungsabfall an der Grenzfläche quantitativ analysiert wird.
Wir haben herausgefunden, dass eine Schwingungsvoranregung einen wesentlichen Einfluss auf den Elektronentransfer hat, da sie zwei Prozesse mit Lebensdauern von 120 ± 30 fs und 4,0 ± 1,5 ps induziert. Unsere Interpretation lautet wie folgt: Die Anregung von Ferrocen im mittleren Infrarotbereich induziert eine kurzlebige (120 ± 30 fs) Umorientierung der Dipole der umgebenden Wassermoleküle, die den Elektronentransfer von Gold auf Ferrocen unterstützt. Vor der vollständigen Thermalisierung dieser Bedingung ist die Energieverteilung von Ferrocen noch für weitere 4,0 ± 1,5 ps verbreitert, was den Elektronentransfer leicht verstärkt. Das bedeutet, dass Schwingungsanregungen von Molekülen an Fest-Flüssig-Grenzflächen den Elektronentransfer für bis zu 4 ps verbessern, bis die angeregte Schwingungsmode vollständig thermalisiert ist.
Mit diesem Messverfahren lassen sich auch andere Schwingungsanregungen von Molekülen an Fest-Flüssig-Grenzflächen untersuchen und deren Einfluss auf die Elektronentransferdynamik bestimmen.

[2]Ferrocen-Kopfgruppe mit 11-gliedriger CH-Kette

Contents

Chapter 1

Introduction

Time scales of natural processes extend over various orders of magnitude, some take several hours (like the transition between the tides), years (the rusting of an old car) or even much longer (the evolution of a star to a super nova) to take effect. Towards shorter time scales, there are phenomena, which happen on timescales so short and on microscopical length scales, that people from 100 years ago could not even think about investigating them (like tracking the motion of a single molecule or the creation and destruction of excitons).
However, this changed dramatically, with the invention of lasers [1,2] and in particular ultrashort laser pulses. The first to reach a pulse duration below 100 femtoseconds with pulses as short as 27 femtoseconds were J. A. Valdmanis et al. in 1985 [3]. With these pulses, it was possible to investigate ultrashort processes, which were a hundred years ago believed to be instantaneous. And with that, a big step was made towards the shortest possible pulse durations. Only one year later, titanium doped sapphire (Ti-Sa) oscillators were introduced [4], which were quickly established as the workhorses for ultrashort laser measurements. Nowadays, commercially available systems can be purchased with pulse durations as short as 5 fs directly from the oscillator. With pulses that short, it is possible to do research on time scales completely new to science. Even with the fastest electronics, time resolutions lower than several picoseconds are out of reach.
However, Ti-Sa oscillators for themselves only yield comparably low pulse energies of a few nJ in the best case. To improve this, many scientists were looking how to amplify the Ti-Sa pulses the best for their individual application. The fundamental problem is that with stronger amplification of the laser pulses, the intensity of the beams increase so much that the nonlinear phase of the laser pulses deformed the pulses' temporal structure and made them therefore unusable for experiments. The novel idea of chirped pulse amplification (CPA) is to reduce the intensity by increasing the pulse duration prior to amplification. Subsequently, the elongated pulses can be

amplified by orders of magnitude efficiently. This is followed by a recompression of the pulse back to the optimal pulse duration. This approach significantly rose the peak power of the laser pulses. It was introduced in 1985 by Gérard Mourou and Donna Strickland [5] for which they were awarded the Nobel Prize in physics in 2018.
With high pulse energies and ultrashort pulse durations it was then possible to do experiments on a femtosecond timescale such as time-resolved spectroscopy (e.g. photoelectron spectroscopy [6], fluorescence spectroscopy [7] or transient absorption spectroscopy [8]), ultrafast material ablation [9] or high harmonic generation [10], just to name a few.
But there was still room for improvements. CPA is using a pumped laser medium to amplify the laser pulses, which has the following drawbacks: Amplifying in a laser medium reduces the spectral bandwidth due to gain narrowing and thereby the shortest possible pulse duration increases. Additionally, due to Stokes shift, a part of the pumping energy of the laser medium is dissipated into the laser medium. Therefore, when using CPA with high average powers, the laser medium needs to be cooled to dissipate this residual energy. Additionally, thermal lensing in the laser medium leads to temperature dependent aberrations of the beam, which need to be minimized.
The solution to avoid storage of energy in the medium is to use amplification by optical parametric amplification (OPA). Within this nonlinear process, the seed laser pulses are amplified with a second, more intense pump laser. Within this process, an so-called idler pulse is generated, which possesses the photon energy of the difference of the seed and pump photons. This has the advantage, that the energy difference between the pump and seed pulses is not stored in the medium and will therefore not heat the system. For OPA , there can also be found nonlinear crystals which support broader bandwidths compared to amplification in a laser media.
OPA is often pumped by pulses amplified by CPA . Many well established sources work on the basis of YAG doped with rare earth ions and yield high power pulses centered at around 1 µm and pulse durations in the picosecond regime. To match the pulse duration of the seed pulses with those of the pump, the seed pulses need to be stretched. The amplification of stretched pulses is commonly referred to optical parametric chirped pulse amplification (OPCPA).
The newly generated idler beam from this approach is generated with a photon energy being the difference between the pump and signal energies. Therefore, the idler wavelength is typically longer than the wavelengths from the pump or seed. This makes OPA a good tool to access the near and mid infrared range by utilizing the idler pulses. Depending on the energy difference between signal and pump photon energy, this newly generated idler light can end up even in the THz region [11]. For a long time, there were no lasers with a high quality beam shape, energy and pulse duration in this region, for which it was then called the "THz gap". Measurement techniques

which have high requirements to the beam quality, pulse duration, energy and coherence could then be taken on with OPCPA sources. Some of these applications are: Sensing of trace elements, hyperspectral imaging or microspectroscopy [12–16].
The demand for MIR laser sources with high peak powers spiked even more in 2012 after Popmintchev et al. showed experimentally [17], that the cut-off frequency of high harmonic generation could be extended into the keV regime if a driver laser in the MIR range was used. This allows for the production of high brilliance X-ray radiation on a lab scale which is comparable to the ultrashort pulse outputs of synchrotrons.
This kicked off several approaches [18–23] to design a suitable system to drive this extreme process. The light pulses generated by high harmonic generation also exhibit excellent properties: Ultrashort, coherent and broadband pulses, with a reasonable photon yield to be a source for X-ray absorption spectroscopy (XAS) [24, 25]. Due to the broad bandwidth of several hundred eV it can even be used for single shot pump probe near edge X-ray absorption fine structure (NEXAFS) measurements [26, 27].
By utilizing the ultrashort, Gaussian beam shaped and highly energetic mid-IR pulses, it is also possible to conduct time resolved ultrafast vibrational spectroscopy [28] to examine the dynamics of interfacial electron transfer, free-carrier formation, and bimolecular charge recombination and trapping in an organic photovoltaic material [29]. Using this method and in collaboration with chemists, it was possible to visualize the motion of molecules [30], temporally resolve interface dynamics and to investigate inter- [31] and intramolecular processes like bond breaking.
For all these measurements, sophisticated and specialized OPCPA systems had to be developed. There are various approaches with the goal of reaching high repetition rate and pulse energy in the near IR [32–34], and mid IR [18, 20, 35–42] or shortest possible pulse durations in the infrared region [19].
To reach high pulse energies and short pulses at a high repetition rate, most successful current laser systems use OPCPA to convert laser light from either a visible or near infrared laser source like a Ti-Sa-oscillator down to the mid infrared range.
The biggest differences are the used nonlinear crystals. For this purpose, there is a number of nonlinear crystals which are transparent for these wavelengths, can have phase matching for the down conversion process and yield a good conversion efficiency. The crystals which show excellent specifications for mid infrared generation are KTA (Potassium Titanyl Arsenate), LNB (Lithium Niobate), $LiIO_3$ (Lithium Iodate) and PPLN (Periodically-Poled Lithium Niobate).
In this thesis, I will present our realization of a four stage OPCPA system, producing pulse in the mid- and near-infrared with high pulse energy. Also, we maintained a broad spectral bandwidth of the laser pulses allowing for

final pulse durations of less than 70 fs for the amplified pulses.
This system was successfully used for two experiments: One is carrying out double pump measurements of electron dynamics at solid/liquid interfaces in operating conditions using a novel measurement technique in a chemical cell. These results were achieved in collaboration with our colleagues from professor Kramer Campen from university Duisburg/Essen.
The other is involved with the generation of high harmonics to perform XAS and NEXAFS experiments. This part of the system was mainly executed by my lab mate Oscar Naranjo and will therefore be discussed in his thesis.

Outline

The thesis is structured in the following way: In the next chapter, I will discuss the theoretical background, necessary to understand the OPCPA setup. In particular, I will introduce the nonlinear processes at work and their criteria to be efficient, the principle of chirped pulse amplification and important aspects of optical parametric chirped pulse amplification.
Chapter 3 explains the newly developed OPCPA setup at the University of Duisburg-Essen. Firstly, the pump channel is explained, which yields intense pump pulses from which the energy is drawn for the amplification channel. Secondly, the amplification channel, which consists of four individual amplification stages. Within the amplification stages, we generate laser pulses in the near and mid-IR , which are then compressed in individual compressors. The results of the compressions are analyzed with frequency resolved optical gating (FROG).
Chapter 4 is dedicated to the proof-of-principle experiments with self assembled monolayers of Ferrocene on top of a gold substrate in liquid solution. In these measurements, we used the generated laser pulses in the mid-IR and near-IR from the OPCPA to execute time dependent measurements and thereby investigate whether electron transfer between a metal and liquid is mode specific. In this effort, we find two processes with life times of 120 ± 30 fs and 4.0 ± 1.5 ps, which show a vibrational enhanced electronic transfer between Ferrocene and gold. In chapter 5, I will summarize my efforts and point out possible future applications.

Chapter 2

Concepts for nonlinear optics

This work includes various applications of nonlinear optical effects of mostly second and third order. To gain a better understanding why the setup was built in the way described in the later chapters of this work, I will give a short view into principles of three wave mixing processes, phase relations in nonlinear processes, handling the chirp of a pulse and obstructing effects of high intensity laser pulses. In this chapter, I will follow closely the work of [43–46].

2.1 The nonlinear polarization

Whenever a light wave travels through a material, its electric field $\vec{E}$ instantaneously rearranges the charge distribution in the material. This can be described by the electric polarization $\vec{P}$, which is the induced electric dipole moment per unit volume. For weak fields, the charge distribution around the atom will follow the applied electric field such that a linear dependency is established between the induced dipole moment and the applied field, meaning that the electrons will oscillate and radiate at the same frequency as the applied field. For stronger fields however, the response of the system can be more complex and the effects of a nonlinear dependency need to be accounted for. We can express the polarization by a series expansion:

$$\vec{P}(\omega) = \epsilon_0 \cdot \{\chi^{(1)}\vec{E}(\omega) + \chi^{(2)}\vec{E}^2(\omega) + \chi^{(3)}\vec{E}^3(\omega) + ...\} \tag{2.1}$$

$$= \vec{P}^{(1)}(\omega) + \vec{P}^{(2)}(\omega) + \vec{P}^{(3)}(\omega) + ... \tag{2.2}$$

$$= \vec{P}_L(\omega) + \vec{P}_{NL}(\omega) \tag{2.3}$$

where the proportionality between the electric field and the polarisation is the scalar susceptibility $\chi^{(n)}$ times the vacuum permittivity ϵ_0. The term with $\chi^{(1)}$ represents the linear response of the medium ($\vec{P}_L(\omega)$), while the higher terms correspond to the non linear response ($\vec{P}_{NL}(\omega)$). $\chi^{(n)}$ is a square tensor of n+1-th order representing all possible interactions. But

since several components of $\chi^{(n)}$ cancel out or are identical due to symmetry [43], a contracted notation was made. For three wave mixing processes, this notation takes the symmetry of the tensor into account:

$$d_{il} = \frac{1}{2}\chi^{(2)}_{ijk} \tag{2.4}$$

Due to symmetry, the last two indices are replaced by l which correlates to jk in the following fashion:

jk	11	22	33	23,32	13,31	12,21
l	1	2	3	4	5	6

In the case of the electric field $E(\omega)$ being much lower than the atomic field E_{atom}:

$$\frac{E(\omega)}{E_{atom}} \propto \left|\frac{\chi^{(n+1)}}{\chi^{(n)}}\right| << 1 \tag{2.5}$$

Meaning, that the higher the order of $\chi^{(n)}$, the lower the magnitude of it. Second order effects are described with the term $\vec{P}^{(2)}(\omega)$ and are used in many laser systems. It is important to notice, all second order effects can only occur in non-centrosymmetric materials - that is, in crystals which do not exhibit inversion symmetry or on interfaces. Since this is not given in liquids, gases, amorphous solids (such as glasses) and even many crystals, $\chi^{(2)}$ vanishes identically and consequently these materials cannot generate second-order nonlinear optical interactions. Birefringent crystals exhibit broken centrosymmetry. Some examples are beta barium borate (BBO), lithium triborate (LBO) and potassium titanyle arsenate (KTA).
One can evaluate the polarization by using the plane wave approach. For second order effects, this consists of two electric field components with the frequencies ω_1 and ω_2:

$$\vec{E}(\omega) = E_1 e^{-i\omega_1 t} + E_2 e^{-i\omega_2 t} + c.c. \tag{2.6}$$

where c.c. is the complex conjugate. The second-order polarization induced by the two optical fields through a noncentrosymmetric medium ($\chi^{(2)} \neq 0$) can be written as:

$$\vec{P}^{(2)}(\omega) = \epsilon_0 \chi^{(2)} \vec{E}^2(\omega) \tag{2.7}$$

$$= \epsilon_0 \chi^{(2)} \{\underbrace{E_1^2 e^{-2i\omega_1 t}}_{SHG_{\omega_1}} + \underbrace{E_2^2 e^{-2i\omega_2 t}}_{SHG_{\omega_2}} + \underbrace{2E_1 E_2 e^{-it*(\omega_1+\omega_2)}}_{SFG} + \underbrace{2E_1 E_2 * e^{-it*(\omega_1-\omega_2)}}_{DFG/OPA} + c.c.\} \tag{2.8}$$

This shows that new frequencies are generated, when going through such a medium:

- Second harmonic generation (SHG) of E_1 and E_1: $2\omega_1$ and $2\omega_2$
- Sum frequency generation (SFG): $\omega_1 + \omega_2$ and
- Difference frequency generation (DFG) or optical parametric amplification (OPA): $\omega_1 - \omega_2$

For DFG and OPA processes, usually these notations are used: $\omega_1 = \omega_p$ (for pump), $\omega_2 = \omega_s$ (for signal) and $\omega_2 - \omega_1 = \omega_i$ (for idler). For these three-wave-mixing processes, the energy conservation is automatically satisfied: $\hbar\omega_1 = \hbar\omega_2 + \hbar\omega_3$ (assuming $\omega_1 > \omega_2 > \omega_3$), however momentum conservation is not always fulfilled, as $\hbar\vec{k_1} = \hbar\vec{k_2} + \hbar\vec{k_3}$ is not generally satisfied.

2.1.1 Coupled wave equations for OPA

As discussed, OPA is a second-order $\chi^{(2)}$ process in which two incoming waves (ω_p and ω_s with $\omega_p > \omega_s$) interact in a non-centrosymmetric media ($\chi^{(2)} \neq 0$) and generate a new field with lower frequency ($\omega_i = \omega_p - \omega_s$, see figure 2.1). To understand the interaction of these light fields better, one can derive the wave equation from Maxwell's equations under consideration of no free charges ($\rho = 0$), no free currents ($\vec{J} = 0$) and non-magnetic material ($\mu_r = 1$) [43]:

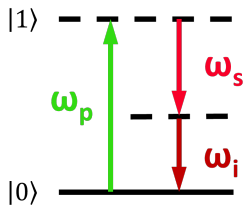

Figure 2.1: Energy schematic of a OPA process

$$\nabla^2\vec{E} - \frac{1}{c^2}\partial_t^2\epsilon_r\vec{E} = \frac{1}{\epsilon_0 c^2}\partial_t^2\vec{P}^{NL} \tag{2.9}$$

where ϵ_r is the relative permittivity of the nonlinear medium, defined as $\epsilon_r = \chi^{(1)} + 1$, c is the vacuum velocity of light, $\vec{P}^{NL}$ is the nonlinear part of the polarization as discussed in eq. 2.3. In case of negligible nonlinear polarization, the wave equation can be fulfilled with a plane wave approach with constant amplitude as the light travels through the medium. If we assume the wave to be linearly polarized and propagates in z direction, the electric field can be written in the following form:

$$\vec{E}(z,t) = Ae^{i(kz-\omega_1 t)} + c.c. \tag{2.10}$$

$k = n\omega/c$ is the wavevector, with $n = \sqrt{1+\chi^{(1)}}$ being the linear refractive index. To include now the nonlinear polarization, the amplitude will be considered to be slowly varying throughout the material, making it dependent on z, $A(z)$. For simplicity, we only consider the polarization term contributing to OPA . The nonlinear source term from eq. 2.9 oscillates at the idler frequency and can be written as

$$P_i(z,t) = B_i e^{-i(\omega_i t)} + c.c. \tag{2.11}$$

From eq. 2.8 we know, that the amplitude of the polarization is dependent of the ones from the pump and signal fields, A_p and A_s:

$$B_i = 4\epsilon_0 d_{\text{eff}} A_p A_s^* e^{i(k_p - k_s)z} \tag{2.12}$$

in this equation we use d_{eff} which is a combination of one or more d_{ijk} from eq. 2.4 corresponding to the polarization of the participating light fields. Now we can substitute equations 2.10, 2.11 and 2.12 into eq. 2.9. And since we have plane waves propagating in z direction, we can also replace ∇^2 by $\dfrac{d^2}{dz^2}$ and get:

$$\left[\frac{d^2A_i}{dz^2} + 2ik_i\frac{dA_i}{dz} - k_i^2 A_i + \frac{\epsilon_r\omega_i^2 A_i}{c^2}\right] e^{i(k_i z + \omega_i t)} + c.c. = \\ = -\frac{4\epsilon_0 d_{\text{eff}}\omega_i^2}{c^2} A_p A_s^* e^{i[(k_p - k_s)z - \omega_i t]} + c.c. \tag{2.13}$$

Now we can slim down the equation by canceling the third and fourth term on the left hand side, since $k_i^2 = \epsilon_r\omega_i^2/c^2$. Also the complex conjugated parts and the time depencence ($exp(-i\omega_i t)$) can be left out without disturbing the equality. We also use the slowly varying amplitude approximation, which assumes:

$$\left|\frac{d^2A_i}{dz^2}\right| \ll \left|k_i\frac{dA_i}{dz}\right| \tag{2.14}$$

This condition requires that the fractional change in A_i in a distance of the order of an optical wavelength must be much smaller than unity. If all the reductions are applied, we end up with the following equation from eq. 2.13:

$$\frac{dA_i}{dz} = \frac{2id_{\text{eff}}\omega_i^2}{k_i c^2} A_p A_s^* e^{i\Delta k z} \tag{2.15}$$

where we have introduced the so-called phase matching condition with the wave vector mismatch:

$$\Delta k = k_p - k_s - k_i \tag{2.16}$$

Perfect phase matching can be accomplished if $\Delta k = 0$, which means that the emitted electromagnetic wave and the nonlinear polarization keep a constant phase throughout the entire crystal thickness. This relation is very important for nonlinear processes and hence will be discussed in greater detail in section 2.3.
Analogously, we can derive similar equations for pump and signal fields:

$$\frac{dA_p}{dz} = \frac{2id_{\text{eff}}\omega_p^2}{k_p c^2} A_s A_i e^{-i\Delta k z} \tag{2.17}$$

$$\frac{dA_s}{dz} = \frac{2id_{\text{eff}}\omega_s^2}{k_s c^2} A_p A_i^* e^{-i\Delta kz} \tag{2.18}$$

Without further assumptions, the wave equations can only be solved numerically. This will yield a development of the individual field amplitudes throughout the material. To test different situations, one can use the program SNLO from AS-Photonics [47], which is a useful tool to gather experience for the quantities within the process. Note that eq. 2.15, 2.17 and 2.18 neglect to account for numerous effects that are crucial in an actual experimental setting, particularly for ultrashort pulses. These effects include the difference in group velocities between the interacting waves, pulse broadening due to dispersion and spatial walk-off due to birefringence in the nonlinear medium. But still, they give a good physical insight into the nonlinear processes that are central to this thesis: DFG and OPA . Since these processes are of special significance in this thesis, I will investigate them in more detail in the next section.

2.1.2 The Manley-Rowe relations

The Manley-Rowe relations were originally developed in the late 50s to predict energy transfer between waves in nonlinear electrical circuits [48]. The equations can be used in our case to describe the energy conservation in three-wave mixing processes. The relations can be derived directly from the coupled equations 2.15, 2.17 and 2.18. The Manley-Rowe relations for DFG are typically written as:

$$\frac{d}{dz}\left(\frac{I_i}{\omega_i}\right) = \frac{d}{dz}\left(\frac{I_s}{\omega_s}\right) = -\frac{d}{dz}\left(\frac{I_p}{\omega_p}\right) \tag{2.19}$$

Since the energy of a photon is $\hbar\omega$, the quantity I/ω is proportional to the photons per unit area per unit time. Therefore the Manley-Rowe relations can also be written as:

$$\frac{dN_i}{dz} = \frac{dN_s}{dz} = -\frac{dN_p}{dz} \tag{2.20}$$

These relations tell us that the rate at which photons at frequency ω_i are created is equal to the rate at which photons at frequency ω_s are created and is equal to the rate at which photons at frequency ω_p are destroyed. This result can be understood intuitively by means of the energy level description of a three-wave mixing process, which is shown in figure 2.1. This diagram shows that, for a lossless medium, the creation of an ω_i photon must be accompanied by the creation of an ω_s photon and the annihilation of an ω_p photon. This is an important result for OPCPA design, since it implies that the wavelength relation between the pump and seed impacts the efficiency of the amplification process.

2.1.3 A more detailed look into OPA and DFG

Without assumptions, the OPA and DFG processes behave the same way and follow the same equations. However, the idea or wanted outcome of the processes are different. Within an optical parametric amplifier, the goal is to amplify the so-called seed beam to become a more energetic signal beam (as depicted in fig. 2.2). The goal of using a DFG process is, to generate the idler beam. After the amplification process, the signal and pump beams are separated from the idler beam, such that it can be used for further applications.

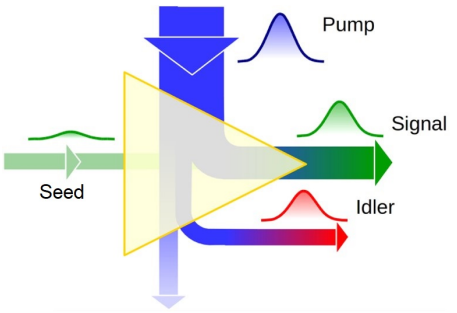

Figure 2.2: Schematic of an OPA process. (Graphic taken from [49])

In a common OPA scenario, the pump intensity is high and undepleted, the signal intensity is low in comparison and there is no idler in the beginning. These assumptions are useful for describing the initial state of the amplification, where the pump is several orders of magnitude higher than the seed. Using these assumptions for now, we set $A_p = const$ and $A_i = 0$. Then we can solve the equations 2.15, 2.17 and 2.18 analytically to be [50]:

$$I_s = I_s(0)\cosh^2(gz) = I_s(0) + I_s(0)\sinh^2(gz) \tag{2.21}$$

$$I_i = I_s(0)\frac{\omega_i}{\omega_s}\sinh^2(gz) \tag{2.22}$$

where $g = \sqrt{\Gamma^2 - (\Delta k/2)^2}$ is the so-called gain parameter and Γ_0:

$$\Gamma = d_{\text{eff}}^2 I_p \frac{2\omega_s\omega_i}{\epsilon_0 c^3 n_p n_s n_i} \tag{2.23}$$

n_p, n_s, and n_i refer to the refractive index at the pump, signal and idler wavelengths.

Looking at the gain parameter more in detail, one can see, that it only depends on the intensity of the pump and not on the other two frequencies, meaning the relative gain of the signal and idler only depend on the pump intensity, respectively. However, since the gain parameter is a multiplier to the initial intensity of the seed beam, the final intensity is very well dependent of the incoming intensity of the seed beam as well.

2.1.4 Phase evolution

The phase of the three interacting waves plays an important role in OPA . The evolution of the phases, for the case of zero initial idler, can be derived from the coupled wave equations [51]:

$$\phi_s(z) = \phi_s(0) - \frac{\Delta k z}{2} + \frac{\Delta k \gamma_s^2}{2} \int \frac{dz}{f + \gamma_s^2} \tag{2.24}$$

$$\phi_i(z) = \phi_p(0) - \phi_s(0) - \frac{\Delta k z}{2} - \frac{\pi}{2} \tag{2.25}$$

$$\phi_p(z) = \phi_p(0) - \frac{\Delta k}{2} \int \frac{f dz}{1 - f} \tag{2.26}$$

where $f = 1 - I_p(z)/I_p(0)$ is the fractional depletion of the pump and $\gamma_s^2 = \dfrac{\omega_p I_s(0)}{\omega_s I_p(0)}$ is the input photon intensity ratio of the signal and pump. These equations have many significant implications for laser design:
First, it is worth mentioning that the direction of energy flow in the OPA is governed by the OPA phase $\phi_{OPA} = \phi_p - \phi_s - \phi_i$. The idler initially automatically takes a phase of $\phi_i(z) = \phi_p(0) - \phi_s(0) - \frac{\pi}{2}$ which maximizes the parametric gain such that $\phi_{OPA} = -\frac{\pi}{2}$. For increasing values of ϕ_{OPA} the efficiency of the process is reduced until reaching $\phi_{OPA} = 0$ when back conversion occurs and energy is transferred from the idler and signal back to the pump. Second, the phase of the amplified field does not depend on the phase of the pump field, and therefore optical aberrations and chirp in the pump are not transferred to the seed during amplification. However, the phase does depend on the pump intensity, implying that fluctuations in the pump can affect the amplified phase. This deleterious effect is particularly problematic close to pump depletion. Finally, phase changes resulting from parametric amplification, are linearly dependent on the phase mismatch. Meaning as well, that in case of perfect phase matching ($\Delta k = 0$), there is no temporal evolution of the phase.

2.1.5 Pump depletion and saturated OPA

In the setup discussed in chapter 3, the amplification processes are meant to convert as much energy as possible from the pump into the signal and idler beams. Hence, we chose the crystal length and the intensities of the beams such, that at the end of the crystal, the pump energy is transferred as good as possible to the signal and newly generated idler.
Therefore we must consider pump depletion as well now. The equations 2.15, 2.17 and 2.18 can then be solved by the Jacobi elliptic functions [52]. Alternatively, the solutions are found by solving the coupled wave equations numerically by standard approaches such as the Runge-Kutta method [53]. This solving algorithm was also used in the Matlab program employed to

calculate the amplification efficiency and bandwidth of our amplification stages.
A good example of the evolution of the individual intensities of the pump signal and idler were calculated by J. Rothhardt [46]. In figure 2.3 , the intensities and phase of the signal (gray), idler (red) and pump wave (blue) are displayed versus the propagation length z, which has been normalized to the characteristic nonlinear length $L_{NL} = 1/\Gamma$.

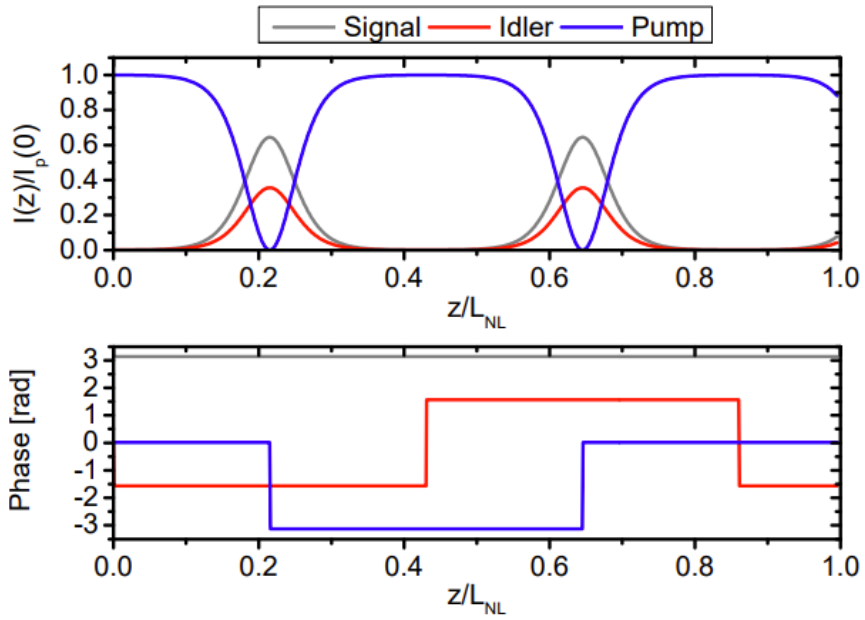

Figure 2.3: Calculated evolution of the intensities (top) and phases (bottom) of signal, idler and pump wave in an OPA with strong pump depletion and back-conversion (λ_p =515 nm, λ_s = 800 nm, $I_s(0)/I_p(0) = 10^{-3}$). (Graphic taken from [46])

For these calculations, perfect phase matching was assumed. They show, once the pump is depleted at $z = 0.215 \cdot L_{NL}$, the phase of the pump drops to $-\pi$ and back conversion starts due to the changed OPA phase $\phi_{OPA} = +\frac{\pi}{2}$. Therefore, for best results in conversion of the pump energy to the signal and idler, the process should end at this point, meaning the crystal length should be chosen to be close to $0.215 \cdot L_{NL}$. Since $L_{NL} = 1/\Gamma \propto 1/I_p$, the optimal crystal length is for one dependent on the pump Intensity used for the process and for the other on the phase matching within the medium, as we will see in the following sections.

2.2 Conversion efficiency

If we look again at equation 2.18 and consider the pump laser energy to be constant, the amplification of the signal from $z = 0$ to z is given by [52]:

$$\eta = \eta_{max} \cdot \frac{\sin^2\left(\frac{\Delta kz}{2}\right)}{\left(\frac{\Delta kz}{2}\right)^2} = \eta_{max} \cdot \mathrm{sinc}^2\left(\frac{\Delta kz}{2}\right) \tag{2.27}$$

with η_{max} being the maximum conversion efficiency with perfect phase matching. This relation of η with Δk describes the relation between the accumulated wave vector mismatch with the efficiency of the process and is plotted in figure 2.4. The full width at half maximum (FWHM) of this function is $\Delta kz/2 = 2.783$ and is an important quantity to determine the maximal crystal length for an optimal amplification process.
This function is 0 at $|\Delta k| = n\frac{\pi}{z}$ for $n \in \mathbb{Z} \setminus \{0\}$. This relation determines also the corresponding length, up to which energy transfer in the desired direction occurs. If we rearrange this relation to $z = \frac{\pi}{\Delta k} = l_c$, we find the so-called coherence length l_c.

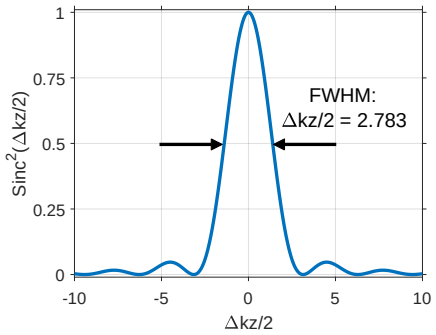

Figure 2.4: Process efficiency as a function of phase mismatch in the non depleted pump approximation.

2.3 Phase matching

In principle, all three-wave-mixing processes can always happen in non-centrosymmetric media. However, the efficiency and probability is determined by phase matching ($\Delta k = k_1 + k_2 - k_3 = 0$). Only if a particular phase relation between the participating fields is maintained, a desired nonlinear process is predominant. If we look closer at second harmonic generation,

the phase matching condition is given as:

$$\Delta k = 2k_1 - k_2 \tag{2.28}$$

$$= 2n(\omega_1)\frac{\omega_1}{c} - n(2\omega_1)\frac{2\omega_1}{c} \stackrel{!}{=} 0 \tag{2.29}$$

$$\Rightarrow n(\omega_1) \stackrel{!}{=} n(2\omega_1) \tag{2.30}$$

For homogeneous, isotropic media the refractive index decreases monotonically with the wavelength. Thus, phase matching is impossible. Representative for this sort of materials is Sapphire in figure 2.5.

2.3.1 Critical phase matching

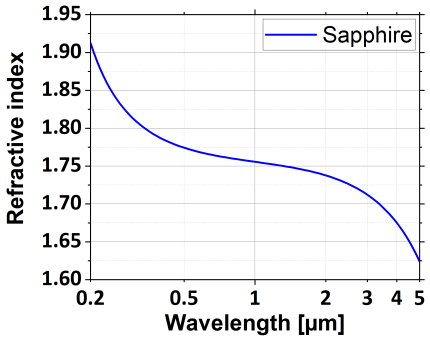

Figure 2.5: Refractive index of Sapphire representative for common glasses. [54]

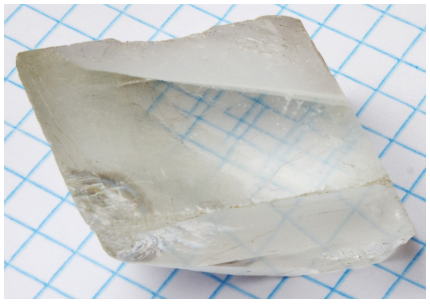

Figure 2.6: A calcite crystal displays the double refractive properties while sitting on a sheet of graph paper [55].

A common way to still achieve phase matching is by using birefringent crystals and hence is called birefringent or critical phase matching. This technique exploits the fact, that the refractive index of these crystals is not only depended on the wavelength, but also on the polarization and propagation direction of the electric field. The simplest type of birefringence is described as uniaxial, meaning that there is a single direction governing the optical anisotropy whereas all directions perpendicular to it are optically equivalent. Thus, rotating the material around this axis does not change its optical behavior. This special direction is known as the optical axis of the material. For uniaxial crystals, light polarized perpendicular to the plane containing the wave vector $\vec{k}$ and the optical axis is known as the ordinary ray, experiencing a refractive index n_0. While light with a polarization in the plane of the wave vector $\vec{k}$ and the optical axis experience the extraordinary refractive index n_e. Therefore, we can introduce the so-called index ellipsoid with the general formula:

$$\frac{x^2}{n_x^2} + \frac{y^2}{n_y^2} + \frac{z^2}{n_z^2} = 1 \tag{2.31}$$

which reads for the uniaxial case ($n_x = n_y \neq n_z$, see fig. 2.7) as:

$$\frac{x^2 + y^2}{n_0^2} + \frac{z^2}{n_e^2} = 1 \tag{2.32}$$

To fine tune the refractive index to match for example the second harmonic case from equation 2.30, one takes an angle in between the ordinary and the extraordinary axis. In that way, the effective refractive index reads as:

$$\frac{1}{n_e(\theta)^2} = \frac{\cos^2\theta}{[n_0]^2} + \frac{\sin^2\theta}{[n_e]^2} \tag{2.33}$$

with θ being the angle between the z direction and the ordinary plane. Due to the sensitivity to the angular alignment of the crystal, this method has its name "critical" phase matching.

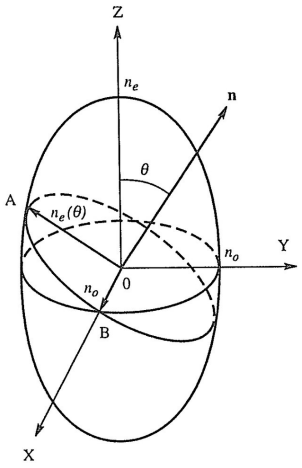

Figure 2.7: Depiction of the index ellipsoid of an uniaxial crystal with extraordinary axis in z direction. (Graphic taken from [56])

For the processes of SFG, OPA and DFG one also speaks of type I and type II interactions. Contrary to the second harmonic case, in the other mentioned cases, one has three instead of two different interacting wavelengths. In the so-called type I interaction, two of the three participating wavelengths follow the ordinary axis and one the extraordinary and vice versa in the type II interaction.
If such a crystal is purchased for the laser laboratory, usually one orders it such, that the transparent crystal surfaces enclose already the correct theta angle with the optical axis. Commonly used crystals in laser laboratories of that type are for example Beta Barium Borate (BBO), Lithium Niobate (LNB), Lithium iodate ($LiIO_3$).
Biaxial crystals ($n_x \neq n_y \neq n_z$, i.e. Potassium Titanyl Arsenate (KTA)) can be described in a similar way, but one needs the polar θ and the azimuthal angle ϕ for a complete description.

2.3.2 Walk off and thermal phase matching

The angle tuning of the critical phase matching unfortunately comes with a problem. If the beams don't follow either the optical axis or its normal (meaning $\theta = 0°$ or $90°$) as rather an angle in between, the direction of energy flow (described by the Poynting vector) is not exactly the same as the direction of propagation following the wave vector $\vec{k}$. This phenomenon is called spatial walk off. This means, that the beams not necessarily overlap

over the full size of the crystal. To quantify this effect, the angle of walk off ρ between the $\vec{P}$ and $\vec{k}$ can be calculated as [49]:

$$\rho(\theta) = \pm(\arctan((n_0/n_e)^2 \tan(\theta)) - \theta) \tag{2.34}$$

For Gaussian beams with beam waist radius w_0, the characteristic walk-off length l_a can be written as:

$$l_a = \frac{\sqrt{\pi} w_0}{\rho} \tag{2.35}$$

The only way to avoid this effect is to use the crystals under $\theta = 0°$ or $90°$, as mentioned. Some crystals' extraordinary refractive index strongly depends on the temperature. In that way, the crystal does not need to be tilted to gain phase matching as rather heated to the right temperature. Therefore, this method is called thermal or non-critical phase matching. A very well known crystal for thermal phase matching is Lithium Triborate (LBO), which we use also in the setup explained in section 3.2.6.

2.3.3 Ultrashort pulses and broadband phase matching

All the considerations for phase matching in the previous sections were done for monochromatic light. However, in the laser system described in the next chapter, we aim for the generation of ultrashort pulses with pulse durations below 100 femtoseconds. Ultrashort pulses can only be achieved if we have on the one hand a large spectral bandwidth and on the other hand, all the participating wavelengths within this spectral bandwidth need to have a specific phase relation to each other. This is due to the fact, that the shortest possible pulse duration achievable with a certain bandwidth is given by:

$$\Delta\tau\Delta\nu = \Delta\tau\Delta\lambda\frac{c}{\lambda^2} = tbwp \tag{2.36}$$

$\Delta\tau$ is the pulse duration (FWHM), $\Delta\nu = \Delta\lambda\frac{c}{\lambda^2}$ is the spectral bandwidth in frequency and wavelength (FWHM), respectively and *tbwp* is the time-bandwidth product, which is constant and for Gaussian pulses approximately 0.44. So, if we want to generate a short pulse, this pulse needs to have a broad spectral bandwidth. For example, if we want to generate a Gaussian pulse at a central wavelength of 800 nm with a pulse duration of less than 50 fs, the spectral bandwidth needs to be larger than 18.8 nm.
The colors or wavelengths within this spectrum will have a certain phase. For the optimal case, the phases of the colors interfere such, that all the peaks of the electric fields of the participating wavelengths overlap constructively in one point of time. In that case, the phase of all wavelengths is zero. Hence, the pulse duration becomes minimal and the duration is therefore bandwidth limited. To reach this optimal condition, there are several

approaches which will be discussed in detail in the chapters 2.4 and 2.5
Regarding the bandwidth of the amplification process, we need to look at the phase matching condition once again. This was defined for an explicit central wavelength in equation 2.16. If we want to investigate the effective interaction bandwidth, we can expand Δk in Taylor series around the central wavelengths ω_i, ω_p and ω_s:

$$\Delta k = \Delta k_0 + \frac{\partial k_p}{\partial \omega_p}\Delta\omega_p - \frac{\partial k_s}{\partial \omega_s}\Delta\omega_s - \frac{\partial k_i}{\partial \omega_i}\Delta\omega_i + \tag{2.37}$$

$$+ \frac{\partial^2 k_p}{\partial \omega_p^2}\Delta\omega_p^2 - \frac{\partial^2 k_s}{\partial \omega_s^2}\Delta\omega_s^2 - \frac{\partial^2 k_i}{\partial \omega_i^2}\Delta\omega_i^2 + ... \tag{2.38}$$

where Δk_0 is the phase mismatch for the central wavelengths of the three waves. The first derivatives of the wave vectors are the inverse group velocity v_g. The next order is the group velocity dispersion (GVD) and so forth.
We can make a few assumptions to simplify the equation:
First, we can achieve phase matching for the central wavelengths with either critical or non-critical phase matching, meaning $\Delta k_0 = 0$.
Second, for DFG and OPA processes, the pump bandwidth usually is much smaller than the bandwidths of signal and idler and can be assumed to vanish, $\Delta\omega_s, \Delta\omega_i \gg \Delta\omega_p \approx 0$.
Third, we propose energy conservation for the spectral width: $\Delta\omega_i = \Delta\omega_p - \Delta\omega_s \approx -\Delta\omega_s$.
Then we can write Δk to first order expansion as:

$$\Delta k = \left(\frac{1}{v_{gi}} - \frac{1}{v_{gs}}\right)\Delta\omega_s \tag{2.39}$$

where v_{gi} and v_{gs} are the group velocities of signal and idler waves. This issue cannot be tackled by critical or non-critical phase matching for themselves, because the angle or temperature in critical or non-critical phase matching, respectively, already needs to be chosen such that Δk_0 vanishes. But if we introduce another degree of freedom, we also have a chance of canceling this out. What can be done is to introduce an angle between seed and pump beam within the crystal. With this approach, one can mitigate the effects of the walk-off within the crystal and can also amplify a spectral bandwidth phase matched. This geometrical modification will be discussed in the next section.

2.3.4 Noncollinear Optical Parametric Amplifier

The idea of noncollinear optical parametric amplification (NOPA) is to introduce an angle α between the pump and the signal beam in an OPA process (see figure 2.8a). By doing so, another degree of freedom is created, which allows to match the group velocities of the participating laser pulses. This

was first tested successfully in 1995 by G. M. Gale et al [57]. The newly generated idler needs to fulfill momentum conservation and is thereby generated under an angle Ω in regard to the signal such that $\vec{k_s} + \vec{k_i} = \vec{k_p}$.

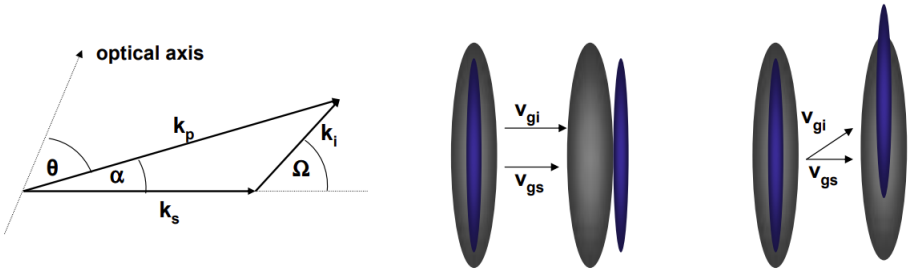

(a) **(b)** **(c)**

Figure 2.8: a) Illustration of the noncollinear geometry within NOPA . The wave vectors of signal k_s and pump k_p insert a noncollinearity angle α, thereby the idler (following k_i) is generated under an angle Ω . b) Group velocity mismatch in collinear geometry between signal and idler wave. c) Group velocity matching in noncollinear geometry. (Figures taken from [46])

From equation 2.39 we know, to achieve phase matching for a broader bandwidth, we need to match the group velocities of the signal and idler beam throughout the crystal. If we analyze the effect on the wave vectors in the noncollinear geometry, we can calculate [58]:

$$\Delta k_{\parallel} = k_p \cos\alpha - k_s - k_i \cos\Omega \tag{2.40}$$

$$\Delta k_{\perp} = k_p \sin\alpha - k_i \sin\Omega \tag{2.41}$$

with $\Delta k_{\parallel}$ and $\Delta k_{\perp}$ being the phase mismatch in parallel and perpendicular direction to the propagation direction of the signal, respectively. For the case of perfect phase matching, these terms are set to 0 and we can find the simple equation [49]:

$$v_{gs} = v_{gi} \cos\Omega \tag{2.42}$$

The group velocity of the idler, which is inclined against the signal by Ω, is projected onto the signal (visualized in figure 2.8 b and c). Hence, the velocity in the direction of the signal is matched for the cost of a displacement perpendicular to it.
Due to the spectral bandwidth of the signal, the wave vector of the signal has also an interval of lengths. This means, to fulfill the equation $\vec{k_s} + \vec{k_i} = \vec{k_p}$ also an interval of Ω is needed as displayed in figure 2.9. Since the bandwidth of the pump is considered small and the noncollinearity angle α is fixed, the generated idler beam is dispersed with angle (see fig. 2.10).

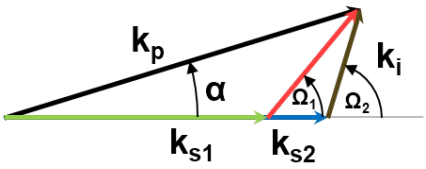

Figure 2.9: Depiction of the signal wavelength dependency of Ω in a NOPA resulting in an angular dispersed idler beam.

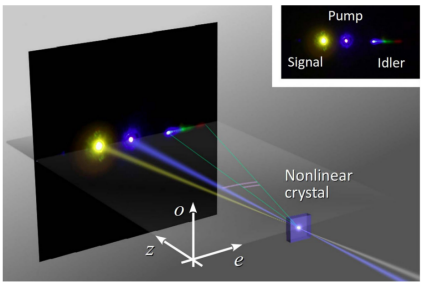

Figure 2.10: Visualization of the angularly dispersed idler beam after a NOPA process (Graphic taken from [49]).

Usually, the dispersed idler is no big problem, because the focus of this process is within the amplification of the seed beam and after the process, the idler and pump beams are dumped anyway. But this means, that this geometry of amplification poses more complications for a DFG process, in which the goal is to use the idler instead of the signal beam after the amplification.
However, another advantage worth mentioning for this geometry is that the noncollinearity angle can be chosen in the same direction as the walk-off within the nonlinear crystal. Thereby, the bandwidth of the amplified signal spectrum can be optimized and the effects of the walk-off can be mitigated or even completely avoided. A practical advantage is, since the pump, signal and idler exit the crystal in different propagation directions, splitting the individual wavelengths for later purposes or just to dump the unwanted wavelengths can be done without interfering with the amplified signal beam.

2.4 Chirped pulse amplification and optical parametric chirped pulse amplification

In this chapter, we look at the pulse duration of the laser pulses, which we amplify. In this work, we aim for laser pulses with high intensities. This means, we want to amplify the pulses to gain high energy and also the generated pulses need to have a broad spectrum, which can be compressed to form ultrashort pulses. However, the intensities reachable with commercial systems nowadays can be easily close to the optical damage thresholds of the optics used in the beam path. There are two options to avoid optical damages induced by the laser pulses: The beam diameter or the pulse duration can be increased to reduce the intensity. For damage effects which correlate to accumulating energy in the optics and thereby heating them, an increase in the pulse duration is no solution, because these issues depend on

the average power. To counter these problems, the beam size needs to be increased to distribute the thermal load and/or the optics need to be cooled. For problems arising with intensity, like electron avalanche breakdown or dielectric breakdown, the pulses may be stretched (also-called chirped) to reduce the intensity and prevent damage to the optics. Then the pulses can be amplified and after amplification, compressed again to have intense pulses with high temporal resolution for experiments. This procedure of stretching, amplification and compression is called chirped pulse amplification (CPA). The concept of chirping the laser pulses before amplification and an effective compression afterwards was first successfully shown in 1985 by Gérard Mourou and Donna Strickland [5]. This development pushed a rapid surge in maximum focused intensity reported in the following years and was therefore awarded a Nobel Prize in physics in 2018. The chirping can be done

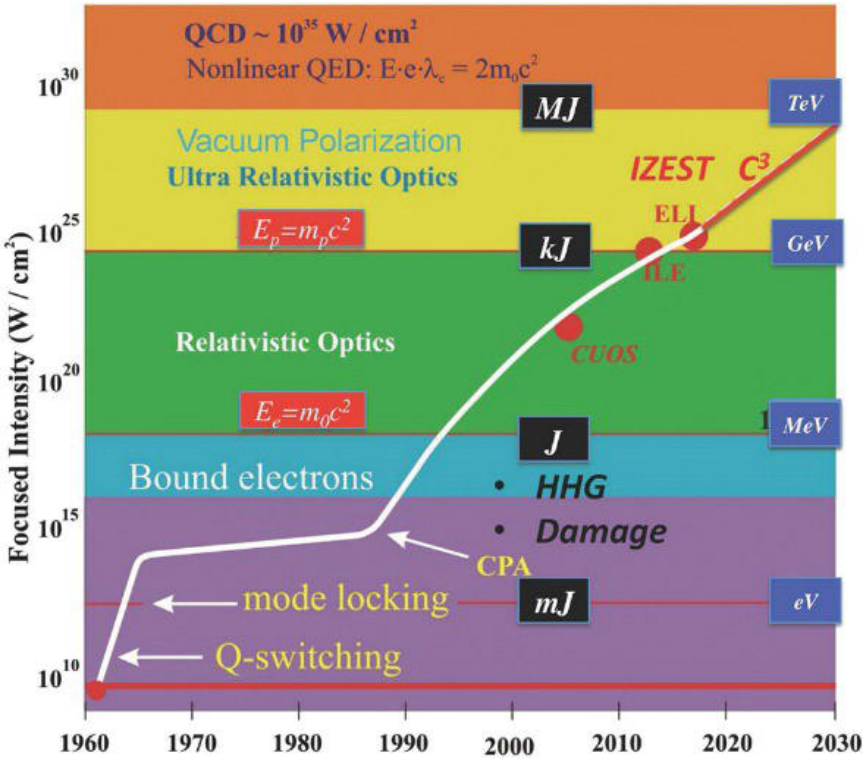

Figure 2.11: Chronology of the growth of focused laser intensity (Graphic taken from [59]).

in several ways as will be discussed in chapter 2.5, but the tricky part lies with a compatible compression. Only two years after Mourou's publication, Oscar Eduardo Martinez came up with an elegant solution to this issue [60]. He used a grating compressor assembly, but inserted a lens such that the grating was standing in the imaginary plane. Therefore, the dispersion gen-

erated, was just the negative of a grating compressor without the lens, hence the dispersion can be fully compensated by one without the lens. In this work, the stretching and compression for the pump channel as described in chapter 3.2 was done following this exact idea.
CPA is a great tool for the amplification of narrow bandwidths of a few nanometers because the amplified bandwidth is determined by the bandwidth of the participating electronic states. Also, the pumping of the laser active medium can be done comparably easy and efficiently with flash lamps of the correct wavelength. In that sense, this is the perfect solution for generating energetic pump pulses for a later OPCPA . A prominent material for this cause is Ytterbium doped laser gain media, because of its simple electronic level structure, its small quantum defect, allowing for high power efficiencies and a relatively large upper-state lifetime of about 1-2 ms, which is beneficial for Q switching. [61]
However, there are also drawbacks of this method. The amplification bandwidth within an CPA is usually limited and centered around a gain medium dependent central wavelength. This means, if light is amplified by CPA , the center wavelength of the gain medium's transition wavelength is amplified best. Hence, the broader the bandwidth of the beam, the lower is the amplification at the wings of the spectrum. The result of this effect is, that the outgoing beam will have a narrower spectrum than the incoming one and is therefore called "gain narrowing". For higher amplification factors, this leads to stronger bandwidth losses.
Another point to consider is the Stokes shift of the laser gain medium. The medium is pumped with flashlamps with a photon energy of more than the laser pulses which shall be amplified. Therefore the difference in photon energy is deposited as heat in the active medium (Stokes shift). This leads to thermal load, which needs to be dissipated. For this reason, these systems usually have quite complex designs (such as thin disk or slab geometry, mostly with multipass configuration) to efficiently cool the laser medium. This thermal load also has another effect, which is thermal lensing. By pumping and thereby heating inhomogeneously or just by the beam itself, a gradient is induced to the refractive index. For reasons of homogeneity of temperature and best heat dissipation, the active medium is to be kept thin.
Another way of using a chirped pulse is if the amplification process is not done with a pumped laser medium but rather with an optical parametric amplifier. This process is then called optical parametric chirped pulse amplification (OPCPA). This idea was first published in 1992 by A. Dubietis et al [62]. In this situation, the chirp of the beam follows another logic. Here, chirp is introduced to a seed pulse to match the pulse duration of the pump pulse. In this work, we aim for pulse durations shorter than 100 fs. But even fully compressed, the narrow spectral bandwidth of the pump only allows for a pulse duration of about 1.2 ps. Therefore, to be able to use the full

pump energy for the OPCPA processes, we need to stretch the seed pulses as it is discussed in chapters 3.3.1.
Positive aspects of OPCPA are: broad amplification bandwidth, high single pass amplification and high power capability. In comparison to CPA , in OPCPA the amplification bandwidth is given by the phase matching condition. In noncollinear geometry, this can be tuned to support over 100 THz in frequency bandwidth, allowing for pulses as short as a few femtoseconds. As calculated in equation 2.23, the amplification of the seed is mainly determined by the intensity of the pump, the phase matching and the d_{eff} of the nonlinear crystal. Therefore, the gain can reach several orders of magnitude with only a few millimeters of crystal length and does not need any complex multipass geometry.
OPCPA can also handle high average powers, because the difference in photon energy between the pump and the seed is not stored in the crystal as rather emitted with a newly generated idler pulse. So, if the crystal is not naturally absorbing any of the participating light waves, the energy of the light waves is just redistributed in the process and not lost. In consequence, the OPCPA is independent on the average power and is therefore a great tool to reach high intensities together with high repetition rates.
However, also OPCPA comes with its own challenges:

- Phase matching: To reach high efficiency of the amplification process and a desired broad spectral bandwidth, the phase matching condition needs to be fulfilled even to higher orders around their central wavelength. This means a careful design of the optical setup in regard to choosing the optimal nonlinear crystal for the process, its internal crystal angles and potential noncollinearity angles for broadband amplification.

- Pump requirements: For this process to work exactly as intended, there are strong conditions for the pump beams. In comparison to CPA , in OPCPA there are no electronic states to populate with the pump pulse. Therefore, only where there is intensity of the pump in time and space, there is also amplification. This means, the pump pulse needs to be equal in space as well as in time. And any movement or jitter has influence on the reached amplification efficiency.

- Efficiency: In theory, the pump can be depleted completely. However, in reality we are using Gaussian shaped pulses. Due to higher gain with higher pump intensity, the pump is depleted earlier in the center, where there is maximum intensity. Also, the pump photon is split in a seed photon and an idler photon. Usually, only one of the photons is of further interest and the other one is dumped, therefore reducing efficiency even more. Over all, one can calculate with a maximum of 25% of the energy of the pump to be used to amplify the seed and

generate the idler.

2.5 Pulse chirping and dispersion management

To make the CPA and OPCPA a reality, we need to have a handle on the pulse duration. This is done by chirping the pulse, meaning we are introducing dispersion to the pulse. For one, this is always done if the beam is sent through any material in the beam path. Since the refractive index of a material is dependent on the wavelength, for a laser pulse with a certain spectral bandwidth, the different spectral components of the pulse will experience a different refractive index. Thereby, the pulse becomes dispersed. An even stronger dispersing effect is achieved, if the pulse is sent through an optical system made with gratings or prisms. Within such systems, the spectral components of the beam are intentionally split and will travel a different distance.
To quantify the effect of the different dispersion generating objects in the beam path, it is convenient to look at an ultrashort laser pulse in the frequency domain. Here, the frequency dependent electric field of the pulse is defined as:

$$E(\omega) = A(\omega)\exp(i\phi(\omega)) \tag{2.43}$$

where $A(\omega)$ is the spectral amplitude and $\phi(\omega)$ is the spectral phase. One usually expands the phase in a Taylor series to specify the effects on the pulse duration:

$$\begin{aligned}\phi(\omega) = & \underbrace{\phi_0}_{\text{Carrier envelope phase}} + \underbrace{\phi_1(\omega-\omega_0)}_{\text{Group delay}} + \frac{1}{2}\underbrace{\phi_2(\omega-\omega_0)^2}_{\text{Group delay dispersion}} \\ & + \frac{1}{6}\underbrace{\phi_3(\omega-\omega_0)^3}_{\text{Third order dispersion}} + \underbrace{\dots}_{\text{Higher order dispersion}}\end{aligned} \tag{2.44}$$

where $\phi_n = \left(\frac{d^n\phi}{d\omega^n}\right)$. In this formula, the individual contributions of the derivatives of the phase produce distinguishable results:

- ϕ_0 is called the carrier envelope phase (CEP) and determines the phase of the electric field of the pulse within the envelope of the pulse. The CEP has no contribution to the pulse duration.

- ϕ_1 is called the group delay (GD) and determines the temporal position of the pulse relative to an arbitrary moment in time. This contribution is also not modifying the pulse duration, but can delay the pulse as a whole. For processes, which depend on temporal overlap of two

pulses, the influence of group delay of materials needs to be taken into account. The effect can be countered by using a delay stage and adding more distance to one of the beams.

- ϕ_2 is the quadratic phase and is referred to as group delay dispersion (GDD) or just second order dispersion (SOD). This term is mainly responsible for the chirping of the pulse. It means, that the different spectral components of the pulse experience a different group delay and are therefore pushed apart. In consequence, the pulse becomes longer. Another notation is the group velocity dispersion (GVD), which describes the GDD per unit distance, which is commonly used to report the dispersion introduced by material.

- ϕ_3 is the cubic term and is referred to as third order dispersion (TOD). It contributes to the stretching of the pulse as well, but it creates also a distortion of it. The pure TOD is responsible for pre- and post-pulses to the main pulse. The cancellation of the GDD and TOD is of central importance to compress a pulse back to its optimal pulse duration.

- All higher order contributions to the phase are difficult to compensate. A good way to address them adequately is with an Acousto-Optic Programmable Dispersive Filter, which can modulate the phase of a pulse to a high degree [63].

To summarize, for CPA or OPCPA , the pulse needs to be stretched by an optical assembly, i.e. a grating stretcher. Most important for the pulse duration are GDD and TOD . It does not matter, whether this assembly is generating positive or negative GDD and TOD . Negative GDD means that shorter wavelengths of the pulse travel faster than the longer wavelengths, while positive GDD means the opposite. However, if the pulse needs to be compressed later on, the same amount of GDD and TOD but with inverse sign needs to be added to the pulse, which may cause problems. To find a matching set of a stretcher and a compressor is not always possible and needs to be carefully investigated before starting to set up a laser system. In the following sections, I will describe the common stretching and compression options, which are also used in the laser system described in chapter 3.

2.5.1 Material dispersion

Any optic which is passed by the beam is contributing to the overall dispersion of the pulse. This is because the refractive index is dependent on the wavelength. For common glasses or transmittive media, the dispersion of the refractive index can be expressed with Sellmeier coefficients B_n and C_n in this form:

$$n^2(\lambda) = 1 + \frac{B_1\lambda^2}{\lambda^2 - C_1} + \frac{B_2\lambda^2}{\lambda^2 - C_2} + \frac{B_3\lambda^2}{\lambda^2 - C_3} \tag{2.45}$$

The exact values of the coefficients are dependent on the material itself. The corresponding GVD and TOD of any material can be calculated by partial derivation of the refractive index by λ and can be written as:

$$\mathrm{GVD}(\lambda) = \frac{\lambda^3}{2\pi c^2}\frac{\partial^2 n(\lambda)}{\partial \lambda^2} \tag{2.46}$$

$$\mathrm{TOD}(\lambda) = -\frac{\lambda^4}{4\pi^2 c^3}\left[3\frac{\mathrm{d}^2 n}{\mathrm{d}\lambda^2} + \lambda\frac{\mathrm{d}^3 n}{\mathrm{d}\lambda^3}\right] \tag{2.47}$$

An example of common glasses are Sapphire, BK7, Fused Silica or Calcium Fluorite. For Sapphire, the Sellmeier formula in micrometers reads:

$$n^2(\lambda) = 1 + \frac{1.4313493\lambda^2}{\lambda^2 - 0.0726631^2} + \frac{0.65054713\lambda^2}{\lambda^2 - 0.1193242^2} + \frac{5.3414021\lambda^2}{\lambda^2 - 18.028251^2} \tag{2.48}$$

In figure 2.12, it can be seen, that the curvature of the dispersion of Sapphire is positive for lower wavelengths than 1.314 µm and negative for larger wavelengths. The curvature is directly proportional to the GVD of the material. This is an important point for the setup described later and will be discussed in more detail in chapter 3.3.1.

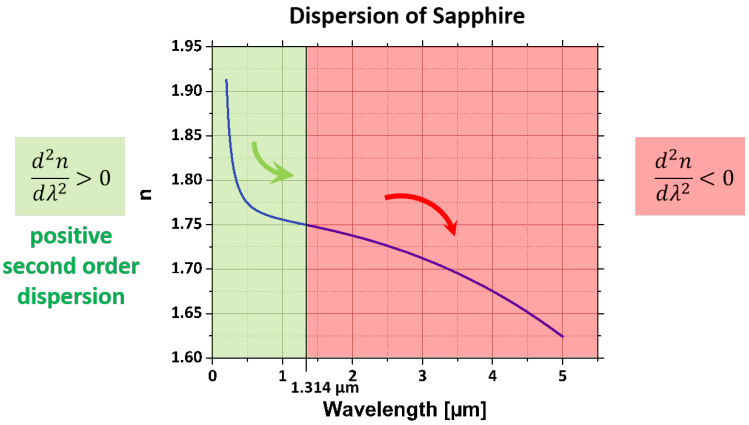

Figure 2.12: Real part of the refractive index of Sapphire as a function of wavelength. Sapphire is taken as a representative for common glasses (like BK7 or fused silica). For wavelengths lower than 1.314 µm the induced SOD in Sapphire is positive, for longer wavelengths it's negative.

2.5.2 Grating pair

Another solution to chirp a laser pulse is to use a pair of gratings. If a laser beam is diffracted off a grating, all other orders of diffraction apart from the 0th are strongly angularly dispersed and follow the formula:

$$m\lambda = d_G(\sin\alpha + \sin\beta) \tag{2.49}$$

In this formula, m is the order of the diffraction, d_G is the groove spacing or also d_G^{-1} is the lines per millimeter, α is the incoming angle and β the outgoing angle. The resulting effect of a diffraction grating is shown in figure 2.13. If a second grating is placed parallel to the first, the angular dispersion

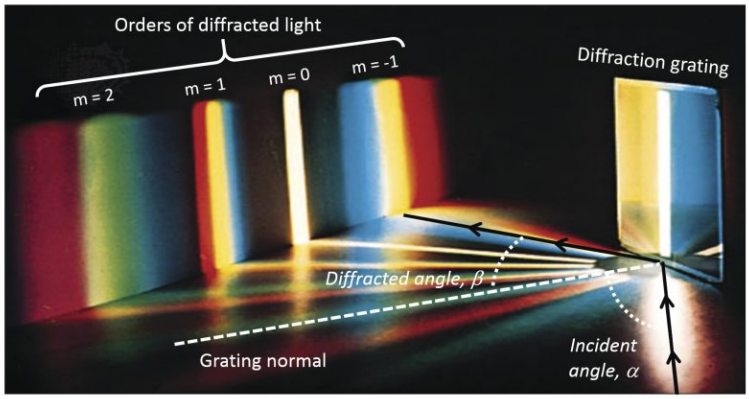

Figure 2.13: Visualization of the dispersion effect of a diffraction grating. (Image is taken from Newport website [64].)

can be compensated. If done so, the colors of the beam will still be spatially dispersed. Usually, a retroreflector is used then, which will send the beam up and then back to both gratings and therefore reshaping the beam to its original shape.

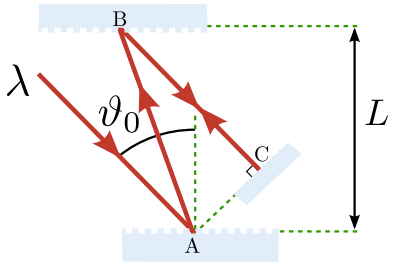

Figure 2.14: Schematic working principle of a grating compressor. The incident beam is angularly dispersed by the first grating and parallelized by the second. With that, a spatial chirp is introduced, which is eliminated by sending the beam back to both of the gratings by a retroreflector. Image is taken from Optics toolbox website [65].

The effect of the configuration as depicted in figure 2.14 on the GDD and TOD of the laser pulse can be calculated by the formulas [66]:

$$\mathrm{GDD}(\lambda) = -\frac{\lambda^3 L}{\pi c^2 d_G^2}\left[1-\left(\frac{\lambda}{d}-\sin\vartheta_0\right)^2\right]^{-\frac{3}{2}} \tag{2.50}$$

$$\mathrm{TOD}(\lambda) = -\frac{3\lambda}{2\pi c}\frac{1+\frac{\lambda}{d_G}\sin\vartheta_0-\sin^2\vartheta_0}{1-\left(\frac{\lambda}{d_G}-\sin\vartheta_0\right)^2}\cdot\mathrm{GDD}(\lambda) \tag{2.51}$$

Here, ϑ_0 is the incoming angle onto the first prism and L is the distance between the prisms. If these gratings are used for laser application, only one diffraction order is important. That is why, the used gratings are usually optimized to reflect almost all incoming light of a specific so-called 'blazing' wavelength to this one diffraction order. This involves modifying the groove profile, including facet angles, shapes and/or depths. However, even with this optimization, the efficiency of such kind of compressors is typically not higher than 80 %.
The advantage of a grating compressor is, that the dispersing effect is larger compared to equal sized other dispersion systems.
With a grating compressor of such kind, it is only possible to generate negative GDD and positive TOD. The only way to invert this is by O. Martinez [60] idea of placing the grating in the imaginary plane of a concave mirror to invert the dispersion effect. This idea was also used and is explained in the chapters 3.2.2 and 3.2.5.

2.5.3 Prism pair

With a prism pair, the dispersion is imposed by refraction into the material, in contrast to the diffraction off a grating only on the surface of the

material. Due to the wavelength dependence of the refractive index, shorter wavelengths will have higher refraction angles than longer ones. Similar to the grating assembly, a second prism is placed in the path to compensate the angular dispersion. Also here, to return the beam shape to its original form and to make the assembly more compact, a retroreflector is placed in the beam path and the two prisms are passed through again. For this type of dispersion assembly, it is easiest to calculate the resulting GDD /TOD by taking the second/third derivative of the optical path with respect to the wavelength. The corresponding formulas are [66]:

$$\mathrm{GDD} = \frac{\mathrm{d}^2\phi(\omega)}{\mathrm{d}\omega^2} = \frac{\lambda^3}{2\pi c^2}\frac{\mathrm{d}^2 P}{\mathrm{d}\lambda^2} \tag{2.52}$$

$$\mathrm{TOD} = \frac{\mathrm{d}^3\phi(\omega)}{\mathrm{d}\omega^3} = -\frac{\lambda^4}{4\pi^2 c^3}\left[3\frac{\mathrm{d}^2 P}{\mathrm{d}\lambda^2} + \lambda\frac{\mathrm{d}^3 P}{\mathrm{d}\lambda^3}\right] \tag{2.53}$$

With the optical path being:

$$P = 2\left[n(\lambda)P_{AB} + P_{BC} + n(\lambda)P_{CD} + P_{DE}\right] \tag{2.54}$$

P_{AB}, P_{BC}, P_{CD} and P_{DE} correspond to the path lengths between two points described in figure 2.15.

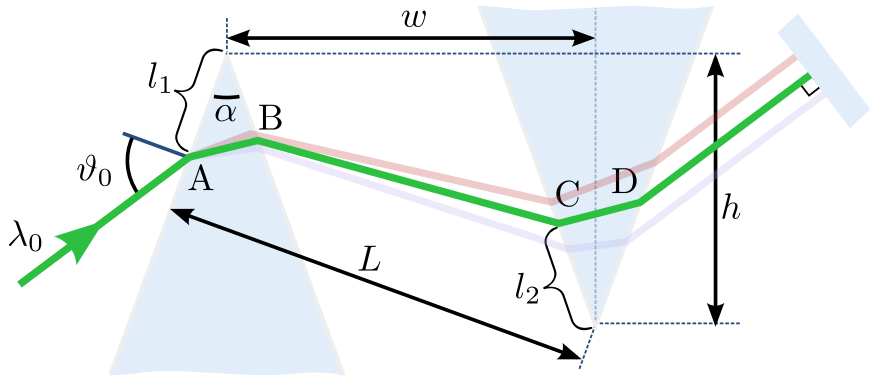

Figure 2.15: Schematic working principle of a prism compressor. Similar to the working principle of the grating compressor (see figure 2.14), the incident beam is angularly dispersed by the first prism and parallelized by the second. With that, a spatial chirp is introduced, which is eliminated by sending the beam back through both prisms by a retroreflector. (Image is taken from Optics toolbox website [65]).

The dispersion generated in a prism assembly has two contributions: One from the material the beam has to transmit and another from in between the prisms. The path within the prisms will generate positive GDD and TOD , the path in between the prisms, generates negative GDD and TOD . Therefore, the prism setup may be fine-tuned by inserting the beam deeper

into the prisms (changing l_1 for the first prism and h for the second prism in figure 2.15) and by modulating the distance between both prisms (changing w in figure 2.15).
Another advantage is, that a prism assembly can be very efficient. If the incoming light is p-polarized, the prisms can be entered under Brewster angle, minimizing the reflection off the surface. Therefore, the efficiency of a prism assembly can exceed 90%.
A possible disadvantage arises for high intensities of the laser beam. Since, the beam needs to be transmitted through the material of the prisms, the beam may induce unwanted self focusing (SF) and decrease in size throughout the path. Details about this effect will be discussed in section 2.6.
In general, the generated dispersion of the prism pair is less than the dispersion generated by a grating pair. For example, if the goal is to generate a negative GDD of 11000 fs^2 for a laser beam with a CWL of 1030 nm, what are the dimensions for a prism or grating compressor?
A prism pair made with a strongly dispersive glass like SF10 in Brewster configuration (meaning, the incoming angle into the first prism is equal to the outgoing one) the prisms need a separation w of about 400 mm. While a grating pair with an incoming angle of 60° and a density of grooves of 1000 lines/mm would need only a distance of 6 mm.

2.6 Effects of third order nonlinearities

If strong electric fields are present, one needs to consider also effects stemming from the third term of the polarization series $\vec{P}^{(3)}$ from equation 2.2. In frequency domain, this polarization can be written as:

$$P_i^{(3)}(\omega_4) = \epsilon_0 \sum_p \sum_{jkl} \chi_{ijkl}^{(3)}(\omega_4; \omega_1, \omega_2, \omega_3) E_j(\omega_1) E_k(\omega_2) E_l(\omega_3) \qquad (2.55)$$

With the plane wave approach and three participating incoming electric fields, following the same logic as in section 2.1. Here the sum over p indicates the possible permutations of the participating frequencies. For this work, only the following interactions were important, for which I would like to mention them:

- Sum frequency generation (SFG): $\omega_4 = \omega_1 + \omega_2 + \omega_3$
- Third harmonic generation (THG): $3\omega = \omega + \omega + \omega$
- intensity dependent refractive index: $\omega = \omega - \omega + \omega$

Sum frequency generation occurs, if three photons with individual frequencies ω_1, ω_2 and ω_3 combine to a photon with the new frequency ω_4. This process can also happen, if all the photons stem from the same laser beam

and have the same frequency. Then the process is called third harmonic generation (THG). We use this process to generate a FROG trace for our mid-IR laser light in section 3.4.3.
The intensity dependent refractive index can be understood as process, which is not generating a new wavelength or amplifying an existing one, but is changing the medium such, that the momentary refractive index is increased. Under assumption, that the electric field is polarized in x direction, the nonlinear polarization for this process reads:

$$\vec{P}_x^{(3)}(\omega) = 3\epsilon_0 \underbrace{\chi^{(3)}_{xxxx}(\omega;\omega,-\omega,\omega)}_{\stackrel{!}{=}\chi^{SF}} |E_x(\omega)|^2 E_x(\omega) \tag{2.56}$$

since $I(\omega) = 2cn_0\epsilon_0|E_x(\omega)|^2$, we can introduce an intensity dependent change to the refractive index as:

$$\Delta n_x = n_2 I(\omega) = \frac{3\chi^{SF} I(\omega)}{2c\epsilon_0 n_0(\omega)^2} \tag{2.57}$$

With that influence on the refractive index, the modified refractive index is:

$$n = n_0 + n_2 \cdot I(\omega) \tag{2.58}$$

An important note is, that for this process, the phase matching is always fulfilled. If we produce the phase matching condition as we did in equation 2.16 for this process, we have the following equation:

$$\Delta k = \vec{k}_1 - (\vec{k}_1 - \vec{k}_1 + \vec{k}_1) = 0 \tag{2.59}$$

Usually, in a laser setup, we are using laser beams with a Gaussian intensity profile. Therefore, the intensity is strongest in the center and decreases the further we are from the center. Therefore, the refractive index will be increase the strongest in the center. This generates then a lensing effect on the beam in space (Self focusing) and also a phase modulation in the frequency domain (self phase modulation).
Since this process is intrinsically phase matched, it always happens but is rarely wanted. To have an estimate about the quantity of this effect across a traversed medium with the length of L, one can calculate the so-called "B-Integral" [67]:

$$B = \frac{2\pi}{\lambda} \int_0^L n_2(z) I(z) dz \tag{2.60}$$

depending on the initial beam quality the B-integral should be kept below π in order to avoid nonlinear effects [67].
The nonlinear refractive index n_2 can only be found experimentally, but was already measured for a lot of materials.

Chapter 3

Generation of high intensity, mid infrared and near infrared pulses in four stages

For decades, light in the mid infrared region was mainly used for rotational-vibrational spectroscopy [68]. The reason for this was, that the mid infrared light is in resonance with several vibrational features of molecules, which could thereby be identified explicitly. Hence, it was used often in chemistry, biology and medicine [69–71].
For these applications, no laser source was needed as rather thermal emitters like globar systems sufficed. They are cheap and are the most easily available source of broadband light. However, they deliver incoherent light both spatially and temporally with low spectral intensity.
Some applications, such as sensing of trace elements, hyperspectral imaging or micro-spectroscopy [12–14], require higher brilliance than that of a thermal source. With globars, no high resolution imaging was possible, which is especially important for the microscopic investigation of biological samples. Later on, synchrotrons were used, which deliver the necessary high brilliance mid-IR radiation.
With the upcoming of OPCPA systems, it was then possible to generate mid-IR pulses with pulse energies in the µJ to mJ range and pulse durations ranging from picoseconds down to pulses with only a few optical cycles. Sources of this type then opened the field to time resolved vibrational spectroscopy [28, 31] and high field physics like high harmonic generation [17, 22] and laser plasma wakefield acceleration [23].
In this chapter, I want to give insight into our approach to generate a setup capable of being a suitable source for pumping vibrations in molecules and temporally resolving their effect on electron transfer dynamics, as well as being a driver laser for high harmonic generation.

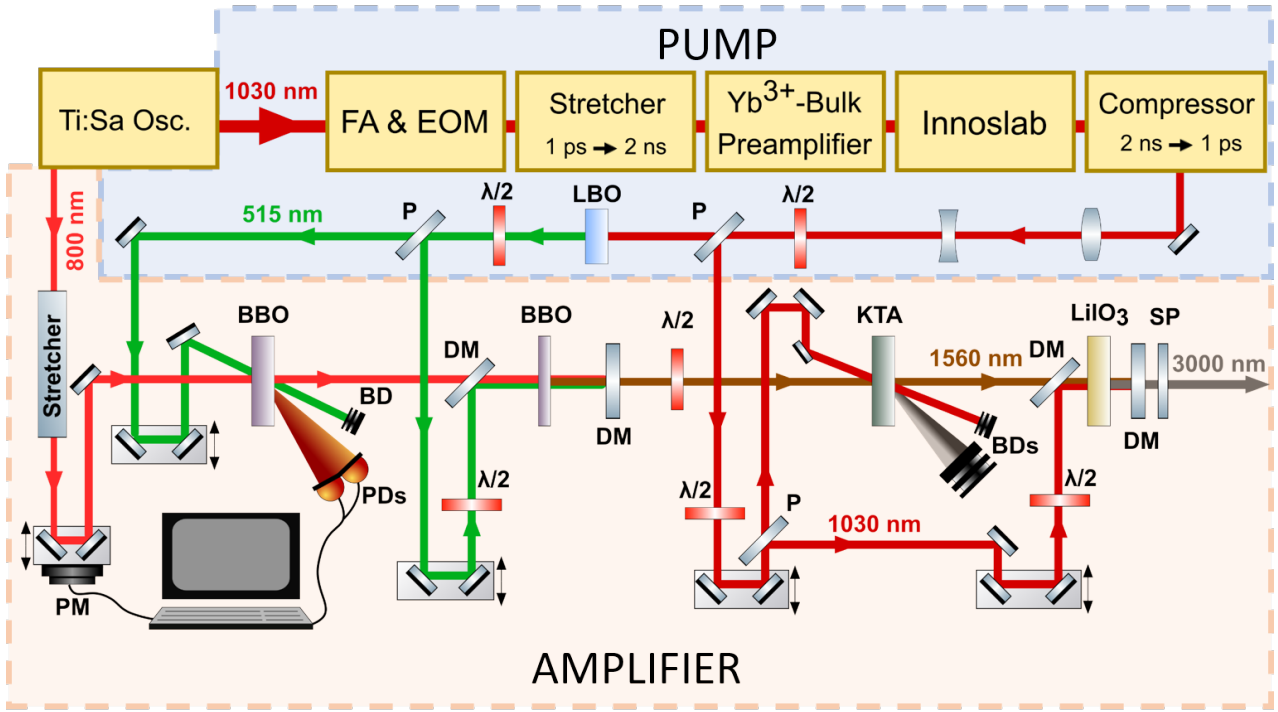

Figure 3.1: Schematic of the four stage OPCPA setup of this thesis [72]. An octave spanning Ti-Sa oscillator is used as a seed source both for the "AMPLIFIER" channel (red box) and for the "PUMP" channel (blue box). The 6 fs pulses from the Ti-Sa oscillator centered at the wavelength of 800 nm are stretched and used as seed for the four stage OPCPA , consisting of two BBO crystals followed by KTA and $LiIO_3$ stages. The pump channel is seeded with narrow band 1030 nm pulses and consists of fiber pre-amplifier with electro-optical modulator (FA & EOM), stretcher, Yb^{3+} bulk pre-amplifier, Innoslab power amplifier, and compressor. Part of the pump radiation is converted to second harmonic in a LBO crystal to pump the BBO stages. Half-wave plates ($\lambda/2$) are used to control the polarization and together with polarizers (P) to adjust pump intensities. Photo diodes (PDs) together with the computer controlled translation stage (TS) are used to set a proper delay between the pump and the amplified pulses. DM, BD, and SP stand for dichroic mirrors, beam dumps, and sapphire plate, respectively. The beam diameters are adjusted with the help of telescopes, which are not shown.

This chapter is split in four parts, an explanation of the seed laser for the system 3.1, a step by step discussion of the pump line 3.2, as well as the amplification line 3.3 and a final section about the compression of the generated pulses 3.4. A detailed overview over the OPCPA system is given in figure 3.1.

3.1 Seed laser: Ti-Sa oscillator

The system is seeded by a Titanium-Sapphire-Oscillator (or also Ti-Sa oscillator). It is the commercially available device Venteon "Pulse:One" (now Laser Quantum [73]). The oscillator is pumped with a 5 W continuous wave, frequency-doubled Nd:YAG laser with a central wavelength of 532 nm. This light is focused within the oscillator onto a thin plate of the laser medium, Titanium doped Sapphire [4]. Due to the large gain bandwidth of the Ti^{3+} ion alone, it can already yield a spectrum supporting pulse durations of about 100 fs. By reaching high enough intensities in the Ti-Sa crystal, third order nonlinear effects become relevant as discussed in section 2.6. These include self phase modulation, which broadens the spectrum even further. Due to this effect, the oscillator is able to provide an octave-spanning spectrum from about 600 nm to 1100 nm as shown in figure 3.2 which is capable of supporting sub 6 fs pulse durations.

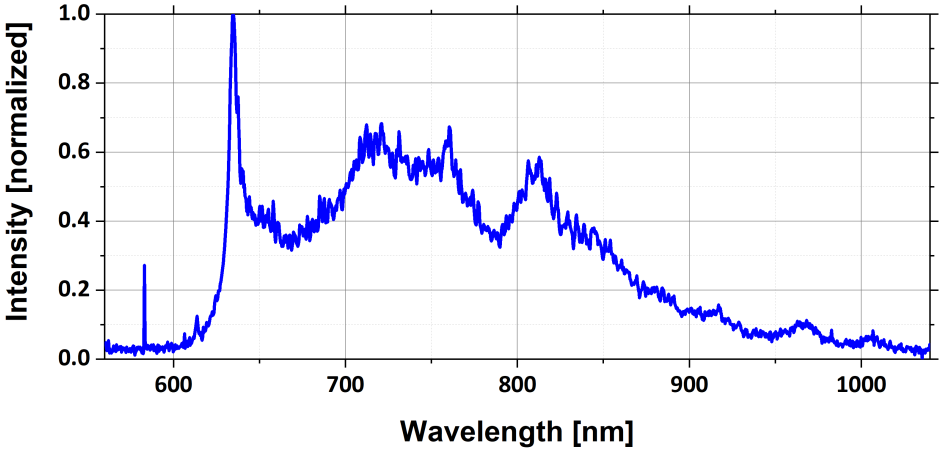

Figure 3.2: Output spectrum of the Ti-Sa oscillator.

The pulses are mode locked via soft aperture Kerr lens mode locking. This means, that only pulses with optimal spatial overlap with the pump beam are amplified in every round trip efficiently. And optimal spatial overlap is given only if the pulses are focused by themselves via Kerr lensing. Thereby, all wavelengths of the laser are in phase and an ultrashort pulse with less than 6 fs duration is generated.

To lock the carrier-envelope-phase (CEP) of the pulses, two processes are employed: An acousto optic modulator (AOM) is modulating the pump intensity slightly which changes the refractive index of the Ti-Sa gain medium and a pair of wedges may be moved in and out to artificially increase the effective length of the oscillator.
The output power of the Ti-Sa oscillator is 160 mW at a repetition rate of 80 MHz. A dichroic mirror is used to transmit a 1.7 nm thin band around 1030 nm to the fiber amplifier (seed for the "PUMP" channel, see fig. 3.1 shaded in blue) and the reflected light seeds the amplifier channel (seed for the "AMPLIFIER" channel, see fig. 3.1 shaded in red). Since the seed pulses for the pump and the amplifier channel stem from the same oscillator, we already have a stable temporal relation between these pulses. This is crucial, because already a drift of a few femtoseconds between the pump and the seed in an OPCPA stage means a different spectrum would be amplified, which in turn means different efficiency and therefore different pulse energies. Since our system consists of four of these stages and all exhibit exponential amplification, this can cause significant changes in terms of pulse to pulse energies. Because of the importance of temporal stability, we employ additionally an active delay stage to ensure this relation (see section 3.3.3).

3.2 Pump channel

To be able to feed all the individual amplification stages within the "AMPLIFIER" channel, we first need to generate a high energy pump beam which provides all stages with the required energy. The way this is achieved in this work is by the use of CPA. A narrow band split-off centered at 1030 nm (the lasing wavelength of Ytterbium) seed pulse from the Ti-Sa oscillator is stretched, amplified and compressed again. In our system, this is done within five steps:

1. Fiber preamplification (3.2.1)
2. Stretcher (3.2.2)
3. Regenerative amplifier (3.2.3)
4. Innoslab amplifier (3.2.4)
5. Compressor (3.2.5)

For the first two stages in the "AMPLIFIER" channel, we need a shorter pump wavelength to make the best use of the non-collinear amplification bandwidth of the BBO crystal. Therefore, we use a heated, temperature stabilized LBO crystal to generate the second harmonic.

3.2.1 Fiber preamplification and electro-optical modulator

Since the intensity of the Ti-Sa oscillator spectrum (fig. 3.2) already dropped to a few percent of the maximum beyond 1000 nm, it is necessary to preamplify the region around 1030 nm for further use. The fiber preamplifier consists of two fiber amplifier stages and yields a pulse energy of 3.9 nJ. Due to the narrow bandwidth, the transform limited pulse duration after this process is about 1 ps.

3.2.2 Stretcher

The stretcher in this setup is based on the idea of O. Martinez [60] and was designed and set up by Alexander Tarasevitch. The idea of the stretcher as explained in chapter 2.5 is to use the imaginary image of the grating to invert the dispersing effect of the grating, and applying a large positive group velocity dispersion to the beam. In this setup, this was carried out following the schematic below (see fig. 3.3). We use a folded design, to save

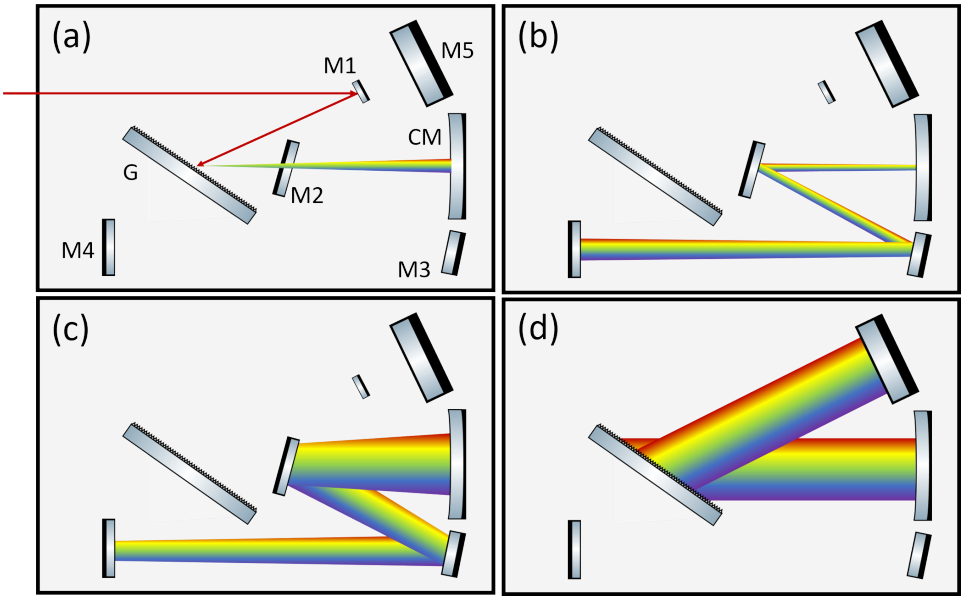

Figure 3.3: Step for step depiction of the beam path within the stretcher. Each panel shows a part of the path through the folded stretcher design. See the text for detailed description of panels a-d.

space and be able to put it into a box to avoid any air perturbations.
The beam path through the stretcher is as follows: First (displayed in fig. 3.3 (a)) the beam enters the environment from the left, is reflected on mirror M1, is dispersed from grating G and reflected from curved mirror CM to hit the mirror M2 which is slightly lower to avoid disturbing the beam path from the grating to the curved mirror. Then, the dispersed beam is forwarded

via mirrors M2 and M3 to M4, where it is reflected back almost the same path, just to be a few centimeters above M1 and being reflected by M5. M5 is then sending the beam back a second time through the full stretcher and back to M1. M1 is large enough to accommodate the incoming beam and the outgoing beam, whose beam path is about 1 cm higher than the incoming one. In that fashion, the grating and the curved mirror are used four times. The curved mirror has a focal length f of 6500 mm and focuses on the Mirror M4. This exact distance between the curved mirror and M4 is necessary, otherwise we would not have a distance of $2f$ between the curved mirror with itself and would therefore not collimate the beam again. At the position of M5, the beam is collimated, but its spectrum is horizontally split due to the grating. To stack the beam again, M5 sends the beam through all of the previous path.
The distance from the grating to the curved mirror is 1250 mm and therefore can only generate an imaginary image. The grating has 1740 grooves/mm and has a reflectance of 96.5 % per reflection. The angle between the grating perpendicular to the incoming beam is 57 degrees. Within the stretcher, the pulse duration of the beam is increased by three orders of magnitude from about 1 ps to about 2 ns.
Following the stretcher are a spherical and a cylindrical telescope, optimizing the beam shape. After this path, the pulse energy is still 0.75 nJ and is fed into a fiber to be amplified by the regenerative amplifier, which is discussed in the next section.

3.2.3 Regenerative amplifier

The regenerative amplifier is a commercial device from Amplitude with the name "ASY-s-pulse-HP" [74]. It uses direct diode pumped Ytterbium KGW as active medium. It was bought slightly modified to accept the external seed pulse, without the standard pulse compressor and in a different housing.
The working principle of this amplifier is as follows: The incoming pulse is trapped via an assembly of polarizers, lambda half plates, a Faraday rotator and a Pockels cell into a laser resonator. Since the regenerative and the Innoslab amplifier cannot amplify all the 80 million pulses per second delivered from the Ti-Sa oscillator to the required energy level, only a small portion of the pulses are captured and used in the amplifier. The combined amplifier system of the regenerative amplifier and the innoslab amplifier is capable to work with a repetition rate of 20 kHz and yield a pulse energy of 20 mJ. But to prove the working principle and for safety reasons for the staff, the full system was first built up with a repetition rate of 100 Hz and the same pulse energy of 20 mJ. This reduces the average power of the system, but the intensity of each individual pulse stays the same. Therefore, in principle, all the processes within the OPCPA stages behave the same.

However, when the maximal possible repetition rate of 20 kHz is used, side effects need to be taken care of, like thermal effects which correlate to energy deposition over time.
Within 26 roundtrips in the regenerative amplifier, the pulse is then amplified from less than 1 nJ to 1.6 mJ. After that, the Pockels cell switches the polarization of the beam, such that it is reflected from a polarizer and can escape the resonator. When the pulse exits the box of the regenerative amplifier, it is forwarded to the Innoslab amplifier. A small leak through of less than 0.5 % of a mirror is used for analysis (see fig. 3.4).

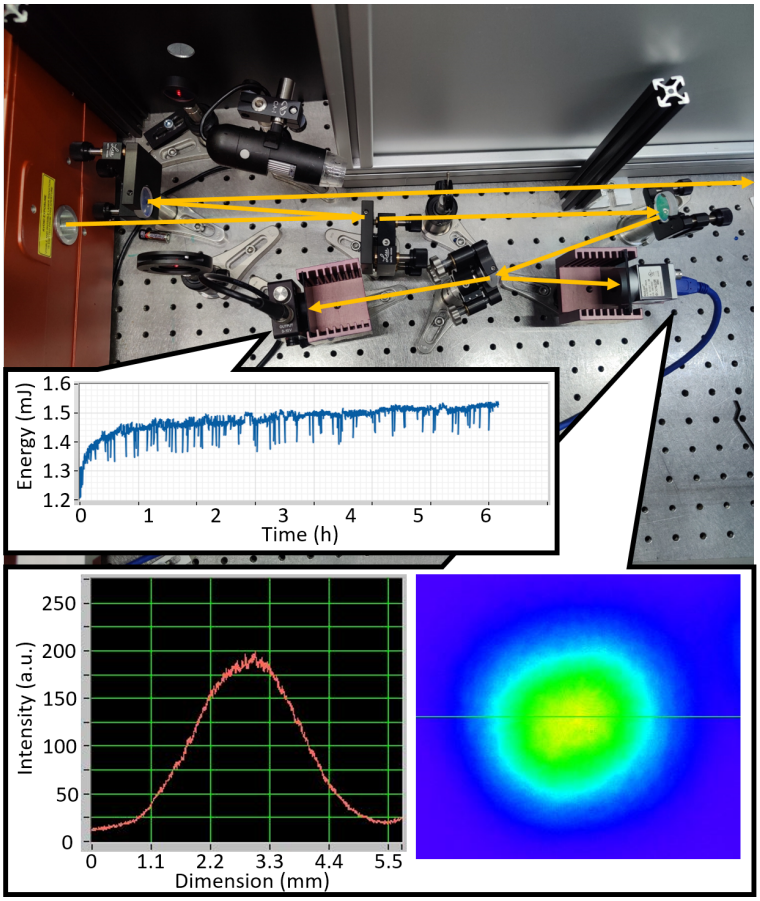

Figure 3.4: Beam analysis after Amplitude regenerative amplifier. The main beam is reflected to the Innoslab amplifier and a small leak through a mirror is used for beam shape and energy analysis.

The transmitted light is sent into a wedged glass which sends the reflected beam into a camera for beam profile analysis and the transmitted light is sent into a photo diode, which continuously measures the pulse energy.

3.2.4 Innoslab amplifier

Within the next amplifier, the pulse reaches the highest pulse energy in the system. The Innoslab amplifier is a commercially bought system from Amphos and the working principle can be described with the schematic from [75] and their paper [76] (see fig. 3.5). Within the device, the beam

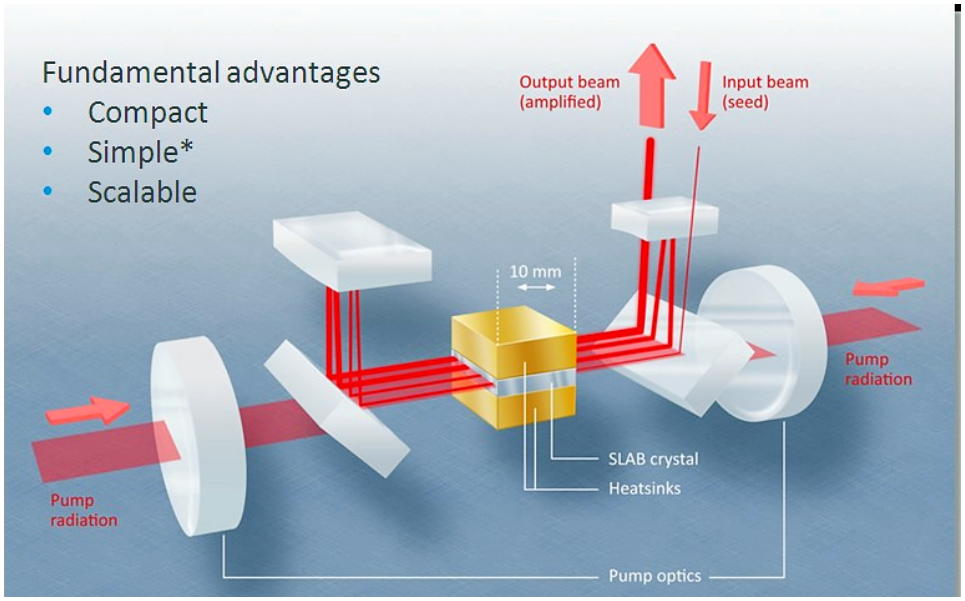

Figure 3.5: Working principle of the Innoslab amplifier (Taken from `https://www.amphos.de/technology/`).

is first adjusted for optimal amplification. The pulse energy is reduced to save the YAG crystal and other optics from harm and to guarantee the correct magnitude of amplification. After that comes a lens assembly to shape the beam to fit the crystal. The Innoslab amplifier used in the setup is designed to work with a repetition rate of 20 kHz and an output pulse energy of 20 mJ corresponding to an average power of 400 W. In this regime, the active medium generates a lot of heat which needs to be dissipated. Therefore, the medium is shaped like a thin slap and is sandwiched between two heat sinks. For the full amplification, the beam is sent through the active medium a total of 4 times. In between the amplification, the beam profile is elongated along the slab to increase the beam area and reduce the intensity to prevent electron avalanche breakdown in the crystal. The reflector mirrors for the beam are dichroic mirrors which reflect 1030 nm with a very high efficiency but transmit the pump wavelength of 940 nm. In that way, the pump can be added in the same direction as the signal light. After the amplification process, the beam is elliptic shaped and needs to be formed back to a Gaussian beam profile. For that reason, there is a

spherical and a cylindrical telescope after the Innoslab amplifier to correct the size of the beam and shape it to a round profile.

3.2.5 Compressor

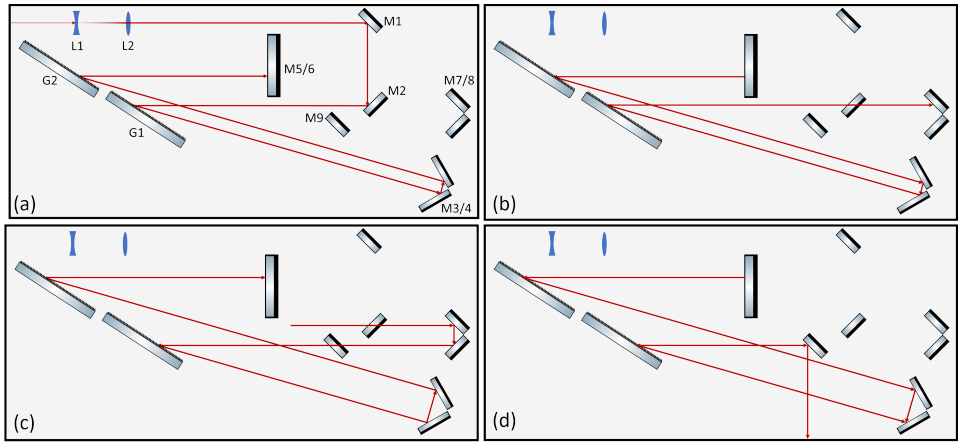

Figure 3.6: Step for step depiction of the beam path within the compressor. Each panel shows a part of the path through the folded compressor design. See the text for detailed description.

The compressor is also folded, as is the stretcher. Also here we use gratings with the same density of grooves of 1740 grooves/mm. Since the imaginary image of the gratings are used in the stretcher which are inverting and magnifying the effect of their dispersion, using the gratings now without imaging inverts the previous effect. Therefore, we compress the pulse duration back to the original.
The proceeding is depicted in figure 3.6 and unfolds as follows: First (see fig. 3.6 (a)) the beam size is increased with a telescope and is sent to grating G1 with mirrors M1 and M2. Subsequently, it is propagating over a horizontal rooftop construction M3/4 to G2 where it hits a vertical rooftop construction M5/6. One level higher (see fig. 3.6 (b)), it returns, passes over M2 and is reflected by the horizontal rooftop construction M7/8. The beam then returns to G1, but hits the grating further to the exit side of the compressor box. It returns now all the way and is reflected from M9 to the exit. In this way, both gratings are used 4 times.
It is essential that the gratings G1 and G2 are placed exactly with the same angle. Otherwise, the exiting beam may be horizontally distorted or may even miss a mirror and is lost. All horizontal beam paths, i.e. from M2 to G1, are parallel and exhibit an angle of 57 degree to the perpendicular of the grating. The outgoing beams, i.e. from G1 to M3/4, are also parallel and insert an angle of 72.5 degree to the perpendicular. The unfolded dis-

tance from G1 to G2 is 2 meters. However, the rooftop construction M3/4 is placed on a linear translation stage, which allows fine adjustment of the effective distance between G1 and G2. This assembly compresses the pulse duration from about 2 ns to 1.1 ps.

3.2.6 Energy distribution, second harmonic generation and spatial filtering

After the compressor for the pump channel, the energy of the pulse is split with combinations of a lambda half plates and polarizers and is then distributed to the individual stages. First, the pulse is split with in a relation of 1.2 mJ to 14.3 mJ for the first two stages and the last two stages. The beam with the lower energy for the first two stages is filtered spatially. This is done by weakly focusing with a telescope assembly and cutting with an iris in the focal plane. Thereby, we generate an almost Gaussian beam profile (see fig. 3.7) for the cost of 0.2 mJ to a final 1.0 mJ in pulse energy after cutting. This procedure is necessary to generate an optimal beam shape for later amplification stages with the goal of high conversion efficiency. For the beam path with the other 14.3 mJ pulse energy to the third and fourth stage, this is not a good solution, for two reasons: First, we would have also lost 1/6th of the energy corresponding to 2.4 mJ and also due to the high intensity in the focus,

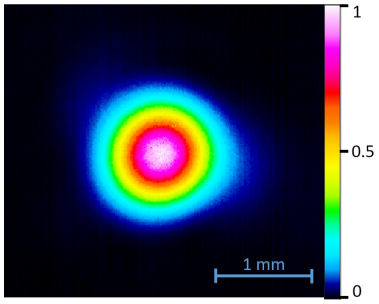

Figure 3.7: Beam profile of the fundamental laser pulse of the SHG .

	Fundamental
Wavelength [nm]	1030.0
Bandwidth [nm] (FWHM)	0.8
Pulse energy [µJ]	1000 ± 5
Beam diameter [µm] ($1/e^2$)	1380 ± 20
Pulse duration [fs] (FWHM)	1100 ± 15
Intensity [GW/cm^2]	56 ± 3

Table 3.1: Beam properties of input beam of the SHG of 1030 nm.

we would have generated plasma in mid air, disturbing later use of the laser pulses.
The laser in the lower energy channel is sent after spatial filtering into a LBO crystal, which is heated to a temperature of 191 degrees Celsius for best noncritical phase matching. The laser parameters were as follows: Af-

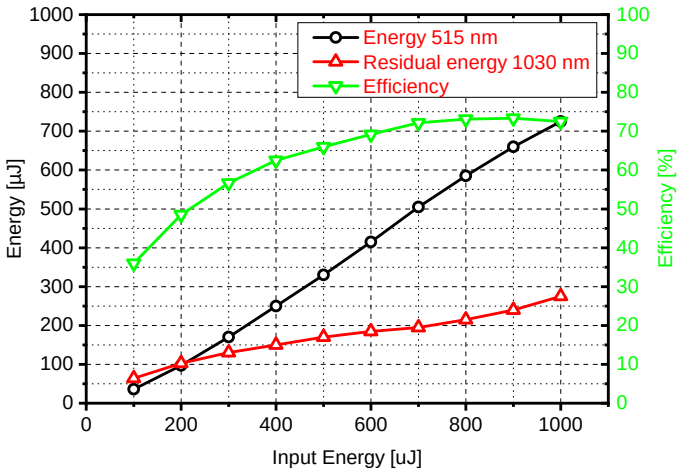

Figure 3.8: Plot of the measured output energies of residual fundamental pulses at 1030 nm (red) and newly generated SHG pulses at 515 nm (black) against the input energy of 1030 nm. Also, an efficiency (green) of the process is plotted, it was determined by division of the output SHG energy by the input fundamental energy.

ter this second harmonic generation (SHG) stage, the newly generated laser pulses at 515 nm contained 725 µJ pulse energy, yielding an efficiency of this SHG of 72.5 %. This high conversion efficiency may be explained, by driving this conversion deep into saturation, which can be seen in the efficiency measurement in figure 3.8. In this plot, the efficiency reaches a plateau starting at around 800 µJ input energy, meaning a saturated regime is reached.
After SHG , the 515 nm pulse energy is split again with a relation of 260 µJ to 300 µJ for the first and second stage. The 1030 nm pulses are dumped after separation via a dichroic mirror.
In case of the high power channel, the laser pulses are split again with a relation of 1.9 mJ to 10.5 mJ for the third and fourth amplification stage. For the third stage, the beam diameter is reduced to 4 mm $1/e^2$ with a telescope. The beam diameter after the compressor is chosen such, that for the fourth stage, no further telescope is needed to avoid self focusing in lenses.

3.3 Amplification channel

Within the amplification channel, we make use of the high energy of the pump beam and convert it into the required spectral range within four stages. First, the seed light from the Ti-Sa oscillator is stretched by bulk BK7. Then, we take care of the temporal overlap between pump and seed

pulses with a self built automatic temporal stabilization unit. After that, we distribute the pump light among two OPA and two DFG stages in following order: OPA, DFG, OPA and DFG (see fig. 3.1). Thereafter, we have three different amplified wavelength beams, which each need a customized compression.

3.3.1 Stretcher and dispersion considerations

The idea of the stretcher in this setup is to add enough positive second order dispersion (SOD) to increase the pulse duration of the seed by about three orders of magnitude, from 6 fs to about 3 ps FWHM. With this stretching, the pulse is about 3 times longer than the pump pulse and its spectrum is temporally distributed over the pulse duration (see figure 3.9).

Since the pulse duration of the pump pulse is shorter than the one of the

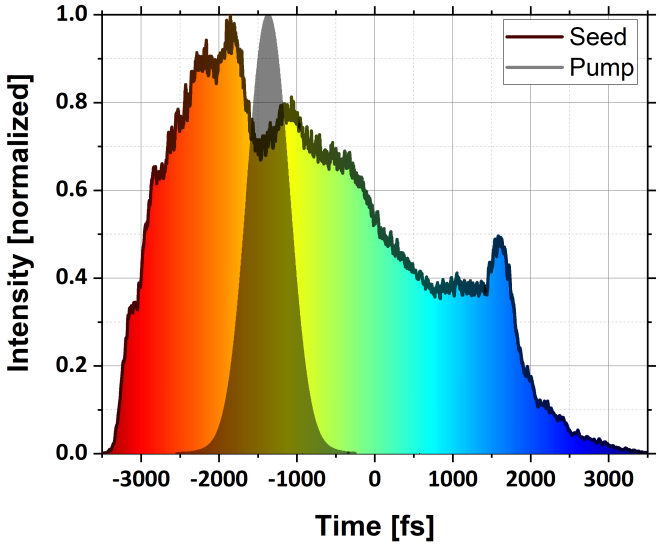

Figure 3.9: Calculation of the pulse duration of the seed (rainbow) and the pump (gray) pulse. With a dispersion calculating program by A. Tarasevitch, the effect of 10 cm BK7 on the measured spectrum was simulated on the transform limited pulse, emitted from the Ti-Sa oscillator. This yielded the intensity of the seed pulse throughout the pulse duration, as shown in the plot. Since the bandwidth of the pump pulse is only 0.8 nm FWHM centered at 515 nm (see fig. 3.14, left), the plotted pulse is already the transform-limited pulse duration, as it is used in the setup after its compression.

seed, we can select the wanted bandwidth of the Ti-Sa oscillator (see fig. 3.2). The full bandwidth of the Ti-Sa oscillator cannot be converted into the MIR range, due to the limited phase matching within the this and later

OPCPA stages. Therefore, we select the desired wavelength region in the first stage, by positioning the pump pulse at the corresponding part of the chirped seed pulse.
The pump delay with regard to the seed is chosen such that the pump is positioned slightly earlier to the peak at -1000 fs (see figure 3.9), which corresponds to the maximum intensity of the spectrum at 760 nm (see fig. 3.2). Because we amplify next to the peak of the spectrum, during the process a second peak will be generated. In this way, the amplified spectrum will have a double peak structure.
This is especially advantageous for further amplification due to the exponential nature of an amplification in an OPCPA . If a pulse with a Gaussian shaped intensity profile, in time as well as in space, is amplified with another such pulse, the amplified beam will be squeezed in space and in time, because the process is dependent on the intensities of the pulses. This means, that a stretched pulse will lose some of its spectral components and additionally will have a smaller beam diameter. However, if the pulse exhibits a local minimum in the center of the pulse duration and is amplified with a Gaussian shaped pulse, the effects compete against each other and the full bandwidth may be amplified. The amplification of the double peak structure needs to be exactly fine tuned, because if the minimum is chosen too broad, only one peak may be amplified. If it is selected too narrow, the desired effect is negligible.
The stretcher is rather simple, consisting of two 5 cm blocks of bulk BK7. This introduces +4700 fs^2 in SOD and +3200 fs^3 in TOD . Due to the broad bandwidth of the Ti-Sa oscillator, 10 cm of bulk BK7 is enough to stretch the pulse to about 3 ps.
In our case, it is very advantageous to stretch the pulse with positive SOD , because it will then be possible to compress the finally generated pulse in the mid infrared with the help of material dispersion again. This is due to two factors:
On the one hand, we will convert our signal wavelength twice in two DFG stages. For compression with material in our case, this is necessary, because with every signal wavelength change, all even orders of dispersion will switch their sign. In the generation process in the DFG stages, the longer wavelengths of the seed pulse will generate the shorter ones in the newly generated idler beam, this will swap all contributions of even order. However, contributions of odd order are unaffected. Since we have two signal changes in our OPCPA setup, the MIR laser pulses will have positive SOD and TOD as do the chirped Ti-Sa pulses.
On the other hand, common glasses invert their dispersion behavior from the visible to the infrared, as discussed in the theory section 2.5.1. This means, we can compensate the SOD which is the strongest contribution to the pulse duration, with the material dispersion of Sapphire glass. However, the TOD is positive for all common materials and can therefore not be mit-

igated in this way. This means, we will have a short pulse duration but due to the residual TOD , the pulse will exhibit an afterpulse.

3.3.2 First stage: Noncollinear OPA experimental setup

The first amplification stage is the most crucial stage for spectrum selection, bandwidth preservation, temporal stabilization and has the highest amplification factor within this setup. As depicted in the previous section, the seed beam pulse duration in this stage is chosen to be significantly longer than the pump duration to select the appropriate spectral bandwidth, which can be supported in all following amplification stages.

To use as much pulse energy as possible in this stage, it is essential to pro-

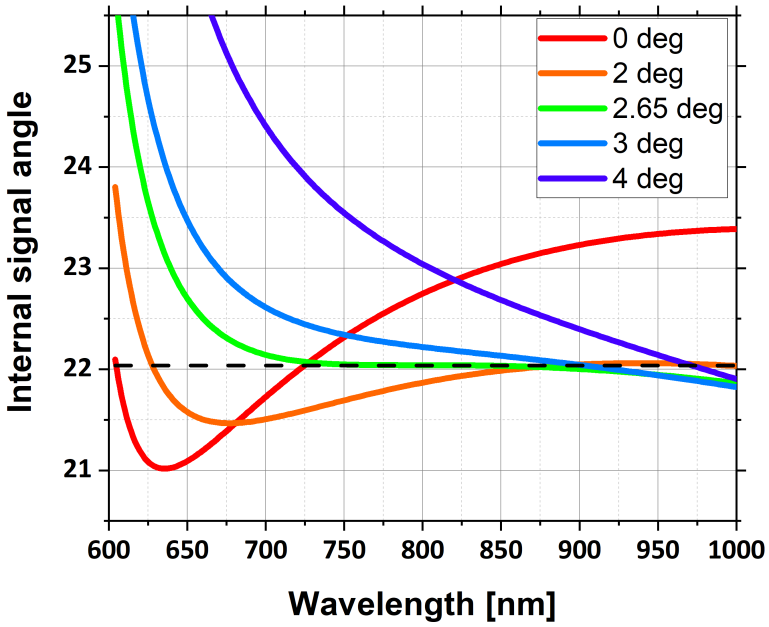

Figure 3.10: Each graph depicts the necessary phase matching angle of BBO for a corresponding wavelength in a noncollinear amplification scheme. The individual lines result from different noncollinearity angles between seed and pump beam. These graphs were calculated with SNLO [47] using a pump wavelength of 515 nm.

vide optimal phase matching between the pump, seed and idler beam. To be able to amplify the broadest possible bandwidth, this stage is used in a noncollinear fashion. In that way, we add one degree of freedom to the phase matching condition and adjust the parameters such, that phase matching is fulfilled simultaneously for a range of wavelengths at a specific optical axis angle. In figure 3.10, the necessary phase matching angles of BBO are plotted in dependency of the noncollinearity angle and the wavelength. A

plateau from about 750 nm up to over 850 nm can be found at a noncollinearity angle of 2.65 degrees and an internal signal angle relative to the optical axis of 22 degrees. This whole wavelength region can be amplified, while maintaining phase matching. Due to Snell's law, the noncollinearity angle outside the BBO needs to be 4.44 degrees (see fig. 3.11). The other angles shown in fig. 3.10 do not exhibit such a plateau and hence provide only a phase matched interaction for specific wavelength pairs instead of a wavelength region.

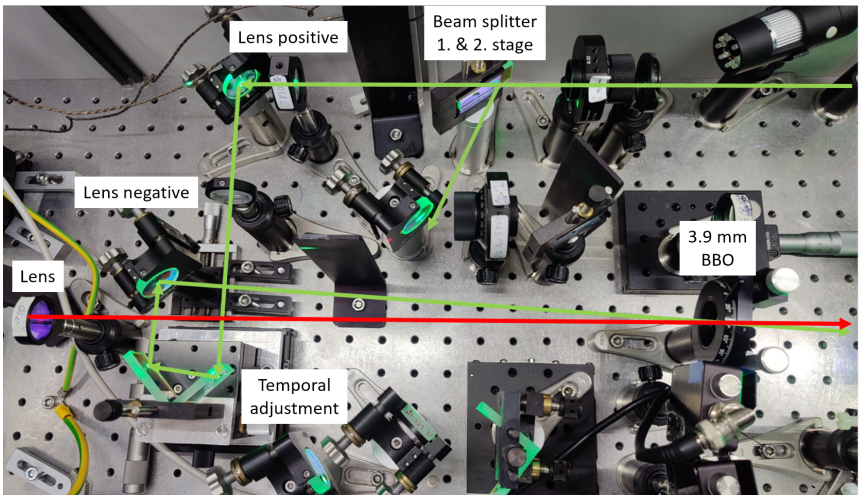

Figure 3.11: Photo of the first noncollinear amplification stage with schematic depiction of the beam propagation. The full pump beam (green) energy is first split via a beam splitter. Then the beam diameter is matched with the seed beam by two lenses. After that, the beam is temporally matched with the seed beam by a delay stage and enters the BBO crystal under an angle of 4.4 degrees with regard to the seed light (red). The BBO crystal is manufactured in such a way that the crystal surface perpendicular exhibits a 22 degree angle in regard to the optical axis of the crystal.

Next, it is important to choose the right intensity of the incoming laser beams. The general formula which connects the laser pulse energy E with its intensity $I(r,t)$ is:

$$E = \int_t \int_S I(r,t) dt dS \tag{3.1}$$

where the intensity of the pulse is integrated over the full space and time to calculate the pulse energy. Under the assumption of a Gaussian pulse shape in space and in time, this formula can be solved for $I(r,t)$ to read:

$$I(r,\tau) = \frac{2E}{\pi r^2 \tau} \tag{3.2}$$

In this formula, E represents the energy of the laser pulse, r is the radius of the beam profile from the maximum to $1/e^2$ and τ is the FWHM of the pulse duration. Following our splitstep calculations, the highest conversion efficiency is reached if the beams are comparable in terms of diameter for amplification factors lower than 100 or the seed beam is slightly bigger for higher amplification factors. This is due to the beam narrowing caused by a high amplification factor. In experiments we found, the conversion efficiency is best in the first stage with a seed beam, slightly bigger than the pump beam.
To select the right crystal dimensions, one needs to consider the following:
On the one hand, nonlinear crystals can support a certain crystal and thickness dependent spectral bandwidth due to phase mismatching, as explained in section 2.3.3. If a broader than supported spectral bandwidth is chosen, the sides of the spectrum are not amplified optimally and the final spectrum will be narrower. To avoid spectral losses, the crystal must be chosen thin enough, such that the participating pulses do not run out of temporal overlap throughout the crystal due to the phase mismatch.
On the other hand, in the amplification processes stated in this thesis (see sections 3.3.2, 3.3.4, 3.3.6 and 3.3.7) the goal is to convert as much energy from the pump pulse to the seed and idler pulses. This means we want to reach a certain energy of the signal beam relative to the pump energy in the process. The energy of the signal after amplification is given by replacing z with the crystal length l in the formula 2.21. Assuming, the diameter and pulse duration of the signal pulse only change marginally, we can rewrite the formula 2.21, as follows:

$$E_s = E_s(0)\cosh^2\left(\left(d_{\text{eff}}^2 I_p \frac{2\omega_s\omega_i}{\epsilon_0 c^3 n_p n_s n_i} - (\Delta k/2)^2\right) l\right) \tag{3.3}$$

where E_s is the signal pulse energy after amplification and $E_s(0)$ the signal pulse energy before amplification. If E_s shall be kept constant and the crystal length l shall be minimized, we can only increase the pump intensity I_p or the start energy $E_s(0)$, since the other parameters (explained in equation 2.21) are given by the process itself or the material. The start energy of the signal pulse is given by the history of the pulse before amplification and can only be changed by different generation of the seed beam. Increasing the intensity of the pump pulse is limited by the material properties of the crystal. Manufacturing companies of nonlinear crystals usually give a value for the damage threshold of their crystals, which should not be exceeded to prevent optical damage to the crystals. In that sense, to achieve optimal amplification in a nonlinear amplification stage the beam intensities need to be chosen to be close to, but still lower than the damage threshold of the crystal and then the necessary crystal length can be derived to reach the wanted signal pulse energy E_s.
Due to the noncollinear interaction in the first and third stage, the phase

mismatch for the wavelength range between 750 nm and 850 nm is very low, such that comparably long crystals can be used. In this stage, the seed pulses provided by the Ti-Sa oscillator are amplified within a 3.9 mm thick type I BBO crystal.

To verify our calculations for the optimal pump intensity, we conducted an

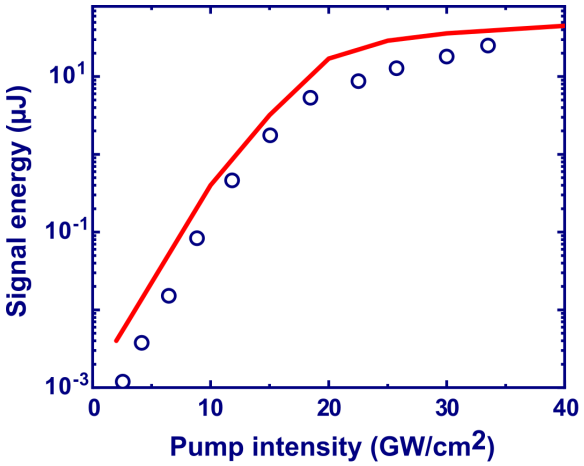

Figure 3.12: Logarithmic plot of the signal energy with regard to the pump intensity of the first noncollinear OPA stage. The red line shows the calculated efficiency with the split step program. The blue rings represent the measured signal energy. [72]

efficiency measurement by increasing the pump energy and measuring the signal energy (see fig. 3.12). We observe an exponential growth of the signal energy for pump intensities lower than 20 GW/cm^2 and sub-exponential growth afterwards. This means, that we depleted the pump pulse at the point of its highest intensity for 20 GW/cm^2.

Due to the exponential nature of the process, the amplification is stronger at points with higher intensity throughout the pulse. Therefore, the pump pulse is depleted earlier in the spatial center of the Gaussian pump profile and later at the sides of the pump profile. This means, that while the pump pulse is depleted in the center and will not amplify the signal beam anymore, the sides will still amplify the signal beam in the known exponential manner. Even worse, in the center the signal and idler beams will convert back and generate the pump wavelength, as displayed in figure 3.13.

However, in the far field, the rather extreme temporal and spatial structure will merge with the intensity distribution of the rest of the beam. Therefore, the measured spectrum and beam shape of such a pulse will be an average of all the contributing spectra shown below. Due to the competing conversion of the center and the sides of the beams, the measured efficiency curve still grows after 20 GW/cm^2, but lower than exponential with pump intensity. Amplification with this competing behavior between amplification and back

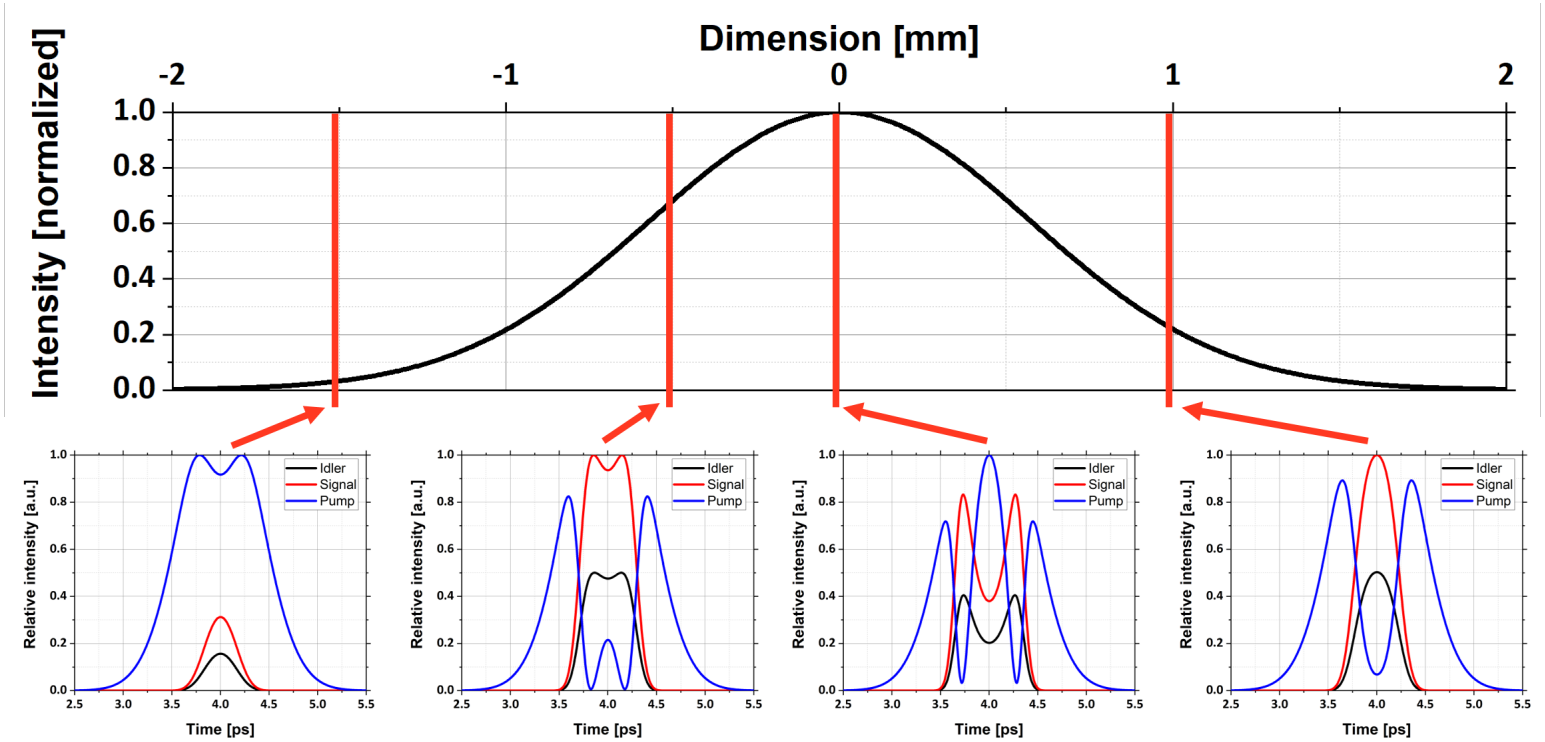

Figure 3.13: The top plot displays the spatial intensity distribution of a Gaussian beam. Since the depletion of the pump energy within a nonlinear amplification stage depends on the intensity at each point in time and space, the process is progressed further closer to the center of the beam. The lower subplots visualize the degree of depletion of the pump beam in an amplification stage in the time domain at different positions within the beam.

conversion is called the saturated regime. It can also have advantages to work in this regime: In the exponential amplification regime, any movement of the beams in space (pointing instability) or in time (temporal drift or jitter) significantly alters the resulting energy of the signal beam. Since the amplification is rather linear in the saturated regime, any turbulence in the process will reflect in much lower signal changes compared to the exponential regime.
The program we invented and used to calculate the amplification stages is a so called "splitstep" program [77] for Matlab, which divides the crystal length in several steps. At each step, the program first calculates the nonlinear interaction of the participating beams (signal, pump and idler) and then switches to the frequency domain via a fast Fourier transformation. In the frequency domain, the program calculates the additional linear phase of the material and nonlinear phase from self phase modulation of the beams. A specific spectrum from the participating beams can be imported and the development of the pulse intensities can be simulated.
This program helps significantly to understand the processes happening during an amplification stage. With the program, one can understand how deep into the saturation regime the process is driven and how distorted the laser pulses are in space, time and spectrum. Apart from that, we could derive what efficiency could be anticipated at which pump power and how thick the nonlinear crystal may maximally be chosen to avoid spectral losses due to accumulated temporal walk-off of the laser pulses and phase mismatching within the crystal.
For this stage, we used a pump intensity of 36 GW/cm^2 to reach deep into the saturated regime. At this pump intensity, our gain parameter (following definition from equ. 2.23) is about 20000 corresponding to a signal energy of 35 µJ.

	Pump	Seed
Wavelength [nm]	515.0	775
Bandwidth [nm] (FWHM)	0.4	288
Pulse energy [µJ]	260 ± 1	$(1.80 \pm 0.02) \cdot 10^{-3}$
Beam diameter [µm] ($1/e^2$)	1410 ± 50	1680 ± 50
Pulse duration [fs] (FWHM)	930 ± 10	3200 ± 100
Intensity [GW/cm^2]	36 ± 2	$(52 \pm 3) \cdot 10^{-6}$
Repetition rate [Hz]	100	$80 \cdot 10^6$

Table 3.2: Beam properties of pump and seed beams for the first OPA stage.

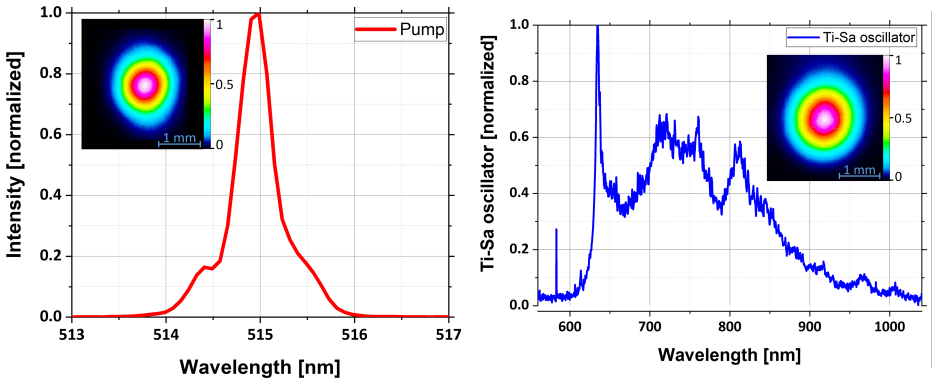

Figure 3.14: Measured spectra of the pump beam after the grating compressor (left) and the seed beam from the Ti-Sa oscillator (right). The insets are the measured beam profiles.

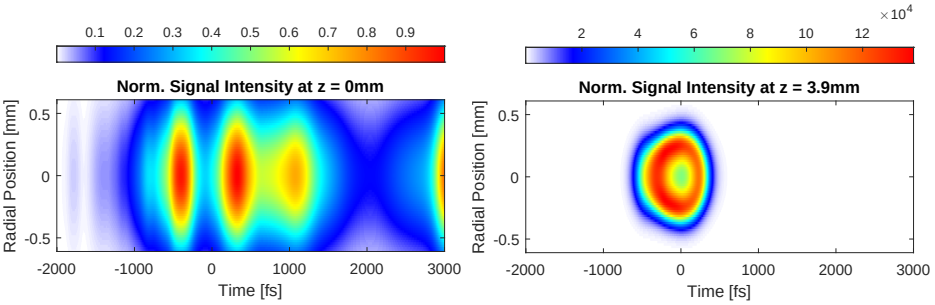

Figure 3.15: Comparison of spatial (vertical axis) and temporal (horizontal axis) distribution of the signal beam before amplification at the crystal position z = 0 mm (left) and after amplification at the crystal position z = 3.9 mm (right). The intensity of the right image is normalized to the original intensity of the beam before amplification.

Using our splitstep program, we can see the temporal and spatial distribution of the seed beam and the amplified signal beam (figure 3.15). In contrast to the intensity distribution of the camera image (inset of figure 3.14, right) of the beam, we see that the amplification into this strong saturation leads to a minimum in the very center of the spatial and temporal profile of the signal pulse (figure 3.15, right). Since a normal camera or beam profiler can not resolve the beam temporally, this minimum can only be seen and considered for further amplification stages in simulations.
It is very important to keep track of the amplified spectrum within the four amplification stages. However, the signal beam is spatially directly overlapping with the seed beam. The spectrometer used in this setup is averaging over several milliseconds. This means, the average power of the signal pulses and the seed pulses is measured. In the first stage, the seed beam from the

Ti-Sa oscillator has a repetition rate of 80 MHz, but the pump only amplifies 100 pulses per second. This means, that even if the seed pulses are amplified by a factor of 20000, the relative average power of the amplified pulses in regard to the seed light is outmatched by 1:53. Therefore, the spectrum of the amplified pulses can only be detected with great difficulty among the spectrum of the seed light.
To address this matter, we inserted a thin 60 µm BBO crystal to generate the second harmonic of the pulses. The crystal size and pulse intensity for the process is chosen such that only a small portion of the full energy of the beams is converted to the second harmonic. For low conversion rates, the second harmonic generation follows a quadratic growth with the fundamental pulse energy. Therefore, the pulse energy of the second harmonic light from the amplified pulses $E_{SHG}(\text{amp})$ divided by the pulse energy of the unamplified pulses $E_{SHG}(\text{unamp})$ corresponds to the gain factor of the first amplification stage squared:

$$\frac{E_{SHG}(\text{amp})}{E_{SHG}(\text{unamp})} = g^2 = 20000^2 = 4 * 10^8 \tag{3.4}$$

If we investigate the relative average power P_{SHG} between the second harmonic generated from the amplified and unamplified pulses, we find:

$$\Rightarrow \frac{P_{SHG}(\text{amp})}{P_{SHG}(\text{unamp})} = \frac{E_{SHG}(\text{amp}) f_{rep}(\text{amp})}{E_{SHG}(\text{unamp}) f_{rep}(\text{unamp})} = 500 \tag{3.5}$$

where f_{rep} is the repetition rate. Therefore, the relation of the second harmonic average power between the seed and the amplified light is 500:1. With that relative power, the spectra of the signal beams dominate in the spectrometer and can be seen in figure 3.16 as blue dots on the left plot.
It is not trivial to calculate back to the originating spectrum on the basis of the second harmonic spectrum. To tackle this problem, the spectrum of the simulated amplification is convoluted with itself to generate the second harmonic spectrum. This simulated spectrum can then be compare to the SHG spectrum of the measurement.

The spectrum shows the desired double peak structure and has a bandwidth of about 60 nm FWHM or about 30 THz in the frequency domain. From this spectrum, we can simulate the shortest possible pulse duration to be 26 fs FWHM. As mentioned in section 3.3.1, the double peak structure allows conserving most of the spectrum throughout the next stages. Therefore, it allows for the generation of a spectrum in the mid infrared which may be compressed to a pulse duration close to the calculated limit here.

3.3.3 Temporal stabilization system and wavelength selection

For all four amplification stages, the temporal overlap of the pump pulse with the seed pulse is absolutely critical. Due to the positive chirp of the

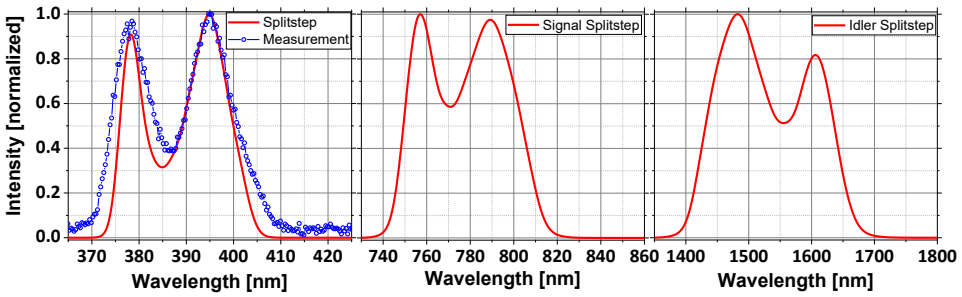

Figure 3.16: Measured (blue dots) and simulated (red line) second harmonic spectrum after the first NOPA stage (left). Spectrum generated with the self written Splitstep program of the fundamental signal beam (middle) and idler (right).

seed pulse, a spectrum with longer wavelength is amplified if the pump pulse is delayed with regard to the seed pulse. This also changes the spectral properties of the signal and the idler. In the term of less than an hour, experiments have shown, that the system can drift into a temporal mismatch such that the amplification at the desired wavelength vanishes entirely. To counteract this problem, we set up a temporal stabilizing unit following the example given by S. Hädrich et al. [78] and F. J. Furch et al. [79].
The temporal stabilization unit makes use of the horizontally dispersed idler beam of the noncollinear interaction, as mentioned in the theory section 2.3.4. Due to the noncollinearity of the interaction, the momentum conservation can only be fulfilled for a matching set of wavelengths, as displayed in figure 2.9. The longer the signal k vector k_s, the shorter must be the idler k vector k_i and the bigger will be the angle between signal and idler beam. This means, on the one hand, that the idler beam profile will be horizontally elongated (as seen in fig. 2.10) and will exhibit rising wavelengths from one side to the other. On the other hand, if the signal pulse as a whole is shifted in time, a different wavelength range will be amplified. This means that the idler beam as total will move, depending on the chirp of the seed, and the temporal displacement between seed and pump.
To correct for temporal shifts, we forward the idler beam to two photo diodes, which detect the horizontal edges of the beam (see fig. 3.17). We read out the diodes with a QDC (Charge-to-Digital Conversion) unit and evaluate their signal strength within a LabVIEW program. The beam and the diodes are placed such, that intensities impinging on the diodes are equal if the proper spectrum is amplified. The LabVIEW program controls an automated delay stage for the seed beam to compensate for temporal displacements. If the idler beam moves, due to temporal mismatch between the seed and the pump, the LabVIEW program evaluates the photo diode signals and uses a PID routine to calculate the necessary movements of the

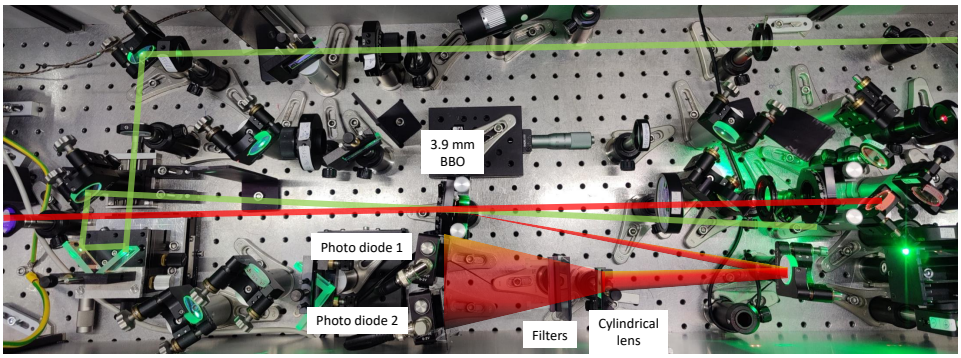

Figure 3.17: Foto of the setup with depicted pump, signal and idler beams. The idler beam is forwarded via a mirror to two photo diodes. To increase the horizontal dispersion, we inserted a negative cylindrical lens and attenuated the light with gray filters.

automated delay stage such that the seed pulse overlaps perfectly with the pump pulse again.

3.3.4 Second stage: Difference frequency generation, Changing wavelength to 1545 nm

Within the second amplification stage, the goal is to generate an idler beam with optimal parameters such that it can be used for the next stage instead of the signal beam. It is possible to use the idler after an noncollinear amplification stage, but it needs quite some effort to compensate for the horizontal dispersion and its spatial chirp. There are successful approaches to this problem. By manipulating the group velocity of the signal before the amplification, Huang et al. have proven to avoid the horizontal dispersion of the idler before generation [80]. Another approach is to use a grating and cylindrical mirrors to reshape the idler after generation, as demonstrated by K. Okamura et al. [81].
However, in our system, we chose to use a collinear amplification regime to avoid the horizontal dispersion of the idler. This means, that the phase matching cannot be optimized for a range of wavelengths but rather only for one specific wavelength. This implies that the longer the birefringent crystal is selected, the more bandwidth is lost during the amplification process. Consequently, the choice of the crystal length is a trade-off between converted wavelength bandwidth and generated idler pulse energy.
We chose the collinear approach, because firstly, it generates no additional problems like the compensation for the horizontally dispersed idler beam. Secondly, any temporal beam instabilities would otherwise generate an additional spatial movement in the noncollinear amplification regime, which is another source of unwanted beam pointing fluctuations. It is essential to

minimize any beam instabilities in such a complex system, because they are magnified in further stages and can disturb conclusive experimental data in the end. To be able to amplify the full spectrum of the seed light and

	Pump	Seed
Wavelength [nm]	515.0	780
Bandwidth [nm] (FWHM)	0.4	50
Pulse energy [µJ]	300 ± 2	30 ± 2
Beam diameter [µm] ($1/e^2$)	1200 ± 50	1400 ± 50
Pulse duration [fs] (FWHM)	930 ± 10	900 ± 100
Intensity [GW/cm^2]	57 ± 2	4.3 ± 0.9
Repetition rate [Hz]	100	100

Table 3.3: Beam properties of pump and seed beams for the first DFG stage.

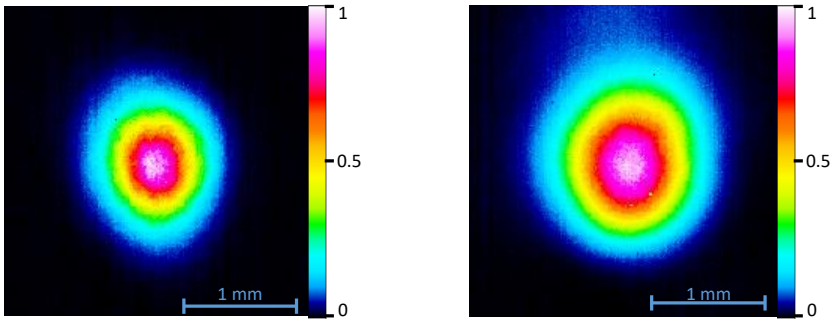

Figure 3.18: Beam profiles of pump (left) and seed (right) beams for the second stage.

thereby generate the broadest possible spectrum of the idler, we calculated that the thickness of a type I BBO crystal may not exceed 0.6 mm and needs to exhibit a 22.5° angle between signal and optical axis. To reach here also the more stable saturated regime and thereby have efficient conversion, we need comparably high pump intensities of 60 GW/cm^2 even with the maximum crystal thickness of 0.6 mm. Therefore, we chose to use the maximum thickness for this BBO crystal of 0.6 mm. For these parameters, we measured a pump efficiency of about 25 %. The amplified signal pulse energy is 80 µJ and the idler pulse energy is 25 µJ. The newly generated idler beam has a spectral bandwidth of about 178 nm (or 23 THz in frequency domain), which supports a transform limited pulse duration of 29 fs.
After the amplification, we isolate the idler from the signal and the pump via two dichroic mirrors (see fig. 3.20) and use a broad band lambda half plate to rotate the polarization of the idler for the next stage. The polarization of the idler is then horizontal and therefore, the noncollinearity angle of the third stage is also oriented horizontally.

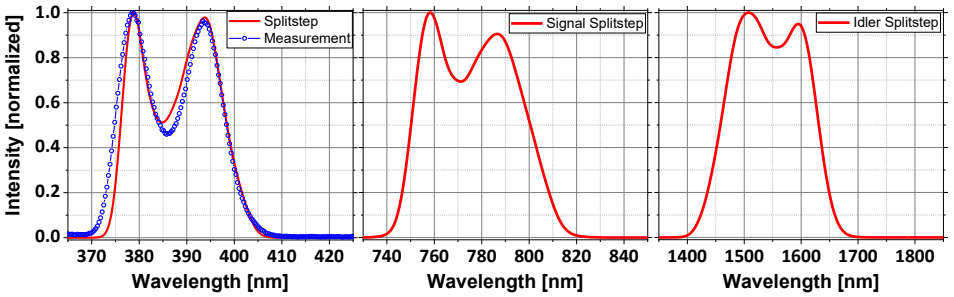

Figure 3.19: Measured (blue dots) and simulated (red line) second harmonic spectrum from the amplified signal light from the second stage (left). Corresponding spectrum generated with the self written Splitstep program of the fundamental signal beam (middle) and idler (right).

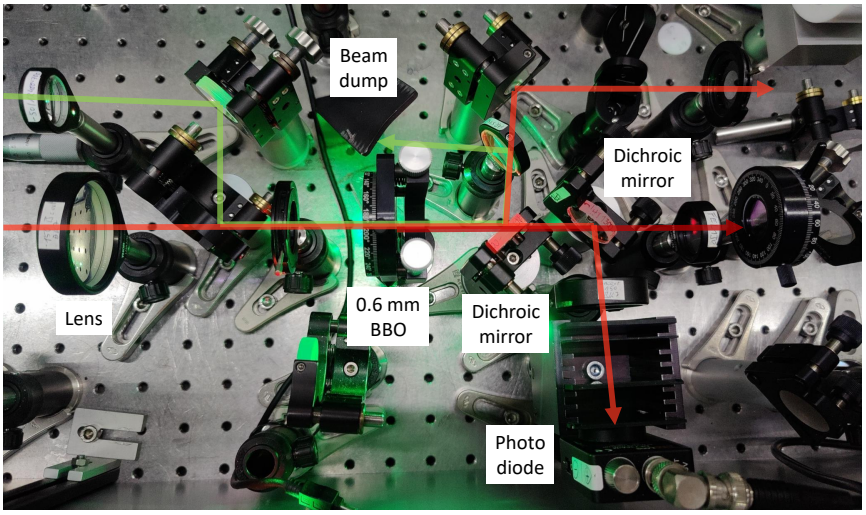

Figure 3.20: Foto of the setup with depicted pump, signal and idler beams. The idler beam is separated from the signal and pump beams with two dichroic mirrors. The reflection from the first mirror is forwarded to the spectrometer or the Ferrocene experiment (see section 4.1). The leak through the first mirror is reflected by a second mirror and is tracked for continuous stability measurement.

3.3.5 Third stage: Crystal discussion for best amplification of 1545 nm

In this stage the goal is to amplify the idler from the second stage (which will be called seed henceforward) in such a way that we have once again an optimal spectral, temporal and spatial shape to optimally generate the mid infrared light in the last stage. Therefore, the used nonlinear crystal must have a broad phase matching bandwidth for the interaction between our center wavelengths of the pump at 1030 nm, the seed at 1545 nm and the idler at 3090 nm. To minimize the crystal length, the d_{eff} should be as high as possible. Also, if the crystal shows any absorption at the participating wavelength bandwidths, the crystal will eventually heat up and break if not cooled constantly. The system currently works with a repetition rate of 100 Hz, so even with some absorption in the crystal, the deposited power dissipates quickly enough without harming the crystal. However, the final working repetition rate is supposed to be 20 kHz and with that the heat dissipation needs to be actively supported.

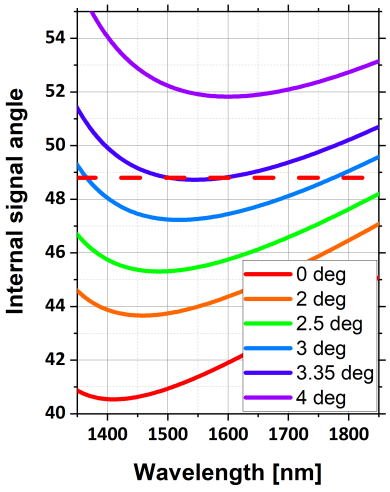

Figure 3.21: Each plot depicts the necessary phase matching angle of KTA for a corresponding wavelength in a noncollinear amplification scheme. The different plots result from different noncollinearity angles between seed and pump beam. They were calculated with SNLO [47] using a pump wavelength of 1030 nm.

We considered 4 different materials for this amplification stage: Potassium titanyle arsenate (KTA), potassium titanyl phosphate (KTP), Lithium iodate ($LiIO_3$) or Lithium niobate (LNB). We found KTA to be the best nonlinear optical crystal for this amplification stage. KTA has no absorption between 700 nm and 3500 nm and under noncollinear interaction angle of 3.35 degrees it shows a flat phase matching behavior in the vicinity of 1545 nm (see fig. 3.21). For this nonlinear process, it also has a comparably high d_{eff} of 2.45 pm/V. KTP is in principle the predecessor of KTA . Even in the noncollinear interaction scheme, the center of the flat phase matching band cannot be moved to 1545 nm (the center wavelength of our seed beam). Additionally, it has sharp absorption edges around 2800 nm and broadband absorption starting from 3000 nm onward [82]. LNB can be used in noncollinear interaction scheme to have a flat band at 1545 nm and shows a high d_{eff} of 4.18 pm/V for our nonlinear process. Unfortunately, it shows a broad absorption at 2870 nm due to OH^- absorption.
Also for $LiIO_3$, a noncollinearity angle can

be found to fulfill phase matching conditions for our interaction and is perfectly transparent for our pump, seed and idler beams. However, companies claim, that the crystal has a significantly lower damage threshold of 100 MW/cm^2 for TEM$_{00}$ mode with 1064 nm, 10 ns, 10 Hz. In comparison KTA has a damage threshold of 500 MW/cm^2 for the same laser specifications. Additionally, $LiIO_3$ also has a lower d_{eff} of 1.5 pm/V. Even though $LiIO_3$ has its drawbacks, in comparison to KTA , it shows a much lower group velocity mismatch under collinear interaction. This is the determining factor for minimizing spectral bandwidth loss if noncollinear amplification is not a option. Therefore, it is the best candidate for the second DFG stage, as described in section 3.3.7.

3.3.6 Third stage: Amplification of 1545 nm

In principle, the next DFG stage could already accomplish the goal to generate the mid infrared light with previously generated seed light. However, this would result in an amplification factor of about 100 and because of that we would lose spectral bandwidth due to gain narrowing. Additionally, we would be unable to use the pump beam efficiently because the spatial beam radius would shrink during the amplification process.

	Pump	Seed
Wavelength [nm]	1030.0	1545
Bandwidth [nm] (FWHM)	0.8	180
Pulse energy [µJ]	1900 ± 10	20 ± 1
Beam diameter [µm] (1/e^2)	4000 ± 100	4200 ± 100
Pulse duration [fs] (FWHM)	1100 ± 15	750 ± 50
Intensity [GW/cm^2]	25 ± 1	0.40 ± 0.05
Repetition rate [Hz]	100	100

Table 3.4: Beam properties of pump and seed beams for the third stage.

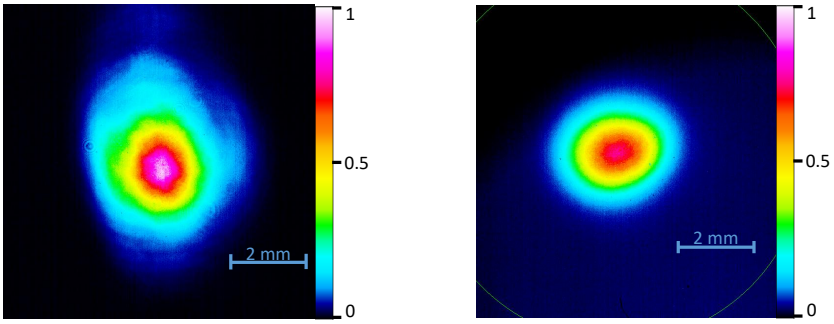

Figure 3.22: Beam profiles of pump (left) and seed (right) beams for the third stage.

To minimize the spectral losses and inefficiency of pump usage, this third stage in noncollinear geometry amplifies the full spectrum phase matched by a factor of 7.5. We use the type II noncollinear phase matching of a KTA crystal under an angle of 48.8 degrees. This signal angle is chosen slightly higher than the optimal phase matching angle as shown in figure 3.21, such that the center of the spectrum is slightly mismatched, but the wings are optimally phase matched. This situation helps to generate a spectrum, which has a flat top and minimum losses in spectral bandwidth (see fig. 3.23).
For the spectral analysis, we need to generate the second harmonic of the signal beam again. The reason is, that our spectrometer is silicon based. It can only detect light in the wavelength range from 200 to 1100 nm, but our signal light is centered at 1545 nm. Hence, we use the second harmonic of the light and calculate back to the originating wavelength range via the Splitstep program.

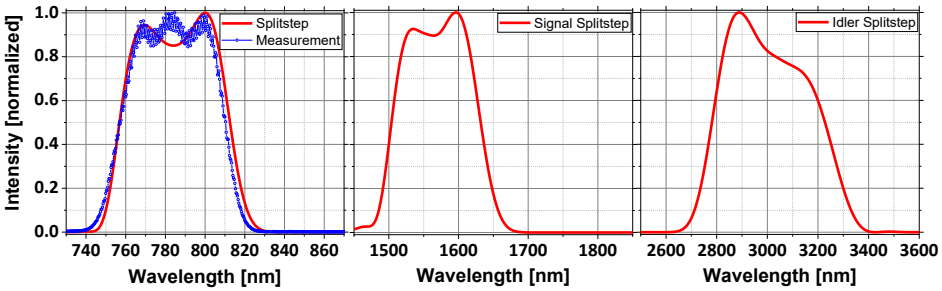

Figure 3.23: Measured (blue dots) and simulated (red line) second harmonic spectrum from the amplified signal light from the third stage (a). Corresponding spectrum generated with the self written Splitstep program of the fundamental signal beam (b) and idler (c).

The geometry is again chosen such, that the pump beam is slightly smaller, than the seed beam. Although the beam diameters are comparable, the pulse durations still differ, since the pump pulse is 1200 fs and the seed pulse is 750 fs long. The efficiency suffers, because the full energy of the pump pulse cannot be exploited. But since the temporal beam profile is flatter closer to the maximum of the pulse, a broader spectrum of the chirped seed pulse can be amplified with fewer losses due to temporal beam narrowing in comparison to temporally matching pulses. Therefore, we have an efficiency of about 13.5 % and gain a signal with an energy of 185 µJ and a specially dispersed idler beam with 82.5 µJ which is dumped.

3.3.7 Fourth stage: DFG, Changing wavelength to 3000 nm

The fourth and last amplification stage of the OPCPA is the most important one to generate a well suited idler beam for further experiments. In this stage, over 75 % of all the pump energy is used. For that, we use a 4 mm thick type I $LiIO_3$ crystal with $\theta = 19.4\,^\circ$. As discussed in section 3.3.5, $LiIO_3$ is the optimal crystal for this collinear stage, because it has acceptable high d_{eff} of 1.5 pm/V for the process, is perfectly transparent for participating wavelengths and exhibits much lower group velocity mismatch (GVM), also called temporal walk-off, for the interacting laser wavelengths than comparable crystals.
To put this into perspective, group velocity mismatch is defined as:

$$\text{GVM} = \frac{1}{v_{g1}} - \frac{1}{v_{g2}} \tag{3.6}$$

where $v_{g1/2}$ are the group velocities of wavelength 1 and 2. This means, for higher the group velocities mismatch of the participating wavelengths, the pulses temporally drift apart within the nonlinear crystal. The inverse group velocities divided by c in $LiIO_3$, LNB and KTA for this process are:

Wavelengths	$LiIO_3$	LNB	KTA
Pump (1030 nm)	1.870	2.252	1.826
Seed (1545 nm)	1.870	2.260	1.837
Idler (3090 nm)	1.875	2.283	1.818

Table 3.5: Inverse group velocities divided by c of pump, seed and idler pulses for the fourth amplification stage.

Using our Splitstep program, we found that due to the well matching group velocities, in the $LiIO_3$, the full spectrum of the seed beam may be converted into the mid infrared with theoretical efficiencies of up to 30 % for Gaussian beams. Due to the slightly higher mismatch in LNB and KTA, the pulses drift apart within the crystal and optimal efficiency can not be warranted. Also due to the drift apart, the generated mid infrared spectrum is narrower and deformed, depending on how long the crystal is chosen.
To reach the saturation regime with LNB and KTA, these crystals may be chosen shorter, because they have a higher d_{eff} of 4.04 pm/V and 2.05 pm/V, respectively, compared to 1.5 pm/V from $LiIO_3$. Therefore, the drift apart of the participating laser pulses is reduced, but still does not compensate the effect of the intrinsic group velocity mismatch. This means, that even though the $LiIO_3$ crystal must be chosen longer to reach saturation, the resulting spectra and efficiency of the process are preferable to the results with LNB or KTA.
Our experimental results agree comparably well with the simulation as

shown in figure 3.25 and in this stage we achieved an efficiency of 25 %. The signal pulses at a central wavelength of 1.545 µm contain 1.8 mJ pulse energy and the idler at a central wavelength of 3.0 µm of 0.8 mJ.

	Pump	Seed
Wavelength [nm]	1030	1545
Bandwidth [nm] (FWHM)	0.8	190
Pulse energy [µJ]	10500 ± 50	180 ± 10
Beam diameter [µm] ($1/e^2$)	8000 ± 200	9200 ± 200
Pulse duration [fs] (FWHM)	1100 ± 15	750 ± 50
Intensity [GW/cm^2]	35.0 ± 1.5	1.4 ± 0.2
Repetition rate [Hz]	100	100

Table 3.6: Beam properties of pump and seed beams for the fourth stage.

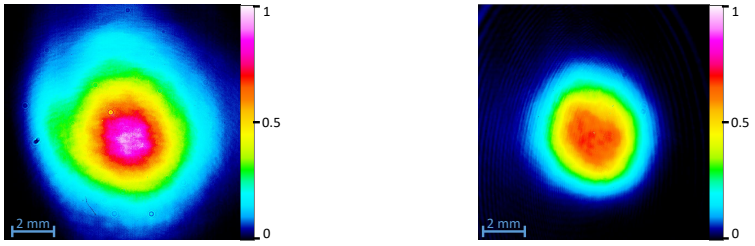

Figure 3.24: Beam profiles of pump (left) and seed (right) beams for the fourth stage.

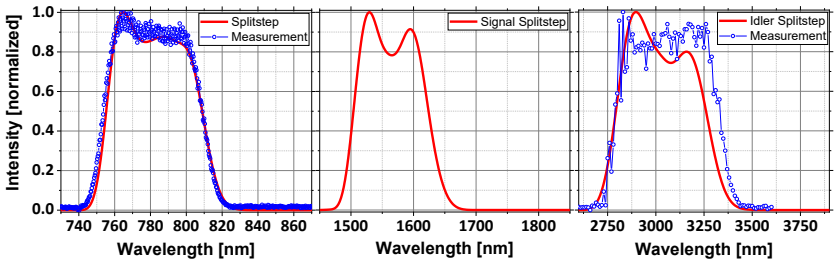

Figure 3.25: Measured (blue dots) and simulated (red line) second harmonic spectrum from the amplified signal light from the fourth stage (left). Corresponding spectrum generated with the self written Splitstep program of the fundamental signal beam (middle). Measured (blue dots) and simulated (red line) spectrum of the idler (right).

3.4 Group velocity dispersion management

Now, we come to the last part of the OPCPA which is the compression part of the amplified pulses. The system creates pulses at three different wavelengths, which are: Red pulses centered at 0.77 µm (coupled out after the second amplification stage), near infrared (NIR) pulses centered at 1.56 µm and mid infrared (MIR) pulses centered at 3.0 µm. The later are both coupled out after the fourth and last stage. The red pulses are amplified pulses from the Ti-Sa oscillator and overlap with the unamplified pulses. Their chirp is mainly determined by the amount of materials in their beam paths. To get a rough estimate of the amount of dispersion, we need to compensate, we calculated the effect in second and third order dispersion (SOD & TOD) of all the individual optics within the beam path up to the second amplification stage and summed them up. Then, for the NIR pulses, we inverted the sign of SOD and proceeded as for the red light before. For the MIR pulses, the sign of the SOD is inverted once again. Since, we want to have compressed pulses at the experiment, all optical elements up to the experiment were considered as well. The results of the calculation are given in table 3.7.

	0.77 µm (red)	1.56 µm (NIR)	3.0 µm (MIR)
Second order dispersion [fs^2]	5600	-5400	5100
Third order dispersion [fs^3]	4200	10000	11600

Table 3.7: Calculated amount of SOD & TOD after amplification of the different outgoing pulses.

To analyze the pulse duration of ultrashort pulses, we either use an autocorrelation function (ACF) or frequency resolved optical gating (FROG) measurement. FROG is in principle an ACF which is spectrally resolved at each individual relative temporal position between the two pulses. The details of the two measurement techniques are well described in the book of Rick Trebino, "Frequency resolved optical gating" [83], that is why I only want to discuss the general ideas. Since ultrashort laser pulses are so short, one can only measure the duration of the pulses with the pulses themselves. An ACF measurement setup splits the pulse into two, using a beam splitter. One branch is delayed against the other one and both are focused onto a nonlinear crystal (see fig. 3.26).
For a second order autocorrelator, one is interested in the second harmonic light, which is generated from the combination of one photon of each beam. In a third order autocorrelator, one of the beams contributes with two photons. The signal value of the interaction is given by the temporal integral

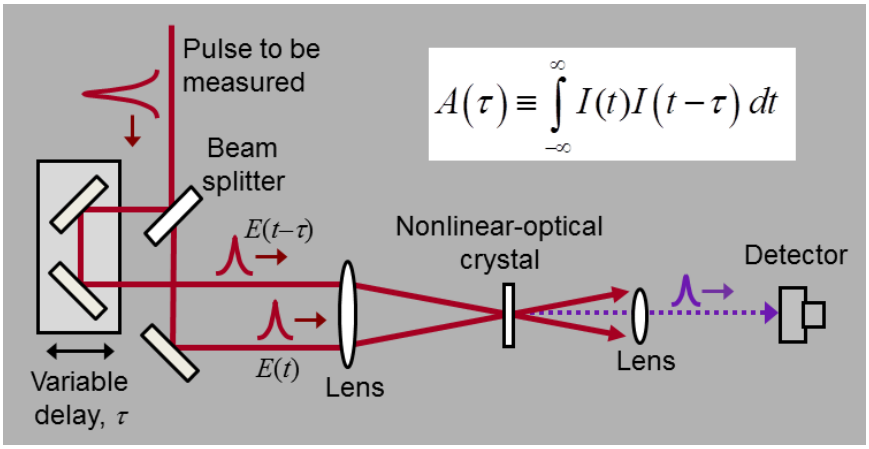

Figure 3.26: Schematic of an intensity autocorrelation function. The pulse to be measured is split into two with a beam splitter. One branch is delayed against the other one and both are focused on a nonlinear crystal. The interaction of the light is then imaged onto a detector. (Schematic taken from [84])

over the second harmonic intensity as follows:

$$A^{(2)}(\tau) = \int_{-\infty}^{\infty} I_1(t)I_2(t-\tau)dt \tag{3.7}$$

I_1 and I_2 represent the intensity and τ is the temporal delay between the incoming beams. For a third order autocorrelator, the signal value can be calculated as follows:

$$A^{(3)}(\tau) = \int_{-\infty}^{\infty} I_1(t)^2 I_2(t-\tau)dt \tag{3.8}$$

The second order autocorrelation function is symmetric. Hence, one cannot distinguish whether pulse irregularities are proceeding or lacking behind the main peak. This is not the case in a third order autocorrelator, which uses two photons of one branch and only one of the other. This clarity about the temporal order also gives more detailed information about the sign and the order of the dispersion.
If we investigate the interaction in the crystal more in detail, we realize the wavefronts of the pulses are tilted against each other. Therefore, an interaction can only take place, when both beams overlap spatially and temporally as displayed in figure 3.27. In that sense, the interaction area in the nonlinear crystal depends on the pulse durations of the incoming pulses. To quantify this situation, the delay between the two beams as a function of the traverse coordinate, x, can be formulated as:

$$\tau(x) = 2(x/c)\sin(\theta/2) \approx x\theta/c \tag{3.9}$$

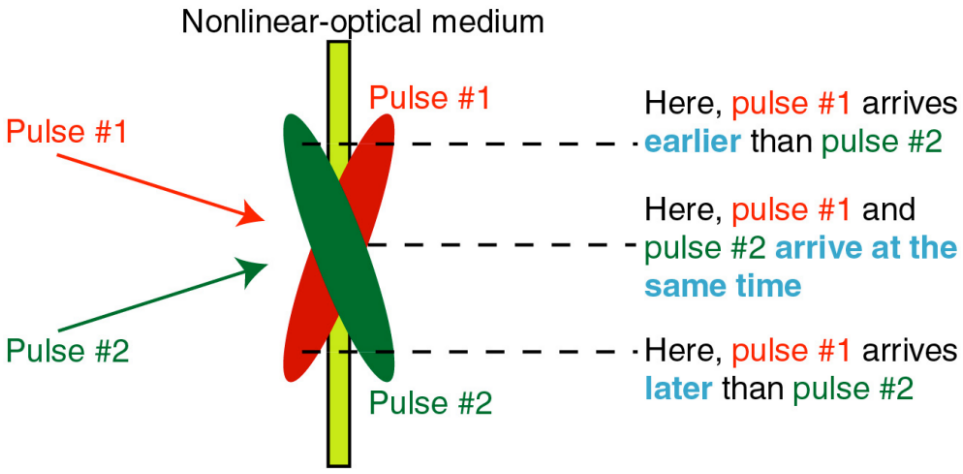

Figure 3.27: Depiction of the wavefront tilt and overlap of two ultrashort pulses in a crossed interaction. Due to the pulse duration and the angle between the two pulses, an interaction of the pulses only happens where both pulses are at the same place and time. In this schematic, this is the case where the red and green ellipses overlap. (Schematic taken from [83])

Where c is the speed of light and θ is the angle between the incoming beams. For this equation, we assumed, the nonlinear crystal to be infinitely thin. The second part of the equation uses the small angle approximation for $\theta/2$. Following this logic, we only need to image the nonlinear crystal onto a camera and we can interpret the intensity distribution on the camera image as a so-called single shot autocorrelation function. This situation has the advantage, that the whole ACF is visible on the camera without moving the delay stage of one of the pulses. For short pulses, as in this setup, the single shot autocorrelator is a good tool, because the limit of this technique is given by the beam size on the crystal, the pulse duration of the pulse and by the camera.
For example: One can calculate with relation 3.9, that for a beam size in the crystal of 5 mm and an angle between the beams θ of 15 degrees, the maximal measurable pulse duration to be 4.4 ps. The resolution of the ACF is given by the pixel size and the magnification of the beam onto the camera chip. Assuming a 10 mm chip, to image the full beam, the magnification should not exceed 2x. With a pixel size of 5 µm, we have 2000 pixels and thereby a temporal resolution of 4.4 fs. With this single shot ACF , the resolution can easily be improved to less than a femtosecond by increasing the magnification.
On the other hand, for a multi shot ACF , as described in the beginning of this section, the upper limit of the measurable pulse duration is only determined by the length of the delay stage. So this may lie well in the

nanosecond regime. The lower limit for this measurement is determined by the influence of the wavefront tilt (fig. 3.27). In that case, it is advantageous to have a small beam size and angle between the pulses.
For example: If we assume a beam size of 200 µm and an angle θ of 1 degree, the lower limit for temporal resolution is 12 fs.
Another problem to keep in mind is the wavelength and the responsivity of the detector. For single shot ACF , we use a silicone CCD camera with a detection range from about 0.35 µm to 1.1 µm. Therefore, we can only use second order ACF for the red pulses centered at 0.77 µm, second and third order ACF for the NIR pulses centered at 1.56 µm and only third order ACF for the MIR pulses centered at 3.0 µm.

3.4.1 Pulse characterization by single shot third order frequency-resolved optical gating

Even though the ACF already gives information about pulse duration, to compress the pulses we need to quantify how much SOD and TOD our pulses exhibit. For this reason, we did FROG measurements. Instead of imaging the crystal surface onto a camera to generate a single shot ACF , we imaged the crystal onto the slit of a spectrometer and thereby were able to spectrally resolve the ACF . By doing so, one has enough information about the pulse, to determine the original spectrum of the beam before interaction in the crystal together with the amount of dispersion of the pulse. The details about deconvoluting the resulting FROG image can be found in the book of Rick Trebino, "Frequency resolved optical gating" [83]. To evaluate our FROG images, we used the Matlab implementation from Prof. Trebino's group, found on their website [85]. A photo of our self-built FROG setup is shown in figure 3.28.
We calibrated the temporal axis, by slightly delaying one pulse against the other. This shifts the interaction area on the crystal vertically. This can be understood by imagining pulling pulse #1 back along its arrow in figure 3.27. Because of this movement, the two ellipses of pulse #1 and #2 will intersect in the crystal plane further up in the figure and therefore also the interaction moves up. Due to the imaging onto the spectrometer, also the FROG image in the spectrometer moves up correspondingly. With that, we can quantify the amount of pixels shifted by the added distance to one pulse. This method delivers a time calibration of the system via:

$$t/\text{pixel} = \frac{2}{c} \cdot \frac{\Delta d}{\Delta\text{pixel}} \tag{3.10}$$

Δd is the distance moved with the delay stage and Δpixel is the amount of pixels, the FROG image moved after shifting the delay stage.
We calibrated the spectral axis independently by illuminating the slit of the

spectrometer with a gas lamp filled with Cesium I (Cs I). The spectral lines of Cs I can be found at NIST Atomic Spectra Database [86].

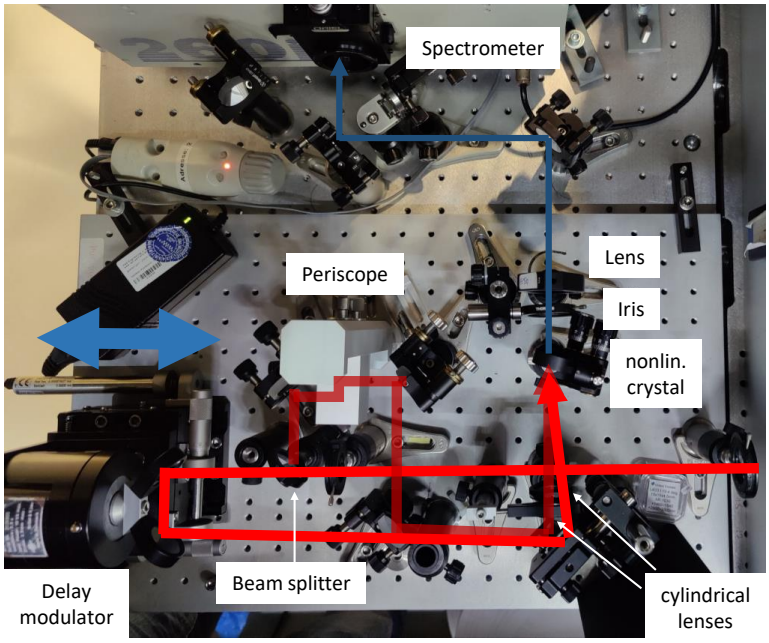

Figure 3.28: Photo of the FROG setup. The incoming light is first split into two branches with a beam splitter. The reflected light is lowered with a periscope and horizontally focused with a cylindrical lens into a thin nonlinear crystal. The transmitted beam is first reflected from a delay modulator to find temporal overlap between both branches. Then it is also horizontally focused with a cylindrical lens into the nonlinear crystal. Two photons of the stronger branch interact with one photon of the weaker branch to generate third harmonic light as cross correlation. Due to the vertical displacement of all three outgoing beams, an iris is used to filter out the seed beams. The newly generated light is then imaged with a lens onto the entrance slit of the spectrometer. The spectrometer then resolves the vertical ACF spectrally in the horizontal axis.

3.4.2 Prism compressor for 770 nm

For the red light centered at 770 nm, we calculated to have about 5600 fs^2 in SOD and about 4200 fs^3 in TOD due to the influence of materials in the beam path. This is of course a rough estimation of the actual dispersion of the pulse, but it already gives an idea of suitable compression techniques as discussed in section 2.5. The positive SOD and TOD of the pulses cannot be compressed, by material because it will just increase the SOD and TOD . Grating compressors could compress the SOD , but would also just increase

the TOD. Therefore, we have the option to use a prism compressor or chirped mirrors. We decided to use a prism compressor, because this solution offers us flexibility in the amount of dispersion to be compensated. The prism compressor is set up to be operated in Brewster configuration. This means, the incidence angle θ_0 into the prism and the outgoing angle from the prisms are the same.

$$\theta_0 = \theta_B = \arctan(n(\lambda)) \tag{3.11}$$

$$\alpha = 2 \arcsin\left(\frac{\sin(\theta_B)}{n(\lambda)}\right) \tag{3.12}$$

α is the apex angle of the prism, $n(\lambda)$ the wavelength dependent refractive index and θ_0, θ_B the incidence and Brewster angle respectively. We used SF10 prisms, because SF10 has a refractive index of 1.71 at 770 nm. Therefore, the Brewster angle and the apex angle are both about 60 degrees, meaning the prisms are equilateral. This makes them cheep, and they can easier be manufactured with high quality.

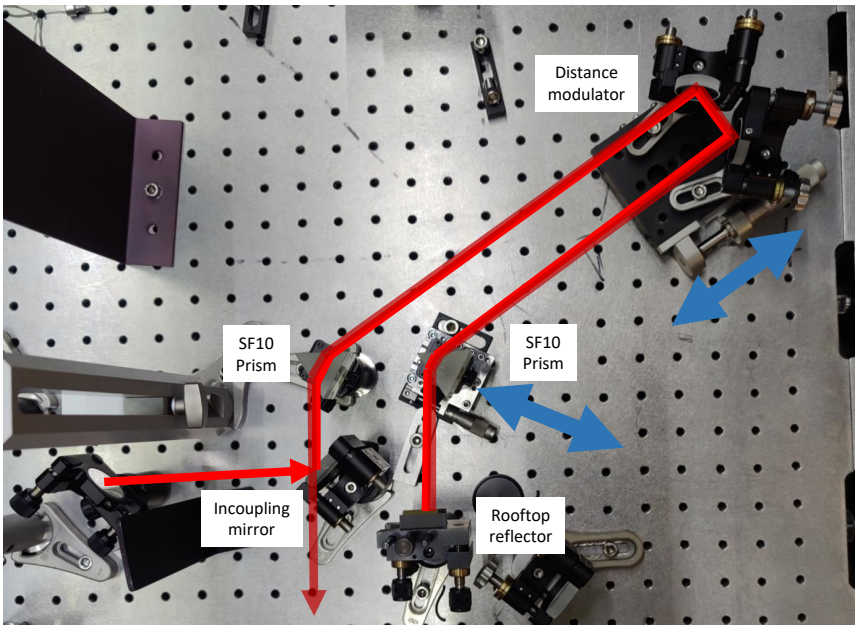

Figure 3.29: Photo of the prism compressor used to compress the 770 nm beams. After in-coupling the light, it is diffracted in a SF10 prism, then reflected back by a horizontal rooftop construction, diffracted by a second SF10 prism and sent back slightly higher by a vertical rooftop construction. The horizontal rooftop construction and the second SF10 prism are sitting on linear delay stages to easily modulate the distance between the prisms and the amount of SF10 material used.

After the compressor, we forwarded the light towards a second order, single shot FROG and were able to optimize the pulse duration with a live FROG image. The optimal results were measured with a distance between the prisms of 50 cm and a distance from the incidence point of the beam to the peak of the prism of about 5 mm for both prisms. Following the online calculator [65], this corresponds to a SOD of -6500 and TOD of -21900. In the measured FROG trace (fig. 3.30), we see a residual side peak at -60 fs in the pulse duration plot, which can be traced back to an overcompensation of the TOD . The prism compressor is still able to compress the pulse from about 350 fs to 49 fs compared to an optimal pulse duration of 34 fs based on the spectral bandwidth. The outgoing pulse energy after compression is 40 µJ.

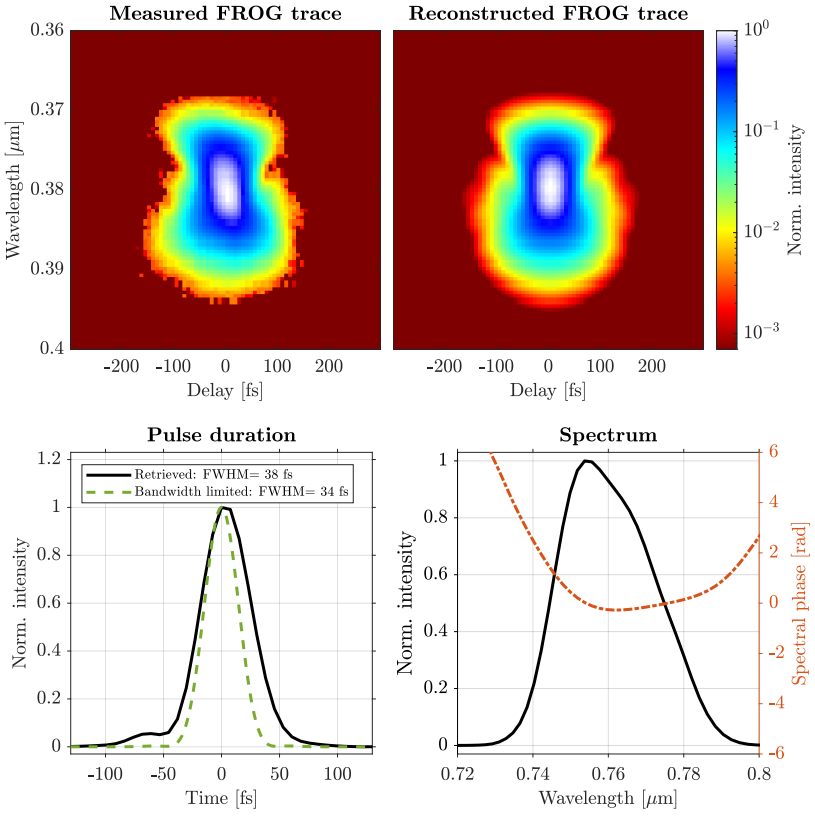

Figure 3.30: Top: Measured (left) and retrieved (right) second order FROG trace for the red pulses centered around 770 nm. The better these two traces agree, the more accurate is the retrieved phase, pulse duration and spectrum. Bottom left: Retrieved pulse duration (solid black) in comparison to an optimally compressed pulse (green dashed). Bottom right: Retrieved spectrum of the pulse (solid black) with the spectral phase (orange dashed).

3.4.3 Compression with material for 3000 nm

As discussed in section 3.3.1, the compression of the MIR pulses centered at 3000 nm can be done deploying material dispersion only. Due to exchanging the signal wavelength twice in two DFG stages, the SOD and TOD of the MIR light is positive in the end. Hence, we can mitigate the SOD with sapphire glass. We found optimal results when using 6 mm of sapphire glass under Brewster angle, such that the losses due to reflection are minimized.

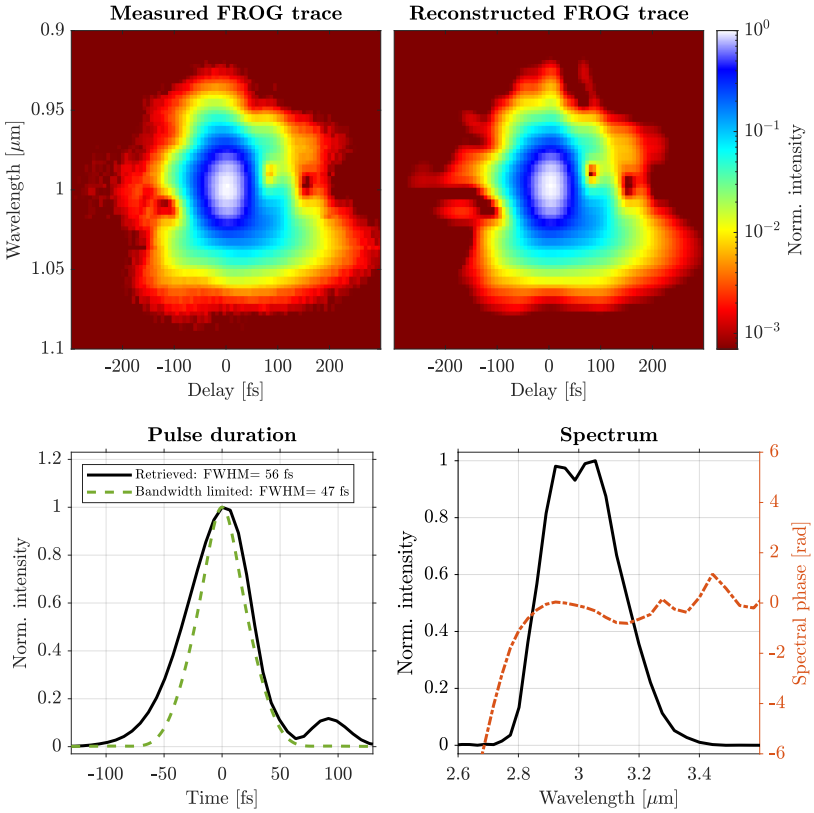

Figure 3.31: Top: Measured (left) and retrieved (right) third order FROG trace for the MIR pulses centered around 3 µm. The better these two traces agree, the more accurate is the retrieved phase, pulse duration and spectrum. Bottom left: Retrieved pulse duration (solid black) in comparison to an optimally compressed pulse (green dashed). Bottom right: Retrieved spectrum of the pulse (solid black) with the spectral phase (orange dashed).

With the glass, we were able to compress the pulse to a pulse duration of 63 fs (see fig. 3.31). The glass also increases the TOD of the pulse so much, that this results in an afterpulse at about +80 fs. This can be seen in the pulse duration plot in figure 3.31. Even though the afterpulse turns out to

be as high as 10 % of the main peak, it contains less than 0.4 % of the overall energy of the pulse. Due to the use of the sapphire plates in Brewster angle, the losses are negligible, yielding pulses centered at 3 µm with pulse energies of 0.8 mJ and pulse durations of 63 fs.

3.5 Conclusion

In this chapter, I discussed the OPCPA setup in detail, and now I will conclude on the strengths and weaknesses of the concept and its realization. With this setup we generated three ultrashort output laser pulses in the visible, near infrared and mid infrared range with the following parameters:

	VIS	NIR	MIR
Wavelength [nm]	775	1545	3060
Bandwidth [nm] (FWHM)	50	190	500
Pulse energy [µJ]	40 ± 2	1800 ± 60	800 ± 30
Pulse duration [fs] (FWHM)	49 ± 5	∼700 (uncomp.)	63 ± 5

Table 3.8: Laser parameters of VIS , NIR and MIR laser pulses.

Within the OPCPA , the laser pulses from the Ti-Sa oscillator are stretched with bulk BK7 glass, amplified, the wavelength changed twice and then compressed again. We chose to stretch the pulses from the Ti-Sa oscillator with glass, because due to the two wavelength changes, it was possible to compress the laser pulses centered in the mid infrared region by using only bulk material again. This has the advantage, that the bulk material can be used in Brewster angle configuration and thereby the losses of compression are below 1 %. Compared to this, the VIS laser pulses were compressed with a SF10 prism compressor, with losses of 1/3 of the pulse energy.
After stretching, the laser pulses of the Ti-Sa oscillator had a pulse energy of 1.8 nJ and a repetition rate of 80 MHz. For the DFG stage, we needed to have a strong seed pulse to convert the good beam qualities of the Ti-Sa oscillator pulses to the idler beam. Therefore, we first amplified a selected spectrum of the octave spanning spectrum of the Ti-Sa oscillator in a noncollinear OPA stage. With the amplified seed light from the first NOPA stage, we were able to generate a Gaussian shaped beam with only 10 % losses in bandwidth in the NIR for later stages.
As discussed in section 3.3.6, to preserve the most of the spectral components, we amplified now the NIR pulse to be a strong seed pulse for the last DFG stage. The last DFG stage used over 75 % of the full pump energy, which we generated in the pump channel. In this stage, the goal was to generate as much as possible of the MIR light but also to preserve the most of the spectral bandwidth. In this stage, we used a type I $LiIO_3$ crystal,

which offered the best phase matching of available nonlinear crystals for the process in a collinear setting. With this crystal, we converted 70 % of the bandwidth into the mid infrared and generate pulses with 800 µJ of pulse energy.
After the amplification, we measured the pulses with a third order, single shot FROG for 3 µm. The camera of our FROG setup was on silicon basis, such that it could only measure the third harmonic and not the second harmonic. With this setup, we have proven the duration of the compressed MIR laser pulses to be 63 ± 5 fs long.
For the VIS laser pulses, to be suitable for later experiments, we needed to implement a SF10 prism compressor. The resulting pulse duration was then measured by a second order, single shot FROG . It was measured to be 49 ± 5 fs.
In the course of generating 0.8 mJ pulses centered at 3 µm wavelength, we also generated 1.8 mJ of pulse energy centered at 1.5 µm wavelength. These pulses were analyzed, compressed and used for high harmonic generation. In this thesis, I did not discuss this branch, because my colleague Oscar Naranjo was mainly responsible for these achievements.
To compare to other current laser systems, our output in the MIR range delivers pulses with comparable parameters in terms of pulse energy and pulse duration, as can be seen in table 3.9.

Reference	Central wavelength (µm)	Pulse energy (mJ)	Pulse duration (fs)	Repetition rate (kHz)
This work	3.06	0.8	63	0.100
[19]	2.5	0.126	14.4	100
[38]	3	2.7	125	10
[20]	3.2	0.152	38	100
[37]	3.4	0.3	56.5	1
[35]	3.8	0.045	79	100
[41]	5.5	0.4	99	1
[40]	7	220	16000	0.1

Table 3.9: Comparison of this system's MIR output to other current laser systems delivering high energy, mid infrared, ultrashort pulses.

The average laser power of our system with a repetition rate of 100 Hz is however still lower than several other systems. Our system is also meant to work with a higher repetition rate of up to 20 kHz and thereby be on par with others. But to handle the system easier while setting up, the repetition rate was reduced to 100 Hz and will be increased, when no further changes for the system are planned.
The biggest difference of current OPCPA systems designed to generate high intensity MIR pulses, are the used nonlinear crystals. For MIR generation,

there is a number of nonlinear crystals which are transparent for these wavelengths, can have phase matching for the down conversion process and yield a good conversion efficiency. Most prominent crystals are KTA (Potassium Titanyl Arsenate), LNB (Lithium Niobate) and PPLN (Periodically-Poled Lithium Niobate). As discussed in chapter 3.3.6 and 3.3.7, we chose in our fourth stage $LiIO_3$ to generate the mid infrared pulses from the near infrared pulses. The reason is, that $LiIO_3$ exhibits lower GVM for the participating wavelengths compared to LNB or KTA and can thereby support the conversion of a broader spectral bandwidth, but exhibits a lower damage threshold than other crystals. Due to the lower damage threshold of $LiIO_3$ we had to decrease the intensity of our laser pulses by increasing the beam sizes of our signal and pump beams. Therefore, we needed to increase also the crystal length to reach the saturated regime in the amplification process. However, due to the low GVM, still the full spectral bandwidth could be converted, which made $LiIO_3$ the optimal crystal for our purpose.
In [38], the authors report a powerful system, delivering MIR laser pulses with pulse energies of 2.7 mJ, pulse duration of 125 fs and a repetition rate of 10 kHz. They achieved this good values by shaping the pump beam to a flat-top profile and then being able to convert about 13.3% of the pump beam into the mid infrared idler beam in a collinear DFG stage with KTA.

Chapter 4

Electronic and vibrational dynamics in Ferrocene self-assembled monolayers at solid-liquid interfaces

Electron transfer across solid/liquid (electrolyte) interfaces underlies much of the chemistry necessary for a sustainable global energy economy. Despite this evident importance, the elementary steps accompanying such electron transfer are not well understood on a microscopic level. Part of the challenge in gaining understanding is the enormous range of timescales the problem encompasses: elementary processes from femtoseconds to seconds are all important. Even with reducing the number of contributing variables by choosing metallic solids, in which the charge transfer dynamics are much faster than most of the processes in solution phase, the elementary processes that control electron transfer remain a highly non-trivial problem. In these systems, the net electron transfer rate k changes with the interaction strength Δ between the metal and the electrolyte. This dependence can be divided into three distinct regions: non-adiabatic, adiabatic and catalysis (see figure 4.1). Following W. Schmickler [87], for small (non-adiabatic) and large (catalysis) interactions, the electron transfer rate is proportional to Δ, but for an intermediate section, the transfer rate does not increase with rising interaction strength (adiabatic).
Butler and Volmer first delivered a phenomenological explanation for the change in electronic transition rates in the 1930s [88]. The existing theory was extended by R. A. Marcus in 1985 by explaining the outer sphere electron transfer reactions between two chemical species [89]. This explanation involved the reorientation of surrounding solvent dipoles to overcome the reaction energy. For this theory, R. A. Marcus received a Nobel Prize in Chemistry in 1992.

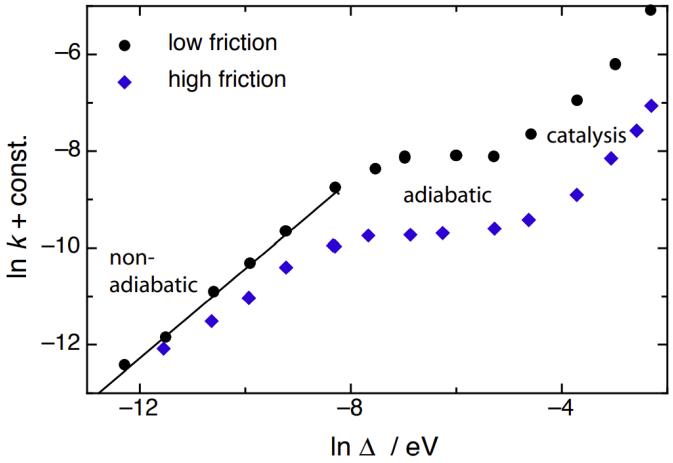

Figure 4.1: Simulated dependence of the electron transfer rate constant k on the interaction strength Δ. The plot can be divided in three regions: non-adiabatic, adiabatic and catalysis. The black dots and blue diamonds correspond to low and high solvent friction, respectively. The solvent friction is determined by the typical time that the solvent takes to reorient. The black line shows the prediction from 1st order perturbation theory (Figure is taken from [87]).

However, Marcus's theory makes the assumption that configurational change in the electrolyte is sufficiently rapid relative to electron transfer. This assumption is limiting in many situations, especially in metal/liquid electrolyte interfaces, which are very important because virtually all electron transfer reactions belong to this kind. To get an intuition of what might occur, existing work on inorganic/organic heterostructures like in photovoltaics may be taken as comparable systems. In these, charge transfer becomes mode specific, such that the excitation of vibrational modes increases the produced photocurrents. To investigate the mode specificity of the photocurrent, we designed an experiment in which a vibrational excitation at an electrode/electrolyte interface is generated at a well defined time and a photocurrent is generated with a second laser pulse before this excitation thermalizes.
Usually, vibrational lifetimes in aqueous solutions are in the order of femto- to tens of picoseconds, such that an all optical ultrafast experiment is needed. However, an experiment to investigate the charge transfer by only optical excitation in operando conditions is a challenging condition since any free electrons are absorbed in the liquid.
In this chapter, I want to present a new method to investigate the mode-specificity of the photocurrent generated at an electrode/electrolyte interface, show first results and interpretations of our experimental findings. For

this effort, we worked jointly with the work group of Kramer Campen from our university, namely Zhipeng Huang, Yujin Tong and Kramer Campen. They created the samples, helped with the measurements and developed an interpretation of the measured data.

4.1 Experimental method

To be able to investigate the photocurrent interface sensitive, we use a self assembled monolayer (SAM) of Ferrocene undecanethiol[1] on top of a gold substrate. Ferrocene systems are characterized by their extreme stability, reversible single electron transfer redox chemistry and its ability of rapid interfacial charge transfer. The gold with the Ferrocene structure on top is submerged in a solution of 0.5 mol/l K_2SO_4/D_2O. This solution is under constant flow to transport any heat generated in the process away from the interaction site and to replenish the electrolytes on site. In this solution, not only Ferrocene as also its ion Ferrocenium$^+$ (Fc^+) are apparent. The latter is able to accept an electron from the gold. Also, following Schmickler [87], each individual Fc or Fc^+ molecule has an energy state at a specific energy. But due to the dipole orientation of the surrounding water molecules, this energy state is energetically higher or lower. Therefore, the energy state of Fc and Fc^+ is broadened (see fig. 4.2) and we call it henceforth the possible energy states. We use an initial mid infrared femtosecond pump pulse to excite vibrational modes in the Ferrocene head group and use a second pump in the visible or ultraviolet to generate a non-equilibrium electronic state at the electrode/electrolyte interface. This non-equilibrium then thermalizes by pulling electrons from the gold substrate. The freed electrons from the gold then reduce the Ferrocenium$^+$ to Ferrocene. In our experimental cell, the substrate is divided into three electrodes: The reference (RE), counter (CE) and work electrode (WE) as depicted in figure 4.3 on the right.

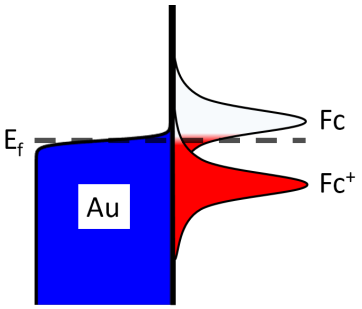

Figure 4.2: Energy distribution of gold with FcC11 on top in K_2SO_4/D_2O solution.

The laser pulses are only applied to the work electrode. Therefore, when electrons are pulled from the gold substrate, we can measure a voltage change by a comparably slow potentiostat between the WE and the RE in the course of seconds. Due to the second ultrashort pump pulse with defined time difference to the first pulse, the measured voltage change is modified if there is an influence between the processes generated by the two pulses. Therefore,

[1] Abbreviation for Ferrocene: Fc, for head group only and FcC11: For Ferrocene with 11 piece CH chain (undecanethiol)

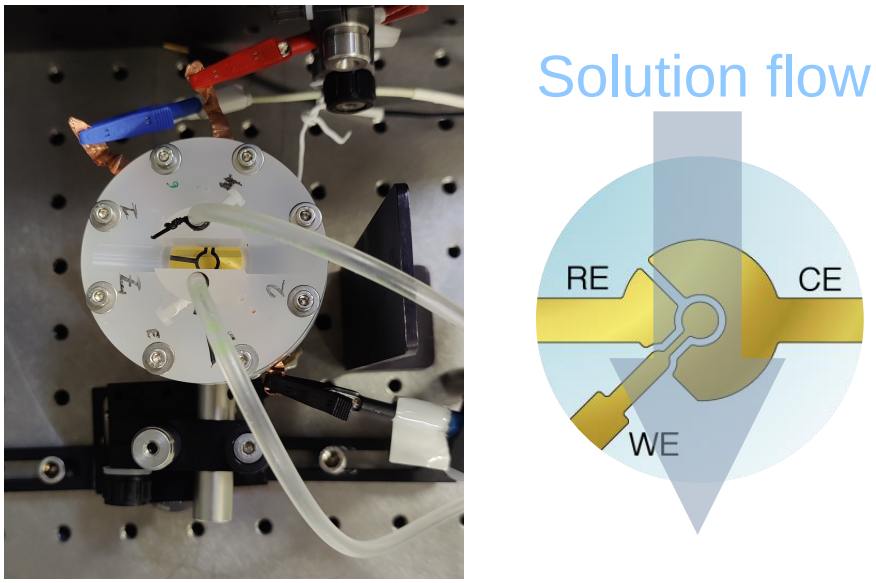

Figure 4.3: Photo (Left) and schematic (right) of the used chemical cell for electrostatic experiments. RE, CE and WE are the reference electrode, counter electrode and working electrode respectively. The gold electrodes were submerged in 0.5 mol/L K_2SO_4 in D_2O solution with constant flow through.

the slow voltage signal gives us an ultrafast information about the processes at hand. We call this experiment a double pump/probe experiment, because we pump the system with two laser pulses and probe it by measuring the voltage change with the potentiostat. Our colleges in the Faculty of Chemistry in Essen (Tim Lämmerzahl and Nelli Kremer) analyzed the Ferrocene with sum frequency spectroscopy and identified a spectrally clearly separated aromatic CH stretch absorption at 3220 nm in comparison to the aliphatic stretches at 3430 nm and 3496 nm. In the OPCPA described in the previous chapter, we generate MIR laser pulses with a spectrum, which is mostly exciting the aromatic CH stretch of the Ferrocene head group (see figure 4.4). In that way, we exclusively investigate the contribution of the aromatic CH stretch of the Ferrocene ring to the photocurrent.

4.1.1 Laser system

For the described double pump experiments of Ferrocene SAM on liquid/metal interfaces, the setup described in the previous chapter needs just a few additions. A schematic of the full setup for the Ferrocene experiments is displayed in figure 4.5. In the first and second amplification stages of the system, the seed light from the Ti-Sa-oscillator centered at 775 nm is amplified to 80 µJ which is used as visible (referred to as VIS) pump light

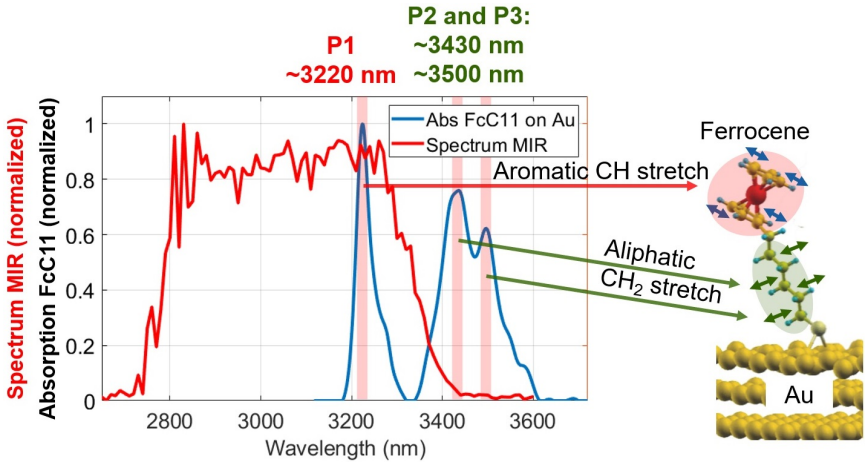

Figure 4.4: Spectrum of the MIR laser pulses (red) and absorption spectrum of Ferrocene terminated alkane thiol monolayers (blue). The absorption peaks were measured by vibrational sum frequency spectroscopy. Due to the interface sensitive measurement technique, the peaks correspond only to the Ferrocene SAM in solution. Individual absorption peaks P1, P2 and P3 are referenced to their origin in the molecule structure schematic to the right.

source. For the measurements with an ultraviolet pump, the VIS laser was doubled within a BBO crystal to 387 nm (referred to as UV), then chopped and afterwards sent to a delay stage. For experiments with the VIS laser, the BBO crystal was taken out. The UV and the MIR light were then focused and sent to the sample under 45 and 65 degree grazing angles, respectively. The parameters of the lasers are listed in table 4.1. The fluence was calculated considering grazing incidence, the losses from optics on the path to the experiments and the pulse compression.

	UV	VIS	MIR
Wavelength [nm]	387	775	3060
Photon energy [meV]	3204	1602	452
Bandwidth [nm] (FWHM)	1	50	500
Bandwidth [meV] (FWHM)	8	100	70
Pulse energy [μJ]	10 ± 1	19 ± 1	140 ± 6
Beam diameter [μm] ($1/e^2$)	340 ± 20	480 ± 20	770 ± 40
Pulse duration [fs] (FWHM)	320 ± 50	110 ± 10	100 ± 10
Fluence [mJ/cm^2]	16 ± 3	15 ± 2	25 ± 3

Table 4.1: Laser parameters of UV , VIS and MIR laser pulses.

With the UV laser pulses, the goal is to free electrons from the gold and

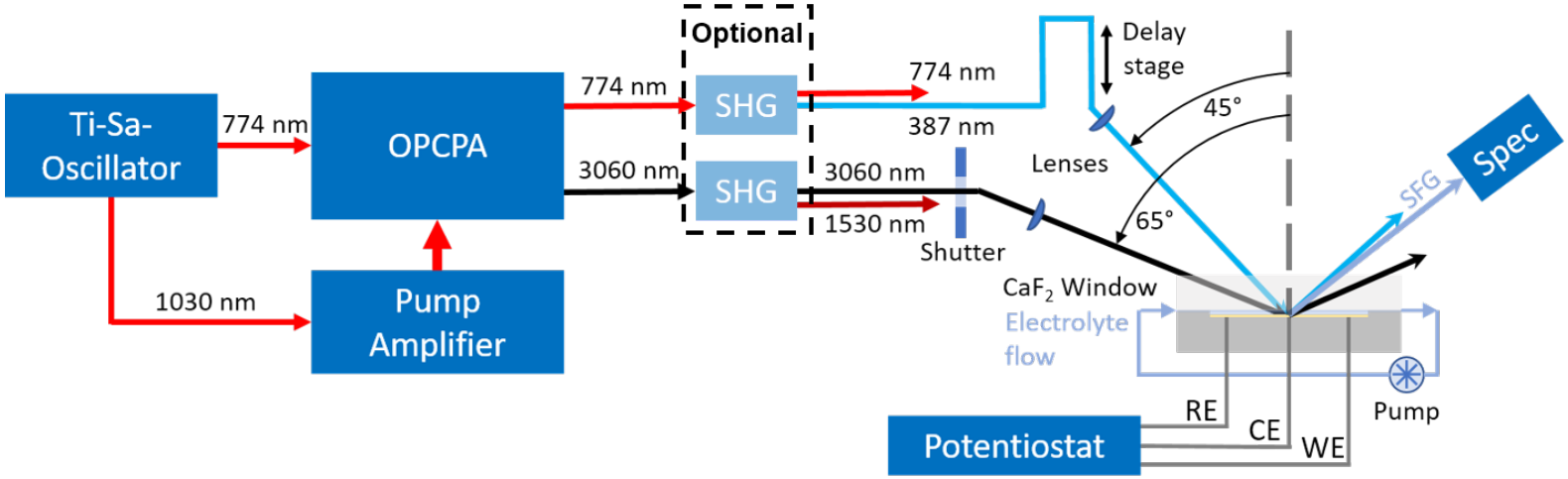

Figure 4.5: Schematic of the setup for electrostatic, double pump measurements. The laser system consisting of a Ti-Sa-Oscillator, OPCPA and pump Amplifier is explained in detail in the chapter before. SHG stands for a BBO crystal, which generates the second harmonic of the 774 nm (VIS) light. The laser beams with central wavelengths of 3060 nm (MIR) and 387 nm (UV) are focused with lenses onto the chemical cell at grazing incidence of 65° and 45° respectively. The preparation of the chemical cell is explained in section 4.1.2. To find time zero and measure a cross correlation between the VIS /UV and MIR , the sum frequency generation was analyzed with a spectrometer (Spec).

reduce the Fc^+ to Fc. Therefore, the only condition for the UV light is to be below the plasma edge of gold at 516 nm, which is the case for our spectrum (see fig. 4.6 left). We assume a two photon absorption process for the VIS laser pulses, which then finally yields the same effect as the UV light.

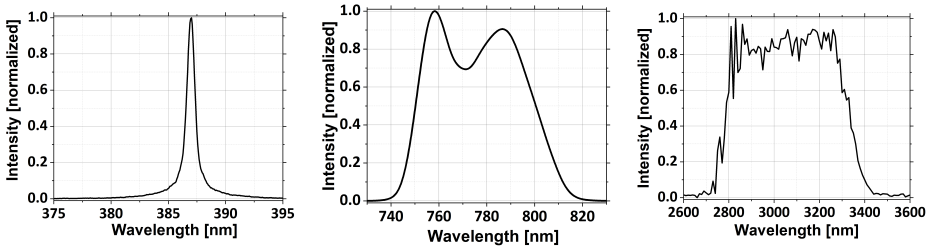

Figure 4.6: Spectrum of UV pulses, measured after second harmonic generation of VIS pulses (left). Calculated spectrum of the VIS laser pulses after the second amplification stage (middle). Measured MIR laser spectrum after generation at the fourth OPCPA stage (right).

4.1.2 Preparation of FcC11 self assembled monolayer on gold electrodes

The sample was prepared by our collaboration partners Zhipeng Huang, Yujin Tong and R. Kramer Campen.
The sample consists of a self assembled monolayer (SAM) of FcC11 on gold electrodes in an electrochemical cell filled with 0.5 mol/l K_2SO_4/D_2O solution. The thickness of the electrolyte is around 50 µm. The gold electrodes (5 nm Cr/200 nm Au) are prepared by electron beam deposition on top of a quartz plate. They were consecutively cleaned in an ultrasonic bath with acetone, Isopropanol, methanol and ultrapure water for 10 minutes each. In an additional step, they were cleaned with UV Ozone for 20 minutes, followed by rinsing with methanol and dried with Argon gas. The cleaned electrodes were immersed in a 2 mmol/l FcC11 methanol solution for two days. The FcC11 molecules then assemble themselves on the gold electrodes.

4.1.3 Data acquisition with the potentiostat

The procedure of the experiments as well as the chemical cell are used in a comparable way as described in the supportive information of [90]. In our setup, the two beams (either UV or VIS and MIR) are focused on the same spot on the center island of the sample, the working electrode (WE). The sample is used in open current voltage (OCV) condition, in which no voltage is applied. The voltage change was measured between the WE and the RE.

The potentiostat can only measure the change in voltage with a resolution of seconds, while we want to achieve femtosecond time resolution. For this purpose, we use a specific temporal order at which the lasers are shut or open. We let one of the two beams irradiate the sample uninterrupted until a stable state is reached. Then, the shutter for the second beam is opened. The second laser has the same repetition rate as the first, and each pulse is placed at a specific relative time Δt to the first pulse. After a certain amount of irradiation with the second pulse (in our experiments, we use 60 seconds), the shutter is closed, and the sample is only irradiated with the first laser for another 60 seconds. Then this loop is repeated for different temporal delay positions of the two laser pulses.
A voltage change ΔV is generated during the time the second laser beam is opened. This voltage change is the signal we investigate in this experiment. It depends on the temporal relation between both laser pulses. If the voltage changes more or less compared to the case in which both pulses have high temporal delay against each other (we consider them uncoupled), we can derive an influence between the processes generated by the two pulses.
For high relative temporal delay (in our case, $\Delta t = 150$ ps was chosen), we considered the observed voltage change as independently generated from the two pulses, and we took it as reference signal or uncoupled signal. In this time frame, positive times mean MIR pulses come first.
Each cycle of opening-closing-opening the shutter for the second laser pulse attributes one data point at a relative time delay between the pulses. In principle, the maximal voltage change after opening and before closing the shutter for the second laser inhibits the information about the magnitude and the entanglement of the processes driven by the laser pulses. But only the maximal voltage change is too unstable for evaluation. Therefore, we used the standard deviation of all the measurement points of a cycle to determine the magnitude of the signal (see fig. 4.7 left). It was calculated in the following way:

$$S_n = \sqrt{\frac{\sum_{t_{open(n)}}^{t_{open(n+1)}} (V_t - \bar{V})}{\#meas - 1}} \tag{4.1}$$

In this equation, S_n is the signal value for the relative time delay n, $t_{open}(n)$ is the time at which the shutter was opened for the relative time delay n, V_t is the voltage measured at real time t, $\bar{V}$ is the average value of all voltages measured in the cycle and $\#meas$ is the amount of voltage measurements in the cycle.

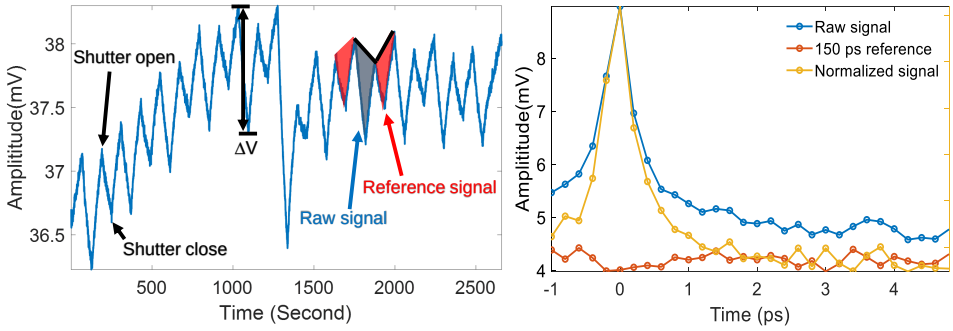

Figure 4.7: (left) Voltage measurement with opening and closing the shutter for the second pump pulse with different relative times. (right) Extracted experimental data in terms of amplitude change against relative time positions between the two laser pulses.

We also take one reference measurement after each measurement. This consists of a measurement in which the two laser pulses have high relative temporal delay (in our case: $\Delta t = 150$ ps) such that their generated signal is uncoupled from the other pulse. This is done to insure each measurement point is independent of the previous one. The reference signal should always show the same value if the measurements are independent. Only then the measurement can be considered stable enough for evaluation. The raw signal was divided by the reference signal to generate a normalized signal (see figure 4.7 right).
In general, this type of measurement is very sensitive to any environmental changes. But with this approach any unwanted voltage changes due to any single photon effects or long term environmental changes can be distinguished from the two photon effect.

4.1.4 Cross correlation measurement

As shown in figure 4.5, we have also the option to investigate the sum or difference frequency signal, generated by the two interacting pulses at the sample surface. Since SFG and DFG can only happen, when both beams are temporally and spatially overlapping, we were able to investigate the pulse duration and spectra of the interacting pulses. Due to the geometry with different grazing incidences of the laser pulses, the newly generated, weak SFG light, was spatially separated and could be guided individually to the amplified spectrometer (SpectraPro HRS-300 with the camera PI-MAX 4 from Princeton Instruments). By detuning the delay time and investigation of the generated SFG spectrum of the two pulses, we generate a cross correlation signal of the two pulses. The cross correlation signal $A(\tau)$ is

dependent on the pulse duration of the two pulses as follows:

$$A(\tau) = \int_{-\infty}^{\infty} I(t)I(t-\tau)dt \tag{4.2}$$

$I(t)$ is the intensity of the laser pulse at the time t. Therefore, an estimation for the pulse duration and a possible pulse chirp can be drawn. For the VIS laser, the DFG signal centered at 610 nm was investigated and for UV the SFG signal centered at 415 nm.

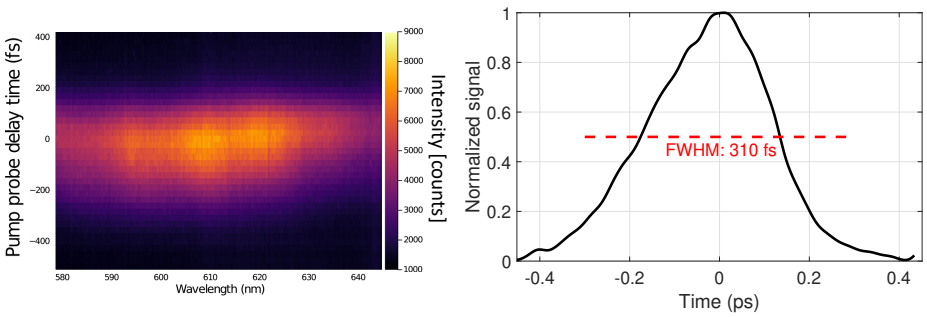

Figure 4.8: Left: Spectrally resolved cross correlation measurement off the sample between VIS and MIR . Right: Spectral integration and normalization to maximal intensity of the left image to yield the cross correlation of the two pulses. It shows a FWHM of 310 fs. It is also done to determine the temporal overlap between the VIS and MIR pulses.

We investigated the pulse durations of the pulses VIS and MIR already by FROG measurements described in section 3.4.2 and 3.4.3. We found the pulse duration of the VIS to be 49 fs and the MIR to be 63 fs. The DFG signal should show a comparable duration. However, since, the pulses need to travel through several additional optical elements to reach the sample, the pulses are expected to be longer at the sample itself. From the measurement shown in figure 4.8, we find the pulses were stretched on the way to the sample and generate a cross correlation signal with a FWHM of 310 fs.

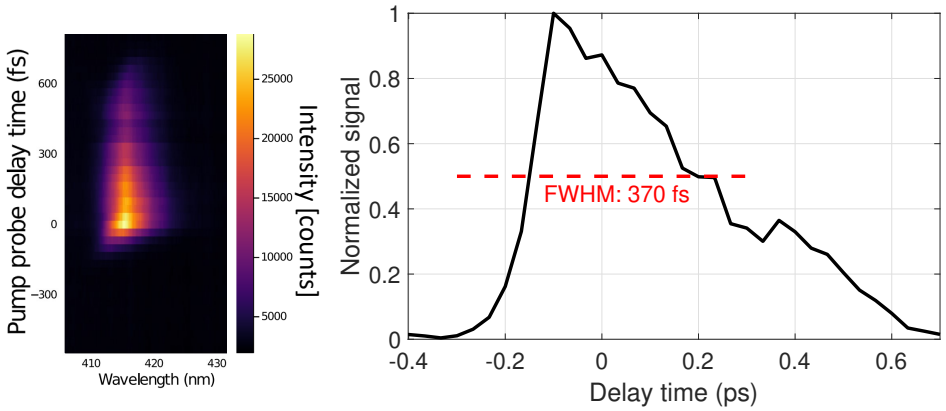

Figure 4.9: Left: Spectrally resolved cross correlation measurement off the sample between UV and MIR. Right: Spectral integration and normalization to maximal intensity of the left image to yield the cross correlation of the two pulses. It shows a FWHM of 370 fs. It is also done to determine the temporal overlap between the VIS and MIR pulses.

For the UV laser, we used a 3 mm thick BBO crystal for second harmonic generation. In principle, the BBO crystal is comparatively thick and a stable phase relation between the fundamental and the second harmonic light cannot be maintained within the whole crystal. This means that throughout the crystal, the VIS pulse will continuously produce UV light, but since the two wavelengths travel through the crystal at slightly different speeds, the generated UV pulse will be elongated. This can be seen in the left figure 4.9 for positive times. Here, the intensity of the DFG is maximal at time zero and reduces in intensity as time passes. However, this was a trade-off between pulse energy and pulse duration. With this thick BBO crystal, we were able to convert about 30 % of the VIS light into the UV and the cross correlation between UV and MIR is only marginally longer with 370 fs in comparison to the cross correlation between VIS and MIR.

4.2 Experimental findings

In this section, I present the experimental results and show additional supportive measurements to clarify the origin and dependence of the photoinduced voltage change. Within these additional measurements, we investigated the contribution to the signal of varying electrolyte flow and laser intensity.

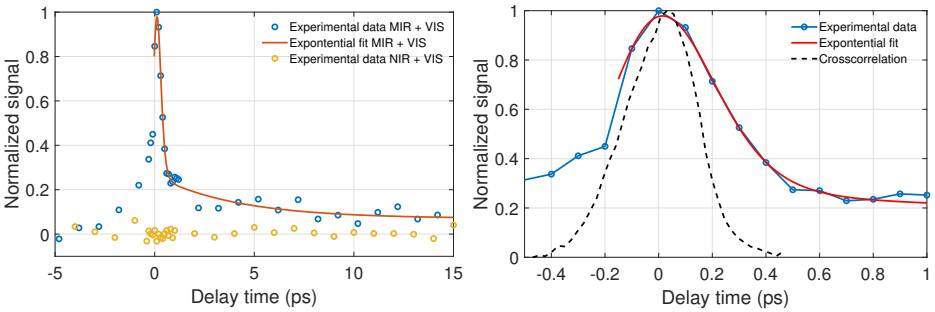

Figure 4.10: (left) Double pump measurements with VIS + MIR pump and VIS + near-IR. Blue and yellow rings indicate the normalized signal of MIR + VIS and near-IR and VIS, respectively, The red line is a double exponential fit. Positive delays correspond to MIR or near-IR pulses coming first. (right) Zoom in at time zero and comparison to the cross correlation of the two pulses, measured with their SFG signal, see figure 4.8.

4.2.1 Double pump measurements of Ferrocene self-assembled monolayers using a potentiostat

In this first measurement displayed in figure 4.10, we fit the data for positive times (MIR before VIS) with two exponential functions corresponding to two decay processes. They are multiplied with an error function to account for the sudden start of the driving of the processes by a Gaussian pulse in time. The fit is calculated with the formula:

$$I(t) = \left(\frac{1+A_1}{2}\mathrm{erf}\left(\frac{t-\sigma^2/\tau_1}{\sqrt{2}\sigma}\right)\right)\exp\left(-\frac{t}{\tau_1}+\frac{\sigma^2}{2\tau_1^2}\right)+... \tag{4.3}$$

$$+\left(\frac{1+A_2}{2}\mathrm{erf}\left(\frac{t-\sigma^2/\tau_2}{\sqrt{2}\sigma}\right)\right)\exp\left(-\frac{t}{\tau_2}+\frac{\sigma^2}{2\tau_2^2}\right) \tag{4.4}$$

In this formula, $A_{1/2}$ are the fitting parameter for the amplitude of the signals, erf is the error function, t is the time in picoseconds, σ is defined as $\sigma = \mathrm{FWHM}\cdot\left(2\sqrt{2\ln(2)}\right)^{-1} \approx 0.42\cdot\mathrm{FWHM}$ with FWHM being the full width at half maximum of the cross correlation between the laser pulses, $\tau_{1/2}$ are the life times of the processes. If we look closer at time zero (figure 4.10 (right)) the signal becomes comparable to the cross correlation signal from the DFG measurement. Fitting the curve with two exponential functions yields one long decay time of about $\tau_1 = 4 \pm 3$ ps and a short decay time of about $\tau_2 = 120 \pm 30$ fs.

We also generate the second harmonic of the MIR laser pulses, which I call in the figure the near-IR laser pulses. This light is not in resonance with any vibrational features of the Ferrocene head group. And in fact, with this light, we do not see any ultrashort life times, neither in the experimental results shown in figure 4.10 nor in figure 4.11. We took this measurement to

verify, that the processes in the experiments with MIR and UV or VIS laser pulses stem from the MIR laser pulses exciting the Ferrocene head group.

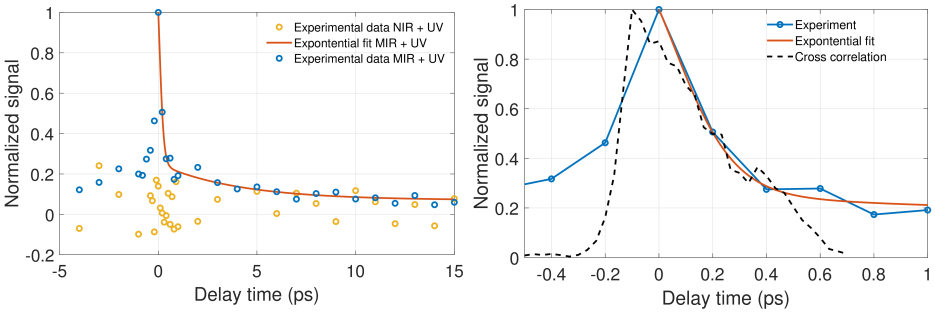

Figure 4.11: (left) Double pump measurements with UV + MIR pump and UV + near-IR. Blue and yellow rings indicate the normalized signal of MIR + UV and near-IR and UV, respectively, at individual delay times. The red line is a double exponential fit. Positive delays correspond to MIR or near-IR pulses coming first. (right) Zoom in at time zero and comparison to the cross correlation of the two pulses, measured with their SFG signal, see figure 4.9.

In the case of interaction with UV and MIR, we find the long decay time to be 4.0 ± 1.5 ps and the short decay time to be 120 ± 100 fs. The large error margins for the short decay time of the VIS + MIR measurement and the UV + MIR arise due to the comparable cross correlation signal, which is of the same order as the effect.

4.2.2 Flow rate dependence measurement

As mentioned in section 4.1.3, we are measuring very small voltage changes in open circuit voltage condition. This means, that small environmental changes (like rising room temperature or any air turbulences) may influence the measured voltage. Due to the reference measurement after each data point, any slow influences to the system can be eliminated. To investigate whether the laser pulses themselves heat the sample in the course of the measurement, we changed the flow rate of the electrolyte. Dependent on the flow rate, any deposited heat should be carried away faster or slower. If heat is deposited and whether it has some effect on the ultrashort processes is investigated in this chapter.
In the measurement seen in figure 4.12 we varied the flow rate of the solution by changing the rounds per minute (rpm) of the solution pump from 7.5 rpm to 15 rpm. In this experiment, we only saw a change in the magnitude of the signal, but not in decay times of the processes. Therefore, we concluded, that even if heat is deposited, it is either too little such that the processes are not affected or the ultrafast processes are independent of the local heat generated

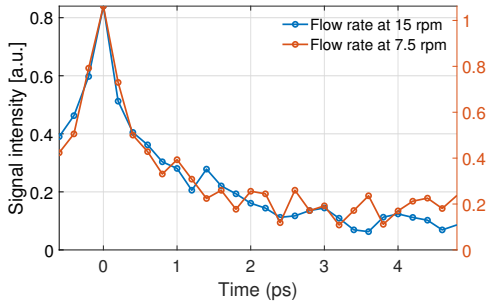

Figure 4.12: Comparison of the measured double pump experiment with UV and MIR lasers with different flow rates. Right y-axis corresponds to 7.5 rpm, left y-axis to 15 rpm.

by the laser pulses. With a flow rate of 15 rpm, the signal reduced to about 80 % of the signal with 7.5 rpm. For that reason, all other measurements were conducted with 7.5 rpm.

4.2.3 Laser intensity dependence measurement

Apart from the local temperature dependence of the experiment, we also conducted experiments to investigate the signal change with laser intensity change. In our measurements, we found an exponential increase in voltage change with increasing pulse energies for UV and MIR. In case of VIS, we can fit the data only following power law, $y(x) \propto x^m$, with an exponent of 1.7 (see fig. 4.13).
Our assumption is as follows: To transition an electron from gold to Fc^+ to generate Fc, hot electrons in gold are needed which have energetic overlap with the Ferrocene states. For higher laser pulse energy of the UV, the Fermi-Dirac distribution of the electrons in gold is spread broader and has more energy overlap with the Fc state. The resulting dependency on pulse energy is exponential, which follows our observation.
We assume, the MIR is exciting an aromatic CH stretch of the Ferrocene head group, which reorients the dipole moments of the surrounding water and thereby increasing the signal of the measurement. Also for MIR, the energy distribution of the Fc is stronger modified with higher pulse energy and follows the Fermi-Dirac distribution in the vicinity of the Fermi energy. Which explains also the exponential dependency we observe in our power dependence measurements.
The VIS laser pulses need to take the role of the UV light and excite hot electrons in gold. However, the photon energy to generate hot electrons in gold must be greater than the plasma edge of gold, which is at 2.4 eV or 516 nm in wavelength. Our VIS light has a photon energy of 1.6 eV and our UV light of 3.2 eV. Therefore, the UV light may be absorbed by gold directly,

but the VIS light may only be absorbed, if two photons are absorbed at the same time. Therefore, we assume a multi photon process, which then does not follow exponential increase with pulse energy as rather with power law dependency.

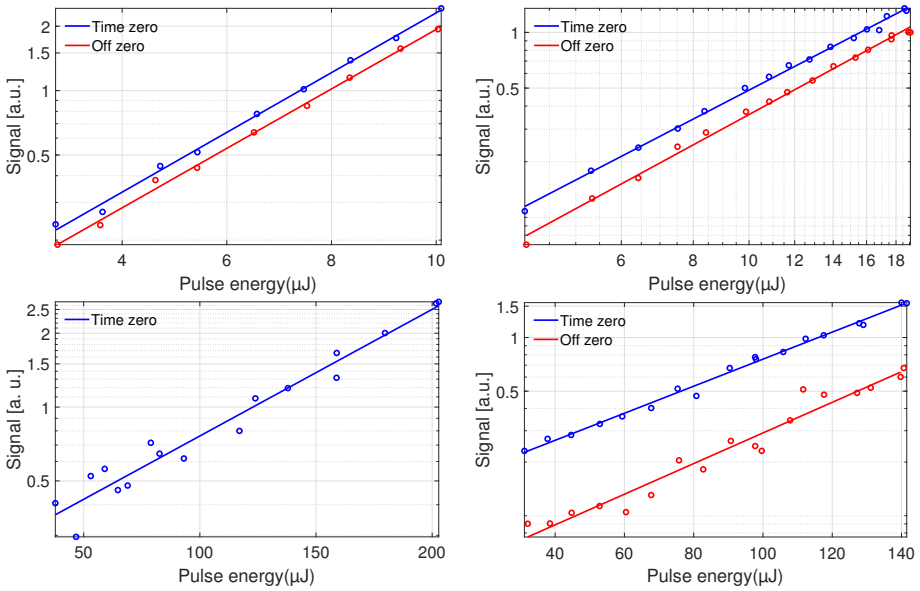

Figure 4.13: Logarithmic plots of double pump measurements at one specific time delay (either when both laser pulses arrived at the same time on the sample ⇒ Time zero or at different times ⇒ Off zero) and changing laser intensity to determine the laser power dependence of the signal. The measurements were conducted with increasing laser power of one pump laser while the second was held constant. In the plots, following intensities were changed: Top left: UV changed, MIR constant. Top right: VIS changed, MIR constant. Bottom left: UV constant MIR changed. Bottom right VIS constant, MIR changed.

4.3 Results

In the performed experiments, we find two decay times of the measured voltage change: One shorter with a lifetime of less than 120 ± 30 fs and a longer one with a lifetime of 4 ± 3 ps. We can differentiate three temporal situations: VIS before MIR , at time zero, and MIR before VIS . These situations are schematically drawn in figure 4.14.
Based on the theory stated by Schmickler [87], we assume the following chain of events: The mid infrared pulses drive the aromatic CH stretch of the Ferrocene head group. This stretch mode reorients the dipole moments of the surrounding water molecules in a time frame shorter than what we

can resolve in our experiment. Due to this reorientation, a redistribution of the possible energy states towards higher energies is generated. This can be seen in the Ferrocene distribution in the center image in figure 4.14. Once the VIS /UV pulses excite hot electrons in gold, there is better overlap between the hot electrons in gold and this deformed Ferrocene energy distribution than without this deformation. Therefore the electron transfer from gold to Ferrocene is mediated and the measured signal rises. However, this mode redistribution thermalizes to other vibrations of the molecules within 120 ± 30 fs. These other vibrational modes then still broaden the possible energy distribution of the Ferrocene (fig. 4.14, right image). Thereby, the measured signal is still higher until also this broadening is dissipated within 4.0 ± 1.5 ps to the surrounding environment and the equilibrium state is reached.
In our experiments, we also see a temporal asymmetry, which supports this theory. We only see an increased signal in case the MIR was applied before the VIS /UV (positive times). If the VIS /UV comes first and then the MIR (negative times), there is no vibrationally assisted charge transfer between gold and Ferrocene and therefore the case is the same as if the pulses would be far apart in delay time.
This means, the mode specific excitation with the MIR light before the VIS/UV pulse shows an increase in the measured signal on femtosecond time scales. This in turn means, the charge transfer between gold and Ferrocene can be mediated for several picoseconds by irradiating the sample with MIR light.

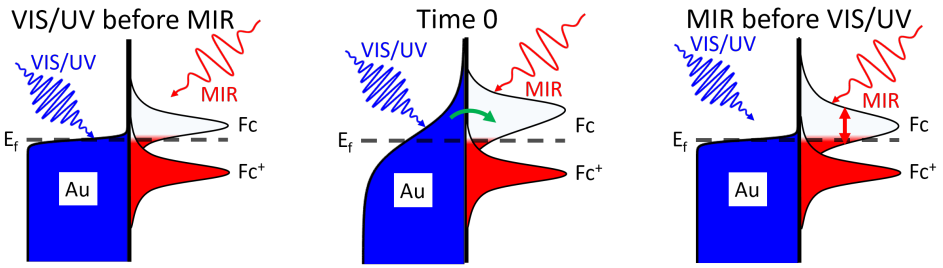

Figure 4.14: Schematic depiction of the energetic states of the liquid/metal interface. In gold, the states are filled until the Fermi energy, while in the Ferrocene SAM in water, there are only the states of the Fc and its ion Fc^+. Following Schmickler [87], The surrounding water dipoles influence the current energy level of Fc and Fc^+ due to spontaneous orientation changes. This broadens the possible energy states of Fc and Fc^+. Once excited by the MIR laser pulse, a specific vibrational mode is excited, which deforms the possible energy states of Fc to higher energies. After time zero, the excited vibrational mode of Fc thermalizes and still broadens the possible energy states, yielding still a higher signal than without excitation.

An alternative explanation may be, that the MIR laser pulses excite vibrational modes of the Ferrocene, which decay back to the ground state within a lifetime of 4 ± 3 ps. If, during that time, the sample is excited by a UV photon with an energy of 3.2 eV (or wavelength of 387 nm) or two VIS photons with half the energy, the already vibrationally excited Ferrocene molecules can reach an electronically excited state. This excitation may dissipate its energy to either the gold substrate or the surrounding solvent molecules. If the electrons dissipate their energy towards the gold substrate, the measured signal should increase. In the case of being close to time zero, a coherent vibronic excitation of Ferrocene could take place. This condition only appears when both pulses are in close temporal proximity to each other. We found the lifetime of this condition to be 120 ± 30 fs. This process seems to be more efficient, which is why the signal around time zero is about four times larger than the longer lasting signal. This situation is displayed in figure 4.15. However, we found no reliable basis for this explanation in the literature, for which we discarded it for now.

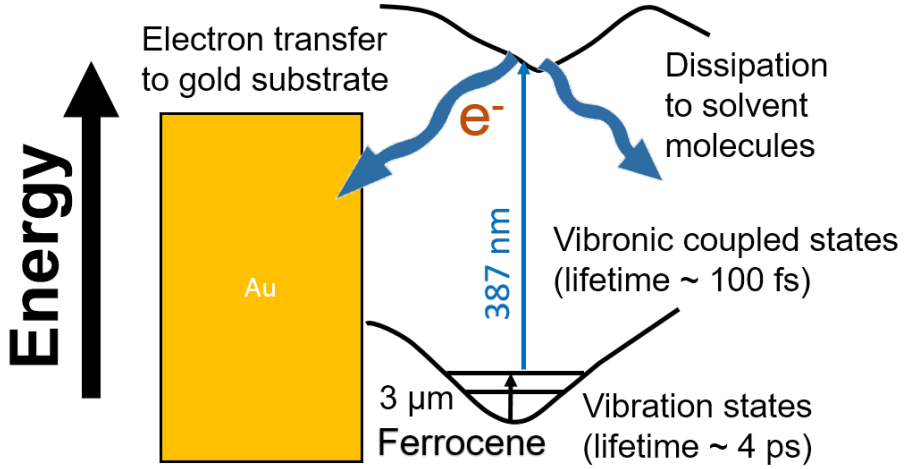

Figure 4.15: Schematic depiction of the energy distribution of the Ferrocene states on top of gold. On the left are the occupied states of the gold substrate in orange. On the right is the energy distribution of Ferrocene. Vibrational modes may be excited with 3 µm laser pulses. An excitation with 387 nm light excites the electrons in an excited state of the Ferrocene molecules, which then dissipate its energy to the gold substrate or the surrounding solvent.

To figure out, which theory describes the situation best, one may conduct the same experiment but with a different solution. For the first theory, this would mean a different possible energy state distribution of the Ferrocene molecules. If these molecules are then heavier or lighter, the reorientation time and efficiency of the molecules should change. This would then lead to

a signal with different magnitude and lifetime. However the second theory is independent on the solvent, so that here, no difference in signal value should be seen even with a different solution.

Chapter 5

Summary and outlook

In this work, I have presented the design and realization of a four staged OPCPA system with an experimental addendum to investigate the electron dynamics at solid/liquid interfaces of Ferrocene SAM on gold in an electrolyte solution.
The OPCPA setup was designed, realized and all individual amplification stages optimized by Alexander Tarasevitch, Oscar Naranjo and me. This process included the numerical calculation of each stage with different nonlinear crystals, the optimization of all stages by fine-tuning beam diameters and pulse energies, as well as evaluating and avoiding the effects of unwanted higher order processes. A program was written using LabVIEW to automatize the stabilization of the time overlap between seed and pump pulses at each amplification stage by using the angularly spread idler of the first NOPA stage as a signal. An existing FROG program was remodeled to be able to take second and third harmonic single shot FROG measurements of our VIS , near-IR and mid-IR laser pulses and evaluate the resulting images. With the working FROG for each pulse, it was possible to optimize the compression of the VIS and mid-IR laser pulses to 49 fs and 63 fs respectively with either sapphire windows for mid-IR or a home built SF11 prism compressor for VIS . Also, the near-IR output at 1.5 µm was compressed and optimized, but is a central part of Oscar Naranjo's PhD thesis and was therefore not discussed here. In the end, we created a laser system with three outputs centered at 0.8 µm, 1.5 µm and 3.0 µm wavelength with pulse energies of 40 µJ, 1800 µJ and 800 µJ, respectively and pulse durations of 49 fs (VIS) and 63 fs (mid-IR).
The VIS or the second harmonic of the VIS pulses (called here UV pulses) together with the mid-IR pulses were used for double pump measurements to investigate the vibrationally assisted electron transfer across a Ferrocene SAM at a gold/liquid interface.
For both the measurements of VIS and mid-IR or UV and mid-IR , we recorded a 120 ± 30 fs lasting signal increase at time zero and a 4.0 ± 1.5 ps last-

ing signal increase in case of the mid-IR pulses coming before the VIS or UV pulses.
We interpret our measurements as follows: The current dipole orientation of water molecules surrounding the Ferrocene head groups broadens the possible energy distribution of Ferrocene and its ion Ferrocenium. During the arrival of the MIR laser pulses, the MIR excites an aromatic CH stretch of the Ferrocene head group. This stretching induces a reorientation of the dipoles of surrounding water molecules, which deforms the possible energy distribution of Ferrocene. Therefore, the electronic transition from gold to Ferrocene is enhanced, when the VIS pulse arrives in temporal proximity to the MIR pulse. Our measurements show, that this condition only persist for 120 $\pm$ 30 fs after the mid-IR pulse arrives. After that, the vibrational excitation thermalizes into other vibrational modes of the molecule. This in turn still broadens the possible state distribution of Ferrocene. Due to better overlap with the hot electrons in gold, this still shows higher signal than without the vibrational excitation. We found, this broadening dissipates into its environment with a lifetime of 4.0 $\pm$ 1.5 ps.
All the setup and experiments were done with a repetition rate of 100 Hz. With this repetition rate, the average power of the system was easily manageable and all stages could be optimized for best output pulse energy. In all OPCPA systems higher repetition rates are always a trade-off between high pulse energies or high repetition rate. Our system was designed to work with a repetition rate of 20 kHz with the same output pulse energies as with 100 Hz. Therefore, the next step for the system is to increase the repetition rate of the system. This will reduce the necessary measurement time of similar experiments as described in chapter 4. Therefore, more systematic studies can be done to average over more measurements, thereby increasing the signal-to-noise ratio and being able to give clearer statements about the lifetimes of the processes.
Parallel to these experiments, another branch of the system was used to generate high harmonics in a hollow core capillary with noble gases. Therefore, Oscar Naranjo compressed the NIR output at 1.5 µm of the system and generated with this an X-ray beam with which already preliminary X-ray absorption measurements were conducted.
A third outlook could be the generation of high harmonics with our MIR output centered at 3.0 µm. We found in our studies, that the energy of the 3.0 µm beam is just too small for high harmonic generation. With a suitable additional amplifier of our pump line, the pulse energy may be increased there from 20 mJ to 80 mJ. With this increase, we could pump the last stage more and generate enough 3.0 µm radiation to also generate high harmonics with radiation. This is most interesting, since the cutoff frequency of high harmonics may be extended beyond 1 keV with a driver laser at 3.0 µm. With this also X-ray absorption spectroscopy can be performed.

Acronyms

ACF Autocorrelation function

BBO Beta Barium Borate

CE Counter electrode

CPA Chirped pulse amplification

CWL Central wavelength

DFG Difference frequency generation

FcC11 Ferrocene head group with a 11 piece CH sting

FROG Frequency resolved optical gating.

FWHM Full width at half maximum

GDD Group delay dispersion

GVD Group velocity dispersion

KTA Potassium Titanyle Arsenate

KTP Potassium Titanyle Phosphate

LBO Lithium Triborate

LNB Lithium Niobate

mid-IR mid infrared. Wavelengths in the range of 2.5-50 µm.

MIR The output laser light centered at 3.0 µm.

near-IR near infrared. Wavelengths in the range of 0.7-2.5 µm.

NEXAFS Near edge X-ray absorption spectroscopy

NIR The output laser light centered at 1.56 µm.

NOPA Noncollinear optical parametric amplification

OCV Open circuit voltage

OPA Optical parametric amplification

OPCPA Optical parametric chirped pulse amplification

RE Reference electrode

SAM Self assembled monolayer

SFG Sum frequency generation

SHG Second harmonic generation

SOD Second order dispersion

THG Third harmonic generation

TOD Third order dispersion

UV Second harmonic of the VIS OPCPA output. Central wavelength is at 387 nm.

VIS Our OPCPA output laser pulses centered at 770 nm.

WE Work electrode

XAS X-ray absorption spectroscopy

Bibliography

[1] T. H. Maiman, "Stimulated Optical Radiation in Ruby," *Nature*, vol. 187, pp. 493–494, 1960.

[2] T. H. Maiman, "Optical and Microwave-Optical Experiments in Ruby," *Phys. Rev. Lett.*, vol. 4, pp. 564–566, 1960.

[3] J. A. Valdmanis, R. L. Fork, and J. P. Gordon, "Generation of optical pulses as short as 27 femtoseconds directly from a laser balancing self-phase modulation, group-velocity dispersion, saturable absorption, and saturable gain," *Opt. Lett.*, vol. 10, pp. 131–133, 1985.

[4] P. F. Moulton, "Spectroscopic and laser characteristics of Ti:Al_2O_3," *J. Opt. Soc. Am. B*, vol. 3, pp. 125–133, 1986.

[5] D. Strickland and G. Mourou, "Compression of amplified chirped optical pulses," *Opt. Comm.*, vol. 55, pp. 447–449, 1985.

[6] A. Stolow, "Femtosecond Time-Resolved Photoelectron Spectroscopy of Polyatomic Molecules," *Annu. Rev. Phys. Chem.*, vol. 54, pp. 89–119, 2003.

[7] J. Xu and J. R. Knutson, "Chapter 8 Ultrafast Fluorescence Spectroscopy via Upconversion: Applications to Biophysics," in *Fluorescence Spectroscopy*, vol. 450 of *Methods in Enzymology*, pp. 159–183, Academic Press, 2008.

[8] R. Berera, R. van Grondelle, and J. Kennis, "Ultrafast transient absorption spectroscopy: Principles and application to photosynthetic systems," *Photosynth. Res.*, vol. 101, pp. 105–18, 2009.

[9] Q. Zhao and Z. Wang, "Manipulation of Tribological Properties of Metals by Ultrashort Pulsed Laser Micro-/Nanostructuring," in *Advances in Tribology* (P. H. Darji, ed.), ch. 1, Rijeka: IntechOpen, 2016.

[10] M. Lewenstein, P. Balcou, M. Y. Ivanov, A. L'Huillier, and P. B. Corkum, "Theory of high-harmonic generation by low-frequency laser fields," *Phys. Rev. A*, vol. 49, pp. 2117–2132, 1994.

[11] F. Wulf, *Novel high power THz sources driven by mode-locked thin-disk lasers*. PhD thesis, Ruhr-Universität Bochum, Universitätsbibliothek, 2021.

[12] P. Colarusso, L. H. Kidder, I. W. Levin, J. C. Fraser, J. F. Arens, and E. N. Lewis, "Infrared Spectroscopic Imaging: From Planetary to Cellular Systems," *Appl. Spectrosc.*, vol. 52, pp. 106A–120A, 1998.

[13] R. Bhargava, "Infrared Spectroscopic Imaging: The Next Generation," *Appl. Spectrosc.*, vol. 66, pp. 1091–1120, 2012.

[14] E. N. Lewis, P. J. Treado, R. C. Reeder, G. M. Story, A. E. Dowrey, C. Marcott, and I. W. Levin, "Fourier Transform Spectroscopic Imaging Using an Infrared Focal-Plane Array Detector," *Anal. Chem.*, vol. 67, pp. 3377–3381, 1995.

[15] Y. Yu, X. Gai, P. Ma, D.-Y. Choi, Z. Yang, R. Wang, S. Debbarma, S. J. Madden, and B. Luther-Davies, "A broadband, quasi-continuous, mid-infrared supercontinuum generated in a chalcogenide glass waveguide," *Laser Photonics Rev.*, vol. 8, pp. 792–798, 2014.

[16] T. Steinle, F. Neubrech, A. Steinmann, X. Yin, and H. Giessen, "Mid-infrared Fourier-transform spectroscopy with a high-brilliance tunable laser source: Investigating sample areas down to 5 µm diameter," *Opt. Express*, vol. 23, pp. 11105–11113, 2015.

[17] T. Popmintchev, M.-C. Chen, D. Popmintchev, P. Arpin, S. Brown, S. Ališauskas, G. Andriukaitis, T. Balčiunas, O. D. Mücke, A. Pugzlys, A. Baltuška, B. Shim, S. E. Schrauth, A. Gaeta, C. Hernández-García, L. Plaja, A. Becker, A. Jaron-Becker, M. M. Murnane, and H. C. Kapteyn, "Bright Coherent Ultrahigh Harmonics in the keV X-ray Regime from Mid-Infrared Femtosecond Lasers," *Science*, vol. 336, pp. 1287–1291, 2012.

[18] P. Rigaud, A. V. de Walle, M. Hanna, N. Forget, F. Guichard, Y. Zaouter, K. Guesmi, F. Druon, and P. Georges, "Supercontinuum-seeded few-cycle mid-infrared OPCPA system," *Opt. Express*, vol. 24, pp. 26494–26502, 2016.

[19] N. Bigler, J. Pupeikis, S. Hrisafov, L. Gallmann, C. R. Phillips, and U. Keller, "High-power OPCPA generating 1.7 cycle pulses at 2.5 µm," *Opt. Express*, vol. 26, pp. 26750–26757, 2018.

[20] N. Thiré, R. Maksimenka, B. Kiss, C. Ferchaud, G. Gitzinger, T. Pinoteau, H. Jousselin, S. Jarosch, P. Bizouard, V. D. Pietro, E. Cormier, K. Osvay, and N. Forget, "Highly stable, 15 W, few-cycle, 65 mrad CEP-noise mid-IR OPCPA for statistical physics," *Opt. Express*, vol. 26, pp. 26907–26915, 2018.

[21] P. Malevich, T. Kanai, H. Hoogland, R. Holzwarth, A. Baltuška, and A. Pugžlys, "Broadband mid-infrared pulses from potassium titanyl arsenate/zinc germanium phosphate optical parametric amplifier pumped by Tm, Ho-fiber-seeded Ho:YAG chirped-pulse amplifier," *Opt. Lett.*, vol. 41, pp. 930–933, 2016.

[22] H. Park, A. Camper, K. Kafka, B. Ma, Y. H. Lai, C. Blaga, P. Agostini, L. F. DiMauro, and E. Chowdhury, "High-order harmonic generations in intense MIR fields by cascade three-wave mixing in a fractal-poled LiNbO3 photonic crystal," *Opt. Lett.*, vol. 42, pp. 4020–4023, 2017.

[23] D. Woodbury, L. Feder, V. Shumakova, C. Gollner, R. Schwartz, B. Miao, F. Salehi, A. Korolov, A. Pugžlys, A. Baltuška, and H. M. Milchberg, "Laser wakefield acceleration with mid-IR laser pulses," *Opt. Lett.*, vol. 43, pp. 1131–1134, 2018.

[24] C. Schmidt, *Experimental Results of TR-XAS in Liquids*, pp. 103–111. Cham: Springer International Publishing, 2021.

[25] C. Kleine, M. Ekimova, G. Goldsztejn, S. Raabe, C. Strüber, J. Ludwig, S. Yarlagadda, S. Eisebitt, M. J. J. Vrakking, T. Elsaesser, E. T. J. Nibbering, and A. Rouzée, "Soft X-ray Absorption Spectroscopy of Aqueous Solutions Using a Table-Top Femtosecond Soft X-ray Source," *J. Phys. Chem. Lett.*, vol. 10, pp. 52–58, 2019.

[26] H. Stiel, J. Braenzel, J. Tuemmler, A. Jonas, I. Mantouvalou, A. Erko, A. Heilmann, M. Moerbeck-Bock, and M. Schnuerer, "Ultrafast NEXAFS spectroscopy in the lab using laser-based sources and advanced X-ray optics," in *International Conference on X-Ray Lasers 2020* (D. Bleiner, ed.), vol. 11886, pp. 290 – 297, International Society for Optics and Photonics, SPIE, 2021.

[27] A. Jonas, H. Stiel, L. Glöggler, D. Dahm, K. Dammer, B. Kanngießer, and I. Mantouvalou, "Towards Poisson noise limited optical pump soft X-ray probe NEXAFS spectroscopy using a laser-produced plasma source," *Opt. Express*, vol. 27, pp. 36524–36537, 2019.

[28] P. Vöhringer, "Vibrations tell the tale. a time-resolved mid-infrared perspective of the photochemistry of iron complexes," *Dalton Trans.*, vol. 49, pp. 256–266, 2020.

[29] R. D. Pensack, K. M. Banyas, L. W. Barbour, M. Hegadorn, and J. B. Asbury, "Ultrafast vibrational spectroscopy of charge-carrier dynamics in organic photovoltaic materials," *Phys. Chem. Chem. Phys.*, vol. 11, pp. 2575–2591, 2009.

[30] M. Fermann, A. Galvanauskas, and G. Sucha, *Ultrafast Lasers: Technology and Applications*. Optical Engineering - Marcel Dekker, Florida: CRC Press, 1st ed., 2002.

[31] M. Lackner, M. Hille, and E. Hasselbrink, "Vibrational Energy Redistribution between CH Stretching Modes in Alkyl Chain Monolayers Revealed by Time-Resolved Two-Color Pump–Probe Sum Frequency Spectroscopy," *J. Phys. Chem. Lett.*, vol. 11, pp. 108–112, 2020.

[32] J. Pupeikis, P.-A. Chevreuil, N. Bigler, L. Gallmann, C. R. Phillips, and U. Keller, "Water window soft X-ray source enabled by a 25 W few-cycle 2.2 µm OPCPA at 100 kHz," *Optica*, vol. 7, pp. 168–171, 2020.

[33] R. Budriūnas, T. Stanislauskas, J. Adamonis, A. Aleknavičius, G. Veitas, D. Gadonas, S. Balickas, A. Michailovas, and A. Varanavičius, "53 W average power CEP-stabilized OPCPA system delivering 5.5 TW few cycle pulses at 1 kHz repetition rate," *Opt. Express*, vol. 25, pp. 5797–5806, 2017.

[34] S. Hrisafov, J. Pupeikis, P.-A. Chevreuil, F. Brunner, C. R. Phillips, L. Gallmann, and U. Keller, "High-power few-cycle near-infrared OPCPA for soft X-ray generation at 100 kHz," *Opt. Express*, vol. 28, pp. 40145–40154, 2020.

[35] T. Kanai, Y. Lee, M. Seo, and D. E. Kim, "Supercontinuum-seeded, carrier-envelope phase-stable, 4.5-W, 3.8 µm, 6-cycle, KTA optical parametric amplifier driven by a 1.4-ps Yb:YAG thin-disk amplifier for nonperturbative spectroscopy in solids," *J. Opt. Soc. Am. B*, vol. 36, pp. 2407–2413, Sep 2019.

[36] K. Tian, L. He, X. Yang, and H. Liang, "Mid-Infrared Few-Cycle Pulse Generation and Amplification," *Photonics*, vol. 8, no. 8, p. 290, 2021.

[37] M. Musheghyan, P. P. Geetha, D. Faccialà, A. Pusala, G. Crippa, A. Campolo, A. G. Ciriolo, M. Devetta, A. Assion, C. Manzoni, C. Vozzi, and S. Stagira, "Tunable, few-cycle, CEP-stable mid-IR optical parametric amplifier for strong field applications," *J. Phys. B: At. Mol. Opt. Phys.*, vol. 53, p. 185402, 2020.

[38] X. Zou, W. Li, S. Qu, K. Liu, H. Li, Q. J. Wang, Y. Zhang, and H. Liang, "Flat-top pumped multi-millijoule mid-infrared parametric chirped-pulse amplifier at 10 kHz repetition rate," *Laser Photonics Rev.*, p. 2000292, 2021.

[39] M. Bock, L. von Grafenstein, U. Griebner, and T. Elsaesser, "Generation of millijoule few-cycle pulses at 5 µm by indirect spectral shaping

of the idler in an optical parametric chirped pulse amplifier," *J. Opt. Soc. Am. B*, vol. 35, pp. C18–C24, 2018.

[40] U. Elu, T. Steinle, D. Sánchez, L. Maidment, K. Zawilski, P. Schunemann, U. D. Zeitner, C. Simon-Boisson, and J. Biegert, "Table-top high-energy 7 µm OPCPA and 260 mJ Ho:YLF pump laser," *Opt. Lett.*, vol. 44, pp. 3194–3197, 2019.

[41] P. Fuertjes, L. von Grafenstein, C. Mei, M. Bock, U. Griebner, and T. Elsaesser, "Cr:ZnS-based soliton self-frequency shifted signal generation for a tunable sub-100 fs MWIR OPCPA," *Opt. Express*, vol. 30, pp. 5142–5150, 2022.

[42] C. Heese, C. R. Phillips, B. W. Mayer, L. Gallmann, M. M. Fejer, and U. Keller, "75 MW few-cycle mid-infrared pulses from a collinear apodized APPLN-based OPCPA," *Opt. Express*, vol. 20, pp. 26888–26894, 2012.

[43] R. W. Boyd, *Nonlinear Optics*. Cambridge, Massachusetts: Academic Press, Inc., 3rd ed., 2008.

[44] C. Skrobol, *High-Intensity, Picosecond-Pumped, Few-Cycle OPCPA*. PhD thesis, Ludwig-Maximilians-Universität München, 2014.

[45] D. A. Sánchez Peacham, *Development of a high intensity Mid-Ir OPCPA pumped by a HO:YLF amplifier*. PhD thesis, Universitat Politècnica de Catalunya. Institut de Ciències Fotòniques, 2020.

[46] J. Rothhardt, *High power ultra-short pulse lasers based on fiber driven OPCPA*. PhD thesis, Friedrich-Schiller-Universität Jena, 2010.

[47] `https://as-photonics.com/products/snlo/`.

[48] J. M. Manley and H. E. Rowe, "Some General Properties of Nonlinear Elements-Part I. General Energy Relations," *Proceedings of the IRE*, vol. 44, no. 7, pp. 904–913, 1956.

[49] C. Manzoni and G. Cerullo, "Design criteria for ultrafast optical parametric amplifiers," *Journal of Optics*, p. 103501, 2016.

[50] R. Baumgartner and R. Byer, "Optical parametric amplification," *IEEE J. Quantum Electron.*, vol. 15, no. 6, pp. 432–444, 1979.

[51] I. N. Ross, P. Matousek, G. H. C. New, and K. Osvay, "Analysis and optimization of optical parametric chirped pulse amplification," *J. Opt. Soc. Am. B*, vol. 19, pp. 2945–2956, 2002.

[52] R. Sutherland, *Handbook of Nonlinear Optics*. Optical Science and Engineering, New York: Marcel Dekker, Inc., 2nd ed., 2003.

[53] C. Runge, "Über die numerische Auflösung von Differentialgleichungen," *Mathematische Annalen*, vol. 46, no. 2, pp. 167–178, 1895.

[54] `https://refractiveindex.info/`.

[55] `https://en.wikipedia.org/wiki/File:Crystal_on_graph_paper.jpg`.

[56] E. Dekemper, *Development of an AOTF-based hyperspectral imager for atmospheric remote sensing*. Paris: Presses universitaires de Louvain, 1st ed., 2014.

[57] G. M. Gale, M. Cavallari, T. J. Driscoll, and F. Hache, "Sub-20-fs tunable pulses in the visible from an 82-MHz optical parametric oscillator," *Opt. Lett.*, vol. 20, pp. 1562–1564, 1995.

[58] D. N. Schimpf, J. Rothhardt, J. Limpert, A. Tünnermann, and D. C. Hanna, "Theoretical analysis of the gain bandwidth for noncollinear parametric amplification of ultrafast pulses," *J. Opt. Soc. Am. B*, vol. 24, pp. 2837–2846, 2007.

[59] V. Chvykov, "New Generation of Ultra-High Peak and Average Power Laser Systems," in *High Power Laser Systems*, pp. 63–90, Rijeka: IntechOpen, 2018.

[60] O. Martinez, "3000 times grating compressor with positive group velocity dispersion: Application to fiber compensation in 1.3-1.6 µm region," *IEEE J. Quantum Electron.*, vol. 23, no. 1, pp. 59–64, 1987.

[61] `https://www.rp-photonics.com/ytterbium_doped_laser_gain_media.html`.

[62] A. Dubietis, G. Jonušauskas, and A. Piskarskas, "Powerful femtosecond pulse generation by chirped and stretched pulse parametric amplification in BBO crystal," *Opt. Comm.*, vol. 88, pp. 437–440, 1992.

[63] P. Tournois, "Acousto-optic programmable dispersive filter for adaptive compensation of group delay time dispersion in laser systems," *Opt. Comm.*, vol. 140, pp. 245–249, 1997.

[64] `https://www.newport.com/n/diffraction-grating-physics`, "Richardson gratings™."

[65] `http://toolbox.lightcon.com/tools/prismpair/`.

[66] S. Backus, C. G. Durfee, M. M. Murnane, and H. C. Kapteyn, "High power ultrafast lasers," *Rev. Sci. Instrum.*, vol. 69, pp. 1207–1223, 1998.

[67] A. E. Siegman, *Lasers*. California: University Science Books, 2nd ed., 1986.

[68] P. R. Griffiths and J. A. d. Haseth, *Fourier Transform Infrared Spectroscopy*. Hoboken, New Jersey: Wiley-Interscience, 2nd ed., 2007.

[69] F. K. Tittel, D. Richter, and A. Fried, *Mid-Infrared Laser Applications in Spectroscopy*. Springer Berlin Heidelberg, 1nd ed., 2003.

[70] W. Petrich, "Mid-Infrared and Raman spectroscopy for medical diagnostics," *Appl. Spectrosc. Rev.*, vol. 36, no. 2-3, pp. 181–237, 2001.

[71] C. Petibois and G. Déléris, "Chemical mapping of tumor progression by FT-IR imaging: towards molecular histopathology," *Trends Biotechnol.*, vol. 24, no. 10, pp. 455–462, 2006.

[72] M. Bridger, O. A. Naranjo-Montoya, A. Tarasevitch, and U. Bovensiepen, "Towards high power broad-band OPCPA at 3000 nm," *Opt. Express*, vol. 27, pp. 31330–31337, 2019.

[73] `https://www.laserquantum.com/`.

[74] `https://amplitude-laser.com/`.

[75] `https://www.amphos.de/technology/`.

[76] M. Schulz, R. Riedel, A. Willner, T. Mans, C. Schnitzler, P. Russbueldt, J. Dolkemeyer, E. Seise, T. Gottschall, S. Hädrich, S. Duesterer, H. Schlarb, J. Feldhaus, J. Limpert, B. Faatz, A. Tünnermann, J. Rossbach, M. Drescher, and F. Tavella, "Yb:YAG Innoslab amplifier: efficient high repetition rate subpicosecond pumping system for optical parametric chirped pulse amplification," *Opt. Lett.*, vol. 36, pp. 2456–2458, 2011.

[77] "Frank Meyer developed the splitstep program for Matlab, which can use measured spectra of the seed and pump pulses, calculate the interaction in the nonlinear crystal and yield the emitting pulse parameters. Alexander Tarasevitch later on improved it to yield a two dimensional output of the beam (The dimensions perpendicular to the propagation direction are considered symmetrical, which shrinks the 3 dimensional problem to 2 dimensions). And I optimized it for quicker execution and to cover a bigger parameter pool.,"

[78] S. Hädrich, J. Rothhardt, M. Krebs, S. Demmler, J. Limpert, and A. Tünnermann, "Improving carrier-envelope phase stability in optical

parametric chirped-pulse amplifiers by control of timing jitter," *Opt. Lett.*, vol. 37, pp. 4910–4912, 2012.

[79] F. J. Furch, A. Giree, F. Morales, A. Anderson, Y. Wang, C. P. Schulz, and M. J. J. Vrakking, "Close to transform-limited, few-cycle 12 µJ pulses at 400 kHz for applications in ultrafast spectroscopy," *Opt. Express*, vol. 24, pp. 19293–19310, 2016.

[80] S.-W. Huang, J. Moses, and F. X. Kärtner, "Broadband noncollinear optical parametric amplification without angularly dispersed idler," *Opt. Lett.*, vol. 37, pp. 2796–2798, 2012.

[81] K. Okamura and T. Kobayashi, "Octave-spanning carrier-envelope phase stabilized visible pulse with sub-3-fs pulse duration," *Opt. Lett.*, vol. 36, pp. 226–228, 2011.

[82] G. Hansson, H. Karlsson, S. Wang, and F. Laurell, "Transmission measurements in KTP and isomorphic compounds," *Appl. Opt.*, vol. 39, pp. 5058–5069, 2000.

[83] R. Trebino, *Frequency-Resolved Optical Gating: The Measurement of Ultrashort Laser Pulses*, pp. 117–139. Springer New York, 1st ed., 2000.

[84] `https://www.swampoptics.com/autocorrelation.html/`.

[85] `https://frog.gatech.edu/code.html/`.

[86] `https://physics.nist.gov/PhysRefData/ASD/lines_form.html`.

[87] W. Schmickler and E. Santos, *Interfacial Electrochemistry*, pp. 19–27. Springer Berlin Heidelberg, 2nd ed., 2010.

[88] T. Erdey-Grúz and M. Volmer, "Zur theorie der wasserstoff Überspannung," *Z. Phys. Chem.*, vol. 150A, pp. 203–213, 1930.

[89] R. Marcus and N. Sutin, "Electron transfers in chemistry and biology," *Biochim. Biophys. Acta*, vol. 811, pp. 265–322, 1985.

[90] F. Lapointe, M. Wolf, R. K. Campen, and Y. Tong, "Probing the Birth and Ultrafast Dynamics of Hydrated Electrons at the Gold/Liquid Water Interface via an Optoelectronic Approach," *J. Am. Chem. Soc.*, vol. 142, pp. 18619–18627, 2020.

List of publications

M. Bridger, O. Naranjo-Montoya, A. Tarasevitch, and U. Bovensiepen, "Towards high power broad-band OPCPA at 3000 nm," *Opt. Express*, vol. 27, no. 22, pp. 31330-31337, 2019.

O. Naranjo-Montoya, M. Bridger, A. Tarasevitch, and U. Bovensiepen, "Compression and characterization of ultrashort pulses at 1.5 and 3 µm wavelength," *Optica High-brightness Sources and Light-driven Interactions Congress 2022*, Optica Publishing Group, JW5A.10, 2022.

Acknowledgements

In my time at the university Duisburg/Essen, I learned a lot about laser systems, ultrashort processes, the Ruhr-area culture and many more topics. All this was very interesting to learn and for that I would like to thank a number of people.
First of all, I want to thank my Ph.D. supervisor Uwe Bovensiepen, who gave me the possibility to work in this interesting field and with this welcoming group. I often referred to my work as playing with scientific Lego, because we had to set up all the mirrors, lens telescopes and crystals. Uwe always saw to it, that we had enough "bricks" and that I did not have to worry about it. He was able to financially support us, because of our collaborate research center 1242 of the DFG. He is the leading spokesperson of this CRC and worked a lot to keep everyone on track for a successful collaboration. Only with his pushes, I learned about all the projects and other doctoral students of the CRC, in the course of doctoral retreats, various conferences and summer/winter schools. I am very grateful, that I was allowed to participate in all these events, because they were a lot of fun, a great opportunity for networking and I learned a lot.
Next I want to thank my scientific supervisor Alexander Tarasevitch for all his support in the lab and all the interesting talks at lunch and in the coffee breaks. Right away, I knew he had a deep understanding of all the devices in the lab, and he was always there with guidance and assistance if a problem arose. There were times when I and my lab mate Oscar Naranjo were almost giving up on a problem, as Alex inquired about the issue and solved it by turning just the right screws.
I am very grateful to my lab mate Oscar Naranjo with whom I spent most of my time here. We were often spending many hours optimizing the system near to perfection, and he was very patient and persistent in this process. I believe, only together, it was possible to build this complex OPCPA system and achieve the values stated in this thesis. Also, apart from work, we frequently met to go bouldering, top rope climbing and for a beer in the evening. All in all, I am very happy for his friendship, all his advises and collaboration throughout my time here in Duisburg.
I also want to thank Zhipeng Huang, Yujin Tong and Kramer Campen, who collaborated with me in the electron transfer studies at interfaces. They al-

ways provided excellent samples for our measurements, helped with taking the measurements and interpreting our results.
I want to thank the other members of the AG Bovensiepen, also the one who already left, and in particular Fabian, Marius, Yasin, Florian, Thies, Philipp, Eric, Christina, Klaus and Michael.
Finally I am very happy about many uplifting talks with my mother Cäcilia and many relieving visits in Bavaria with her, my bigger brother Mario and all of my sister's family: Angela, Christian and their three kids: Leonie, Jonas and Philipp.
Unfortunately, my father Norman died during my time here in 2019, but I think he would be proud, seeing me now with my achievements. He was the best father I could ever wish for. He was always kind to everyone, he supported me all my life and in all my doings. God bless his soul.

DOI: 10.17185/duepublico/78214
URN: urn:nbn:de:hbz:465-20230419-153556-8